IS-T-798

ELECTROCATALYTIC ACTIVITY AND SURFACE PROPERTIES OF TUNGSTEN BRONZES

Michael Francis Weber

Ph.D. Thesis Submitted to Iowa State University

Ames Laboratory, DOE
Iowa State University
Ames, Iowa 50011

Date Transmitted: December 1977

PREPARED FOR THE U.S. DEPARTMENT OF ENERGY
UNDER CONTRACT NO. W-7405-eng-82

DISCLAIMER

NOTICE

Available from: National Technical Information Service
U. S. Department of Commerce
P.O. Box 1553
Springfield, VA 22161

Price: Microfiche $3.00

TABLE OF CONTENTS

LIST OF FIGURES

Page

Page

Page

LIST OF TABLES

ABSTRACT

The electrocatalytic activities of sodium tungsten bronzes, including high purity crystals, platinum doped crystals, and platinum plated crystals, have been measured for oxygen reduction in acid solution. In addition, a survey of the electrocatalytic activities and general electrochemical properties of other alkali tungsten bronzes, thalium tungsten bronze, and tungsten trioxide were investigated and compared to sodium tungsten bronze. All measurements were done on single crystals. Pure sodium tungsten bronzes and WO_3 have a slight catalytic activity for oxygen reduction. The exchange current density is approximately 10^{-14} A/cm^2.

Doping the cubic sodium tungsten bronze with up to 800 ppm of platinum slightly increased the catalytic activity of the crystals, but the effect was noticeable only at very low current densities. Platinum preelectrolysis of the solution was shown to contaminate the crystal surface with significant amounts of platinum. For the platinum plated bronze crystals, no synergistic effect between the platinum and the bronze was observed for oxygen reduction. However, different platinum plating methods gave more than an order of magnitude difference in catalytic activity, with the same amount of platinum. The platinum was deposited on the bronze surface in different forms by the different plating methods. One possible form of highly dispersed platinum on a bronze surface is the formation of a platinum tungsten bronze, Pt_xWO_3.

Hydrogen tungsten bronze is formed in the surface layers of all the bronzes at potentials below +0.2 V (NHE), and the reaction is completely reversible.

One possible form of highly dispersed platinum on a bronze surface is the formation of a platinum tungsten bronze, Pt_xWO_3.

Hydrogen tungsten bronze is formed in the surface layers of all the bronzes at potentials below +0.2 V (NHE), and the reaction is completely reversible.

CHAPTER 1. INTRODUCTION

Energy shortages in this decade have prompted many scientists to focus attention upon the subject of the solid-liquid interface. The technological importance, as well as the interesting features of the solid-liquid interface, and the physical processes which can be made to occur there, have combined to make this subject one of the fastest growing areas of research in the scientific community. The work described here involves the use of the solid-liquid interface to convert stored chemical energy to electricity. The common term for such a device is "fuel cell". The major portion of this study was directed towards the development of efficient electrodes for a hydrogen-oxygen fuel cell. Such research required a combination of experimental techniques from the fields of electrochemistry, solid state physics, and surface physics.

Electrocatalysis

The process of charge transfer from electrode to electrolyte is not well understood, especially for such complicated reactions as the hydrogen and oxygen reactions which occur in a hydrogen-oxygen fuel cell. Such reactions proceed swiftly only if catalyzed, and the process of electrocatalysis at an electrode-solution interface is very difficult to describe theoretically. Today's researchers in the field of electrocatalysis have only general guidelines to aid them in their attempts to produce a more efficient oxygen electrode. Wolfram et al. (1) have presented a model of the d-electron surface states of transition metals in perovskite structured compounds. The model describes the role the d-electrons play in several

catalytic processes, such as the disassociative adsorption of H_2 gas molecules, and the chemisorption of OH^- ions from aqueous solutions. Hopefully, this theory can be extended to include catalytic steps in the oxygen reaction in acid electrolytes. Oxygen is generally thought to adsorb in the end-on configuration (2) on most materials, with one oxygen molecule dangling above the electrode surface. A model for a reversible oxygen electrode in alkaline electrolytes has been presented by Tseung and Bevan (3). This model requires the flat, or side-on, adsorption of O_2 molecules. Tseung and Bevan have reported reversible behavior for the oxygen reaction on antiferromagnetic materials above the Néel temperature.

The oxygen reaction is extremely slow. The reason for the small rate constant is the inability of most electrodes to break the oxygen-oxygen bond (2, 3, 4). Materials on which oxygen would adsorb in a way which would facilitate this process are expected to be good catalysts for the oxygen reaction. For the most part, the method of research has been to test all materials that meet at least two requirements: stability in acidic or basic solutions, and high enough electrical conductivity to supply electrons to the reaction site. Much of the basic research done to date has, therefore, been concerned only with understanding the kinetics of the oxygen reaction on a few metals, mostly the noble metals. The problem is complicated by the large number of steps involved in the oxygen reaction and the different paths that the reaction may follow on different metals. The most probable reaction paths are listed in Chapter 2. The overall reaction is

$$O_2(g) + 4H^+ + 4e^- \rightleftarrows 2H_2O(l) \qquad E° = 1.23 \text{ volts}$$

Oxygen gas is consumed in a fuel cell at the oxygen electrode, while it is evolved at the oxygen electrode in an electrolysis cell. A schematic diagram of a hydrogen-oxygen fuel cell is shown in Figure 1.1. The above reaction proceeds to the left in an electrolysis cell and to the right in a fuel cell. $E°$ is the theoretical equilibrium potential, or rest potential, of this reaction as measured against a hydrogen electrode in the same solution. A diagram of the current-potential relationships at both electrodes in the fuel cell are shown in Figure 1.2. Since a log scale is used, the magnitude of the current density is plotted. The parameter of interest, when current is drawn or driven through the electrode, is the deviation of the potential from $E°$. This parameter is termed the overvoltage, or overpotential, for both positive and negative deviations from the equilibrium potential. The overpotentials at the oxygen electrode, in this case polished platinum metal, are much greater than at the hydrogen electrode. The current-potential relationships of both electrodes combine to give the output curve for a fuel cell, shown in Figure 1.3 with a linear current scale. An electrode's value as an oxygen electrocatalyst is usually determined by comparing its overpotentials, as a function of current density, to the overpotentials measured on a platinum electrode.

The Tungsten Bronzes

Few electrically conducting materials are stable in acid solutions at the potentials where oxygen reduction proceeds. Even fewer conductors

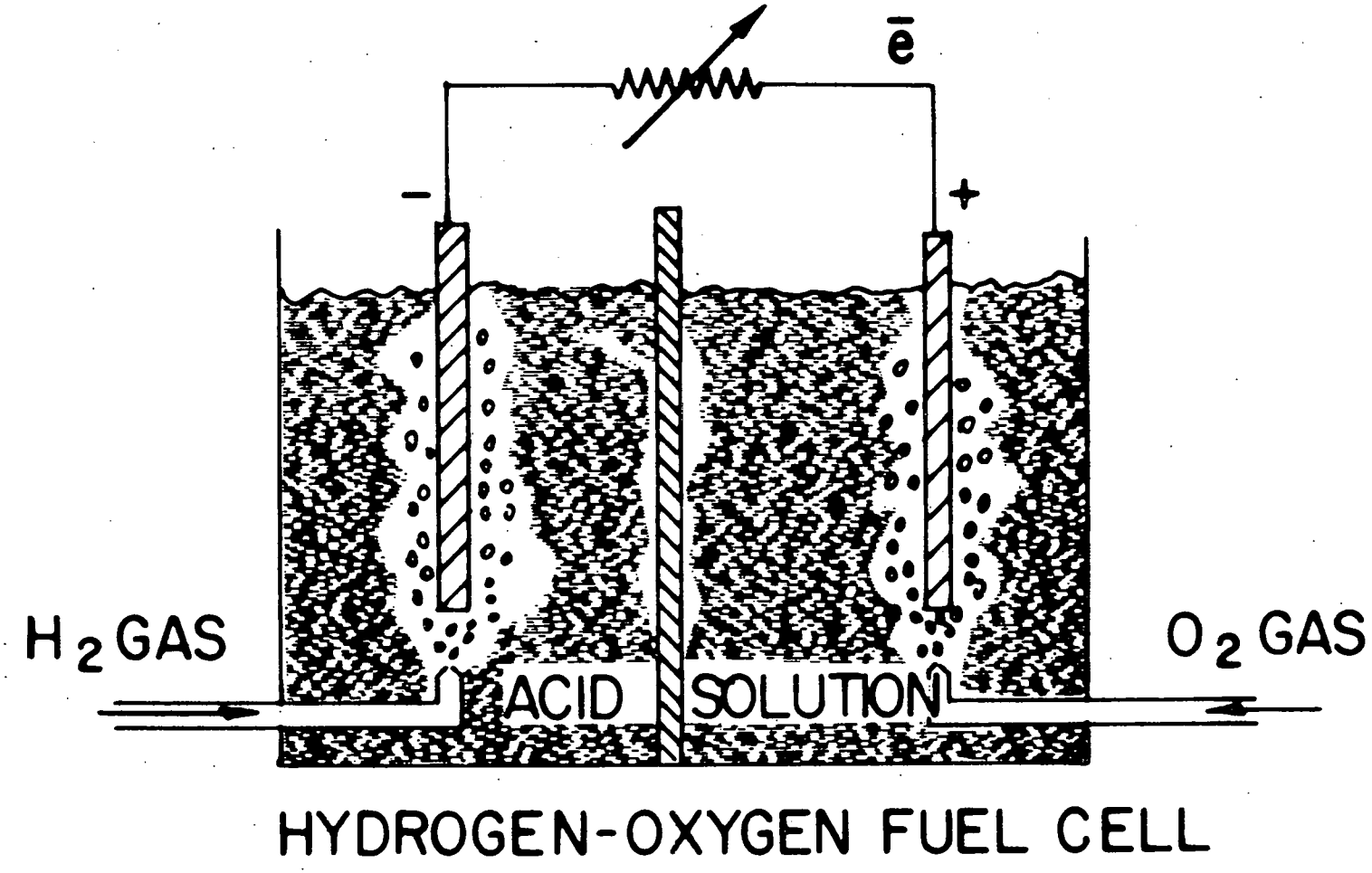

Figure 1.1. Schematic diagram of a fuel cell. The gases are bubbled over the electrodes which are immersed in the acid solution. The center barrier is a porous membrane that allows ionic conduction but prevents mixing of the gases

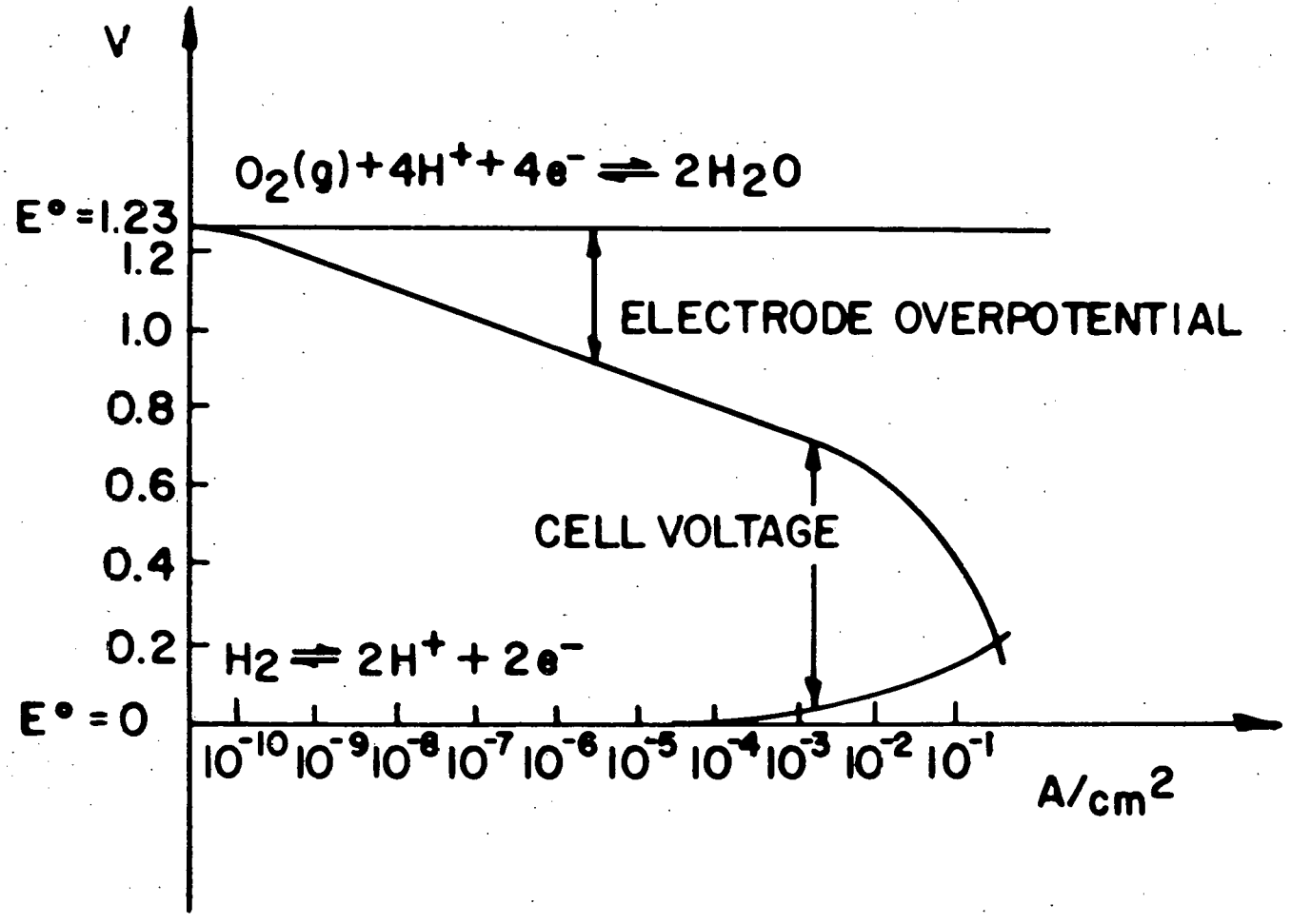

Figure 1.2. Current-potential curves for both electrodes as measured against a third, or reference electrode which is at equilibrium. An exponential i-v relationship exists over a wide current range (10^{-9} A/cm^2 to 10^{-3} A/cm^2) for the oxygen electrode

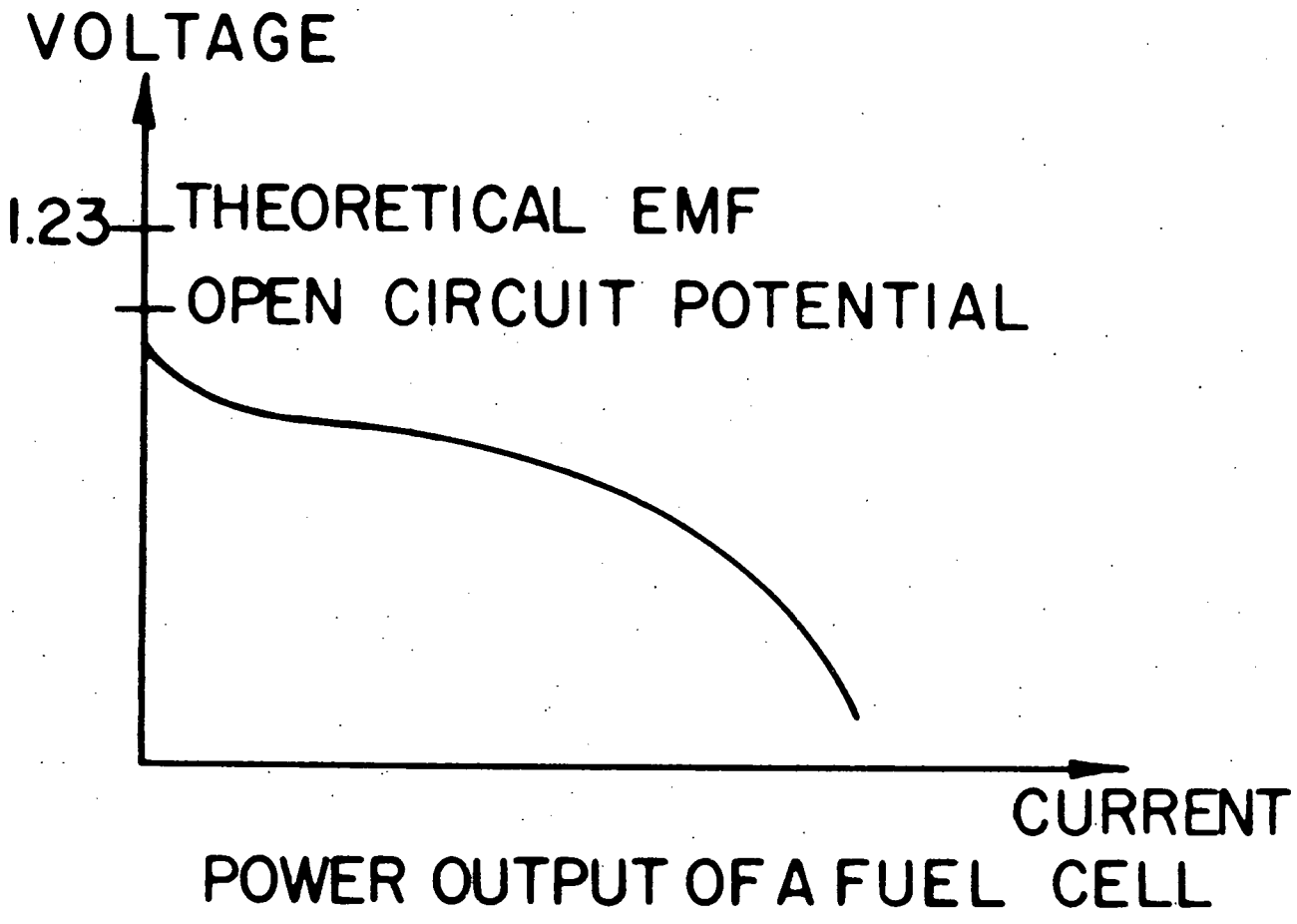

Figure 1.3. Plot of the voltage difference between the H_2 and O_2 electrodes as a function of the current drawn from the cell

meet a third, more unusual criteria that it must catalyze the oxygen reaction. For this reason, the announcement of Sepa, Damjanovic, and Bockris (5) that the sodium tungsten bronzes Na_xWO_3 ($0 < x < 1$) met all three requirements, especially the third requirement, caused considerable excitement among workers in the field of electrocatalysis.

Sodium tungsten bronzes are part of a general class of nonstochiometric compounds with the formula M_xWO_3 where M is a metal and $0 < x < 1$. WO_3 is a semiconductor with a band gap of 2.6 eV (6) and has a monoclinic structure. Additions of different amounts of metal atoms, such as the alkali elements, result in a large number of different crystal structures with differing electronic properties. The compositions and structures of a number of bronzes are shown in Figure 1.4. For $x > 0.5$ Na_xWO_3 has a nearly cubic structure, with one of the crystal axes only slightly longer than the other two. This phase will still be referred to here as the cubic phase. The unit cell of the cubic bronze structure consists of a tungsten atom at the cube center, oxygen atoms on the cube faces, and the sodium atoms at the cube corners. The oxygen atoms form an octahedra around the tungsten atom, so the compound is composed of corner bonded WO_6 octahedra surrounding the sodium atoms. In general, Magneli (7) has shown that the cubic structure consists of four octahedra surrounding an alkali metal M, and the tetragonal-I and hexagonal structures consist of five and six-member octahedra rings, respectively, surrounding the alkali atom M. All the hexagonal crystals are metals.

Na_xWO_3 is a metal for $x \geq 0.25$ and a semiconductor for $x \leq 0.25$. The metal-semiconductor transition occurs at the tetragonal-I to

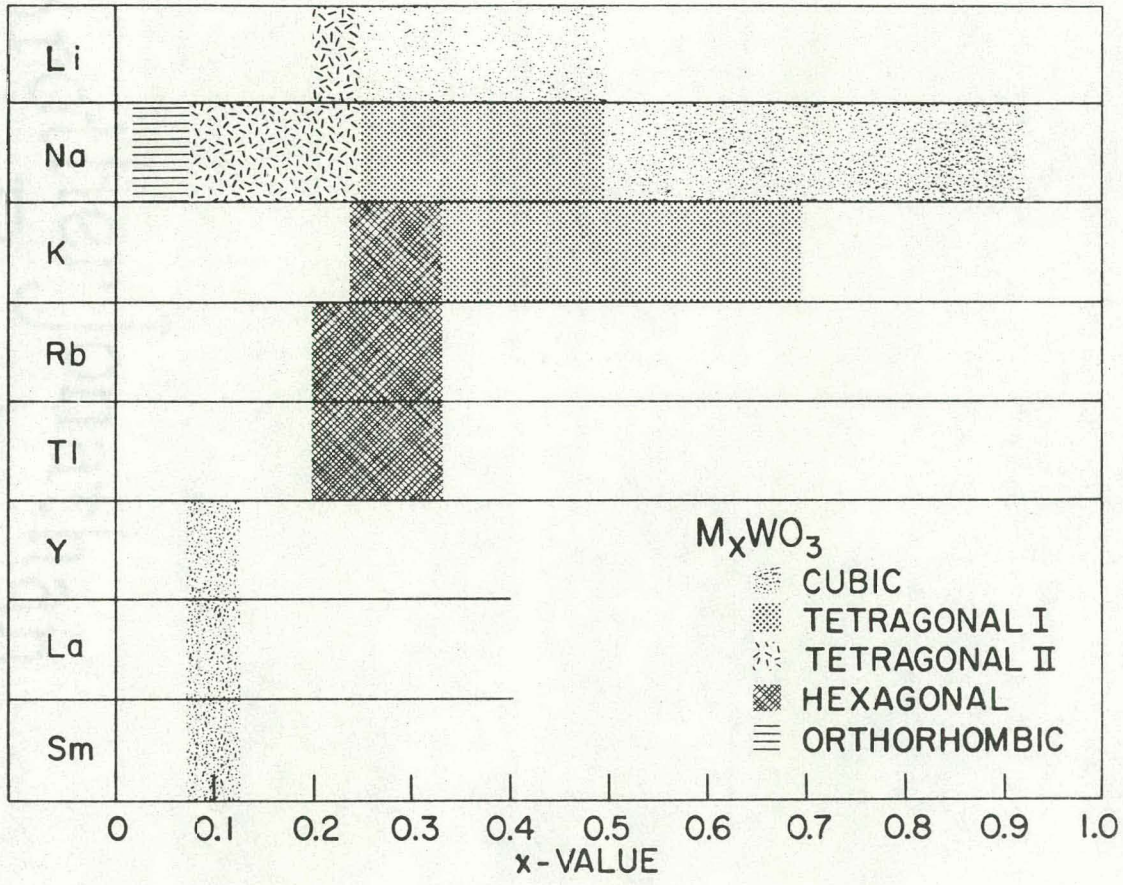

Figure 1.4. Compositions and crystal structures for some tungsten bronzes (8). The cubic sodium tungsten bronze was the primary subject of this investigation, but lithium, potassium, rubidium, and thalium tungsten bronzes were also examined

tetragonal-II structural transition. In the metallic phases, each sodium atom contributes its $3s^1$ electron to the conduction band of the crystal (9, 10). Recently, the band structures of cubic WO_3 and $NaWO_3$ have been calculated (11) and are found to be nearly identical. A rigid band model may, therefore, be used for different sodium concentrations.

Recent investigations (12, 13, 14) have shown that anodization of Na_xWO_3 in acid solutions removes sodium atoms to a depth of several hundred angstroms, leaving a semiconducting layer of low x value Na_xWO_3 on the surface. After anodization, a reversal of the electrode polarity causes the surface to change color from a light green to a deep blue. This color change has been shown to be due to the movement of hydrogen into the empty sodium sites (13, 14). The electronic properties of H_xWO_3 are similar to those of the other bronzes (15).

After Na_xWO_3 was announced to be an excellent electrocatalyst for oxygen reduction, several workers tried to reproduce those results. Experiments by Broyde (16) did not reproduce the spectacular results. Only limited catalytic activity for oxygen reduction was demonstrated on powdered bronzes, including sodium, cerium, and nickel tungsten bronzes. A subsequent paper by Fishman, Henry, and Tessore (17) showed that traces of platinum on the sodium tungsten bronze surface were needed to produce the high catalytic activity. For their experiments, they found that platinum could be deposited on the bronze by dissolving minute traces of Pt from a large Pt electrode in the same test cell. Bockris and McHardy (18) then claimed that only 400 ppm Pt doping of the bronze produced Pt like behavior for oxygen reduction. They assumed that the

surface concentration of Pt was the same as the bulk concentration. Their findings suggested that a synergistic effect for oxygen reduction existed in the platinum-bronze system. However, the findings of Bockris and McHardy (18) on Pt doped single crystals were discounted by Randin (19) and by Weber and Shanks (14) with Pt dopings of up to 1000 ppm and 800 ppm respectively. Recently, the results of Bockris and McHardy were reproduced by Appleby and Van Drunen (20). Platinum pre-electrolysis was used to clean the solutions used in their experiments, as it was in Bockris and McHardy's experiments, but possibilities of Pt contamination were not considered by either group. A number of other papers have dealt with oxygen reduction on pure bronzes (21, 22, 23) and on Pt coated bronze powders (24), but not on Pt doped single crystals. An extensive review of the electrochemistry and general properties of sodium tungsten bronzes is given in the review article by McHardy and Stonehart (25).

Purpose of the Study

These large discrepancies in the literature indicated a need for a careful study of the electrocatalytic activity and surface properties of the tungsten bronzes. All possible factors affecting the catalytic activity of the sodium tungsten bronze system need to be carefully controlled and studied. These factors include: levels of electrolyte impurities, effects of sodium depletion at the crystal surface, effects of surface treatments such as polishing and cleaning, and effects of Pt doping of the crystals and Pt deposition on the crystal surface.

CHAPTER 2. THEORY

The steady state current-voltage curves of the hydrogen and oxygen reactions on platinum electrodes were shown in Figure 1.1. As the current through the electrode-electrolyte interface is increased, the deviation of the potential from the equilibrium values also increases. The exponential dependence of i on η is characteristic of all redox couples. The exponential region of faster reactions, such as the hydrogen reaction, is much shorter and less apparent than in slow reactions. In fact, by definition, a fast reaction is one that can maintain near equilibrium potentials until the higher current densities are reached. At the highest current densities, large deviations of η occur due to diffusion limitations of charge carrier concentrations in the electrolyte at the electrode surface (26, 27, 28). A resistive contribution to the overpotential is always present, but is negligible for sufficiently concentrated electrolytes (0.1 M or greater). Resistive and diffusional contributions to the overvoltage can be made negligible by using a concentrated electrolyte, but the remaining contribution, called the activation overpotential, depends mainly on the electrode itself and not on the electrolyte. The science of electrocatalysis deals directly with the subject of the activation overpotential and the physical parameters that determine its magnitude.

The name activation overpotential arises from the exponential dependence of the current on the overpotential. An exponential dependence implies some sort of activated process. At the solid-

liquid interface, the electrical conduction mechanism changes abruptly from electronic conduction to ionic conduction. For this reason, an activated process must come into play because of differences in the electronic energy levels in the electrolyte and in the electrode. Charge will not flow freely even between equal energy levels because the energy levels are in potential wells on both sides of the interface. The charge carriers must be activated thermally or by applied potentials to pass over the potential barriers. The role of a catalyst is to lower these potential barriers.

At a metal-metal interface, electrical charges flow freely between the two metals until the Fermi levels are equal. However, at a metal-electrolyte interface, charge carriers cannot flow readily from one medium to the other, resulting in a charge build-up at the interface. This charge build-up produces the well-known electrified interface or electrical "double layer" region. The metal-solution potential difference is denoted by $\Delta\phi$ and is an unmeasurable quantity. Only changes in $\Delta\phi$ at an interface, and differences between $\Delta\phi$'s at different electrodes, can be measured (27). The usual scale of emf's is obtained by defining $\Delta\phi$ to be zero for the hydrogen reaction at equilibrium at a metal electrode.

When an external potential is applied to an electrode, $\Delta\phi$ is changed and a current will flow across the interface. The mathematical form of the current-potential relationship may be derived from very general considerations (27, 28). Let ΔG be the activation energy for the process associated with the transfer of an electron from an ion in

solution to an available state in the electrode. ΔG contains both chemical and electrical barrier contributions to the activation energy.

$$\Delta G = \Delta G_{chem} + \beta \Delta \phi e \qquad 2.1$$

The rate of an activated process is then given by

$$\vec{k} = \frac{kT}{h} e^{-\Delta G/kT} \qquad 2.2$$

where

k = Boltzmann's constant

T = temperature in degrees Kelvin

e = charge on an electron

h = Planck's constant

β = fraction of double layer field the electron must traverse.

Since only changes in $\Delta\phi$ may be measured, let

$$\Delta \phi = \Delta \phi_{equil} + \eta \qquad 2.3$$

where η is the deviation of $\Delta\phi$ from the equilibrium value due to an applied potential. So ΔG may be written as

$$\Delta G = \Delta G_{chem} + \beta e \Delta \phi_{equil} + \beta \eta e \qquad 2.4$$

The forward current through the interface is

$$\vec{i} = \vec{k}\, c_A F \qquad 2.5$$

where c_A is the concentration of participating ions in the solution at the interface. Combining equations 2.1 through 2.5, we have

$$\vec{i} = \vec{i}_o e^{-\beta\eta e/kT} \qquad 2.6$$

For the reverse reaction

$$\overleftarrow{i} = \overleftarrow{i}_o e^{(1-\beta)\eta e/kT} \qquad 2.7$$

All of the constants have been grouped together as $\vec{i}_o$ and $\overleftarrow{i}_o$, and have the dimensions of electrical current. With no applied potential, $\vec{i}$ must equal $\overleftarrow{i}$ at equilibrium, so

$$\vec{i}_o = \overleftarrow{i}_o \equiv i_o \qquad 2.8$$

The physical significance of equation 2.8 is that in dynamic equilibrium, the forward and reverse reactions are occurring at the same rate. i_o is a measure of that rate and is called the exchange current. The total current through the interface is given by

$$\begin{aligned} i &= \overleftarrow{i} - \vec{i} \\ &= i_o(e^{(1-\beta)e\,\eta/kT} - e^{-\beta e\,\eta/kT}) \end{aligned} \qquad 2.9$$

Equation 2.9 is called the Butler-Volmer equation after the early researchers whose work led to these ideas. Usually the value of β is close to 0.5. When β equals 0.5, equation 2.9 becomes

$$i = 2i_o \sinh \frac{e\eta}{2kT} \qquad 2.10$$

The exchange current i_o can be measured experimentally. For slow reactions (small i_o), large overpotentials are needed to drive the reaction, that is, $\eta >> \frac{\beta e}{kT}$. Equation 2.9 can then be written

$$\eta \cong a + b \log i \qquad 2.11$$

The exchange current is determined by the intercept a, and β can be found from the slope b. Equation 2.11 is called the Tafel equation and data plotted in the form of equation 2.11 are usually called a Tafel plot. For fast reactions (large i_o) $\eta << \frac{\beta e}{kT}$ and equation 2.9 may be written as

$$i \cong i_o \frac{\beta \eta e}{kT} \qquad 2.12$$

The exchange current may then be found from the slope of the graph if β is known. Experimental measurements are possible in both the linear and exponential regions for many reactions.

Simple derivations such as this one cannot predict a value for either i_o or β. A microscopic theory is needed. Detailed theories of simple one electron transfer reactions have been developed (29 → 34), but usually i_o is left as an adjustable parameter because of the difficulties involved in the calculations. The theory of Levich et al. correctly predicted a direct proportionality of i_o to the density of states at the fermi level ($N(E_f)$) of the metal, and an exponential dependence of i_o on temperature. However, an exchange integral involving the interaction of the ion in solution with the electrons in the solid was not calculated and was left as an adjustable parameter to i_o (32).

Equation 2.9 has been derived for only simple, one step, one electron transfer reactions, but the equation can be generalized for multistep reactions involving many steps, each of which may or may not involve a transfer of electric charge. The generalization is valid only if one of

the steps is much slower than the other steps. This situation of one "rate determining step" is a common one in electrode reactions. Simple redox reactions are obviously controlled only by the rate of electron transfer since that is the only step in the reaction. More complicated reactions, which involve the adsorption of molecules, breaking of chemical bonds, and formation of final products, have a large number of possible rate determining steps. The step which will be rate determining often cannot be predicted and must be found experimentally.

Generalization of the Butler-Volmer equation for multistep reactions requires the assumption of a rate-determining step (rds) which is much slower than any of the other steps. The rds need not be an electron transfer step. Complete details of the derivation of the generalized Butler-Volmer equation are given in the texts by Bockris and Reddy (27) and Erdey Grúz (28), and only the final result will be given here. The total current is again given by a sum of anodic and cathodic currents:

$$i = \overleftarrow{i} - \overrightarrow{i}$$

$$= i_o \left(\exp\left[\left(\frac{n-\gamma}{\nu} - r\beta\right)\frac{ne}{kT}\right] - \exp\left[-\left(\frac{\gamma}{\nu} + r\beta\right)\frac{ne}{kT}\right]\right) \qquad 2.13$$

where

n = total number of electrons transferred in the reaction

ν = number of times the rds must be repeated for the overall reaction to occur once (stoichiometric number)

γ = number of charge transfer steps preceeding the rds

β = fraction of double layer field an electron must cross

$r = 1$ if the rds is an electron transfer step

$r = 0$ if the rds is a chemical step

Now let

$$\overleftarrow{\alpha} = \frac{n-\gamma}{\nu} - r\beta$$

$$\overrightarrow{\alpha} = \frac{\gamma}{\nu} + r\beta$$

so

$$i = i_o \left(e^{\overleftarrow{\alpha}\, \eta e/kT} - e^{-\overrightarrow{\alpha}\, \eta e/kT}\right) \qquad 2.14$$

Equation 2.14 is the generalized Butler-Volmer equation with $\overleftarrow{\alpha}$ and $\overrightarrow{\alpha}$ analogous to $1-\beta$ and β respectively. The sum of $\overleftarrow{\alpha}$ and $\overrightarrow{\alpha}$ is not always unity but is easily seen to be n/ν, so

$$\nu = \frac{n}{\overrightarrow{\alpha} + \overleftarrow{\alpha}} \qquad 2.15$$

Equation 2.14 can be used with the experimentally determined tafel slopes, along with the pH and pO_2 dependence of the reaction rate to determine the mechanism of the oxygen reaction (27, 35, 36).

The Oxygen Reaction

The overall reaction in acid solutions is usually written

$$O_2 + 4H^+ + 4e \rightleftarrows 2H_2O \qquad E_o = 1.23$$

Four electrons must be transferred from the electrode to some intermediate chemical species in the solution during the course of the reaction. The total number of steps in the oxygen reaction varies with the model assumed for the reaction path. The most likely reaction path on most materials, discussed by Hoare (4), and more recently by Yeager (2), is the "peroxide path". The reaction steps are listed:

i) $M\ (\text{adsorption site}) + O_2 \rightleftarrows MO_2$ adsorption

ii) $(O_2)_{ads} + e^- \rightleftarrows (O_2^-)_{ads}$ electron transfer

iii) $(O_2^-)_{ads} + H^+ \rightleftarrows (HO_2)_{ads}$ reaction with H^+

iv) $(HO_2)_{ads} + e^- \rightleftarrows (HO_2^-)_{ads}$ electron transfer

v) $(HO_2^-) + H^+ \rightleftarrows (H_2O_2)_{ads}$ reaction with H^+

Step v is the production of hydrogen peroxide. The completion of the reaction requires that the electrode also be a good catalyst for the reduction of H_2O_2 to water. Several reaction paths are possible for the reduction of H_2O_2 to water (4, 28). The overall reaction is

$$2(H_2O_2)_{ads} \rightleftarrows 2H_2O + O_2$$

Even though step ii is regarded as the rds, the slow reaction rate for O_2 reduction is in part due to the formation of H_2O_2, which leads to higher electrode overvoltages. A catalyst on which O_2 is dissociatively adsorbed would allow for the direct reduction of oxygen atoms to water. Instead, on present catalysts, the O-O bond is not broken until after the formation of H_2O_2 (37).

Step ii is probably the rds since η depends on temperature and partial pressure of O_2 (4), and satisfies equation 2.15 for ν. Step ii must be repeated four times so the stochiometric number ν is 4, which implies $\vec{\alpha}$ must equal 0.5. Experimentally determined values of $\vec{\alpha}$ are close to 0.6.

Exchange currents of simple one electron transfer reactions are approximately proportional to the density of states at the Fermi level of

the electrode. Reactions are characterized as "simple" when the condition of a very weak interaction exists between the reactant and the electrode. A strong interaction between an ion and an electrode would probably slow a reaction which involves only the arrival of an ion at the surface, transfer of electrical charge, and the random departure of the ion with that charge. A reaction such as an electron transfer to an oxygen molecule is less probable and requires a strong interaction between the O_2 molecule and the electrode. This is just another way of saying the reaction must be catalyzed. In such a case, the property of an electrode material that determines the reaction rate may not be the number of electrons available for transfer, but may be the nature of the reactant-electrode interaction that permits the reaction to proceed. Thus, binary and ternary compounds, many of them semiconductors, are being investigated for use as oxygen electrodes because of their properties that may catalyze the oxygen reaction. Semiconductors offer a large number of catalytic surfaces that are stable in acidic or basic solutions. The interaction of reaction intermediates with band gap surface states on semiconductors has recently been discussed by Gerischer (38).

Non-Steady-State Techniques

As is often the case in physical research much information can be gained from dynamic, as opposed to static or steady-state, measurements. A number of dynamic current-voltage measurements and their theoretical i-v relationships are available to researchers studying the solid-liquid interface. Either the current or potential may be arranged to vary with time according to a variety of waveforms and the resulting potentials or

currents monitored and recorded. Various waveforms employed include sine-wave, sawtooth, square, and triangular waveforms. A powerful technique in this class of measurements is linear sweep cyclic voltammetry, normally referred to just as cyclic voltammetry (CV). The experimental arrangement involves a triangular waveform for the electrode potential with the resulting current being monitored on an x-y recorder or oscilloscope, depending on the scan rate. Cyclic voltammetry is an extension or modification of the simpler linear potential scan experiment. The latter technique involves only a linear voltage sweep between two given potentials while monitoring the electrode current. In the cyclic voltammetry experiment, the potential is swept linearly from one potential to another and back again. The number of cycles used depends on the information desired about the electrode or the solution.

Cyclic voltammetry is employed to study two general types of electrode-electrolyte interactions: one is the study of redox reactions which can be made to occur at the interface, and the other is the study of changes in the electrode surface itself which are caused by interactions with the electrolyte. An example of the first type would be the use of CV as a probe to detect traces of an electro-active species in the solution. An example of the second type would be using CV to study the formation of an oxide layer on the electrode surface. In general, the first type involves an inert electrode being used as a probe to study the solution, while the second type of experiment involves the study of the properties of the electrode itself in a certain electrolyte. Furthermore, an unknown reaction occurring at the electrode surface can be experimentally distinguished as belonging to the first or second class of reactions, usually by immediate

examination of the CV curves. Redox reactions produce diffusion limited currents while the surface reactions are limited by the range of zero to to one monolayer coverage. These two physical processes and sometimes the kinetics of the reaction determine the shape of the i-v curve obtained by CV. A good example of a CV curve is shown in Figure 2.1. The current on the return sweep (cathodic or negative current) is usually plotted below the anodic sweep for easy comparison of the anodic and cathodic sweeps. Four parameters can be obtained from curves such as this: the peak currents I_{pa} and I_{pc} on the anodic and cathodic sweeps, and the potentials at which these peaks occur, E_{pa} and E_{pc}. A derivation of the mathematical form of these i-v curves is quite long and tedious so only a summary of the results will be given here, starting with the diffusion limited processes. Mathematical details and extensive references (for diffusion limited CV) are given in the excellent review articles by Brown and Large (39) and Adams (40).

Assume that the oxidized form of a reversible redox couple is present in a solution which is already made conducting by a supporting electrolyte. The reaction occuring as the potential is swept forward and back is

$$O + ne^- \rightleftarrows R$$

The time varying potential V(t) can be written as

$$V(t) = V_i - St \qquad 0 \leq t \leq t_r$$

$$= V_i - 2St_r + St \qquad t \geq t_r$$

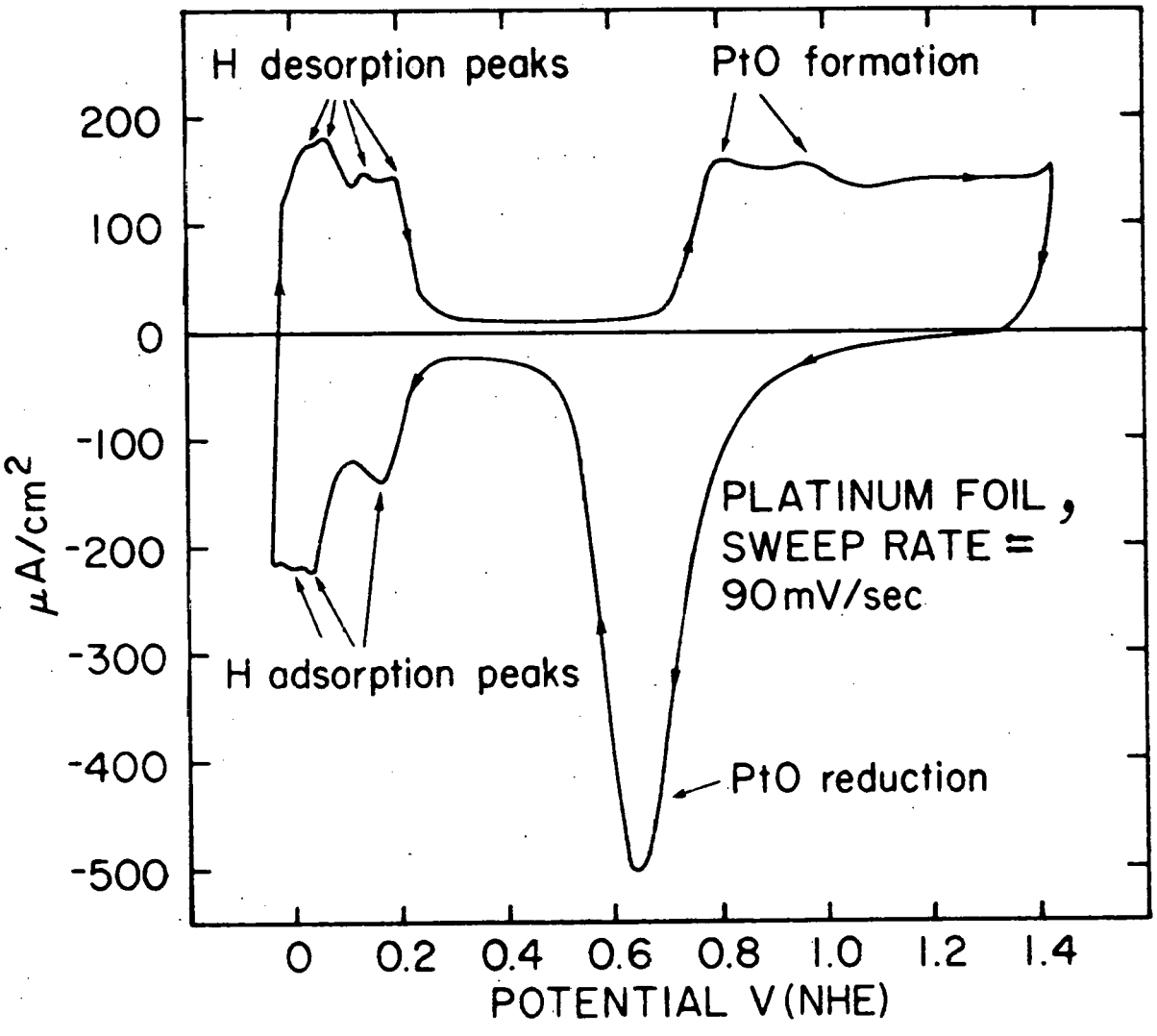

Figure 2.1. CV curve taken in high purity test cell (Appendix A) on a large (20 cm^2) Pt foil. The well-defined peaks and the absence of peaks due to any other reactions are indicative of the high purity of the experimental system

where V_i is the starting potential, t_r corresponds to the peak of the triangular wave, and S is the potential scan rate. The current function is derived by solving Fick's law of diffusion, using the Nernst equation to relate the potential to the concentrations of O and R. Provided that the reaction occurs fast enough, the current is proportional to the flux of reactants diffusing to the electrode surface. A reaction which meets this condition is termed a "reversible" reaction because electrochemical equilibrium is maintained at the electrode.

$$\frac{\partial C(x,t)}{\partial t} = D \frac{\partial^2 C(x,t)}{\partial x^2} \qquad 2.16$$

$$E = E^o + \frac{RT}{nF} \ln \frac{C_O}{C_R} \qquad 2.17$$

$$i(t) = nFA\, D \frac{\partial C_O(0,t)}{\partial x} \qquad 2.18$$

where

$C_O(x,t)$ = concentration of the oxidized species O

$C_R(x,t)$ = concentration of the reduced species R

D_O and D_R are the diffusion coefficients of O and R respectively

F = Faraday's constant

R = gas constant

A = area of the electrode

n = number of electrons transferred in the reaction.

The current as a function of time is found to be

$$i(t) = nFA\, C_O^* \left(\frac{\pi D_O nF}{RT}\right)^{\frac{1}{2}} S^{\frac{1}{2}}\, \chi(at) \qquad 2.19$$

where

C_0^* = bulk concentration of oxidized species 0

$a = \frac{nFS}{RT}$

The function $\chi(at)$ must be obtained by a numerical technique, and a table with values of $\chi(at)$ for 5mV increments in (at) has been published by Nicholson and Shain (41). The form of the curve is contained entirely in $\chi(at)$ and the magnitude of the current at any potential is determined by the constants in equation 2.19. However, no information is contained in the form of the curve since the form is the same for all curves. The peak currents and the potentials at which the peaks occur contain the desired information. The peak current for the forward potential sweep is given by

$$i_{pa} = 2.69 \times 10^5 \, n^{3/2} A \, D_0^{\frac{1}{2}} C_0^* S^{\frac{1}{2}} \qquad 2.20$$

On the reverse scan i_{pc} has the same value. The peak current i_p is proportional to the original concentration C_0^* of the oxidized species 0 in the solution and also is proportional to the square root of the potential scan rate S. The following relationships hold for a reversible voltametric i-v response:

$V_{pa} - V_{pc} = \frac{59}{n}$ mV at 25°C and is independent of S

E_{pa} and E_{pc} are independent of S

$i_p/S^{\frac{1}{2}}$ is independent of S

$i_{pa}/i_{pc} = 1$, independent of S

The 59mV separation of the current peaks is a result of a diffusion limited process and in no way represents an activation energy for the reaction. The number 59 is determined by $(\log \frac{1}{e}) \frac{RT}{F}$ at 25°C.

Slower reactions that cannot maintain electrochemical equilibrium as the potential is changed are controlled both by the diffusion limited current and by charge transfer kinetics. Such reactions are termed quasi-reversible. There is no distinct physical difference between a reversible and a quasi-reversible reaction other than the exchange current, i_o, for such a reaction is so small that a diffusion limited current is not obtained until high potentials are reached on the voltage scan. In the theoretical analysis, the Butler-Volmer equation is used in place of the Nernst equation to relate the concentrations $C_0(0,t)$ and $C_R(0,t)$ to the electrode potential. The magnitudes of the concentrations are contained in the constant i_o, so the Butler-Volmer equation, equation 2.14, is re-written as

$$i(t) = nFA\, C_0(0,t)\, k_s e^{\frac{\alpha nF}{RT}(E(t) - E^\circ)} - nFA\, C_R(0,t) k_s e^{-\frac{(1-\alpha)nF}{RT}(E(t)-E^\circ)}$$

where k_s is the charge transfer rate constant for the reaction. The following relationships hold for a quasi-reversible i-v response:

$E_{pa} - E_{pc}$ approaches $\frac{59}{n}$ mV only as $S \to 0$

$I_p/S^{\frac{1}{2}}$ is virtually independent of S

$i_{pa}/i_{pc} = 1$ only if $\alpha = 0.5$

Reactions for which the rate constant is extremely small are called irreversible reactions. The anodic and cathodic current peaks are widely

separated in potential and sometimes no current flows on the reverse scan, depending on the degree of irreversibility of the reaction. The peak current is still proportional to $S^{\frac{1}{2}}$ however. The theoretical analysis of the problem is simpler than for the quasi-reversible case because the reverse reaction can be neglected and only one term of the Butler-Volmer equation is needed. This same approximation was used to derive the Tafel equation (2.11).

Cyclic voltammetry was not used as a tool to study the electrode surface itself until after the paper by Will and Knorr (42) who studied the adsorption of hydrogen and oxygen on platinum. Surface CV explores the process whereby some species is chemisorbed onto the electrode surface. Current ceases to flow after the surface is entirely covered by the adsorbate or completely stripped of it on the reverse scan. The CV plot in Figure 2.1 is a good example of such a process. A rigorous mathematical analysis of CV for surface reactions was given by Srinivasan and Gileadi (43). The equations that govern the i-v characteristics are the forward and reverse components of the Butler-Volmer equation (2.14) multiplied by the surface coverage fractions θ_A and $(1-\theta_A)$. If the surface reaction is

$$A^{n-} + M \underset{\leftarrow}{\rightarrow} M\,A_{ads} + ne^-$$

then

$$\vec{i} = nF\vec{k}\,(1-\theta_A)C_A\,e^{\beta VF/RT} \qquad 2.21$$

$$\overleftarrow{i} = nF\overleftarrow{k}\,\theta_A\,e^{-(1-\beta)VF/RT} \qquad 2.22$$

$\vec{i} \rightarrow 0$ as $\theta_A \rightarrow 1$, and $\overleftarrow{i} \rightarrow 0$ as $\theta_A \rightarrow 0$

The coverage fraction θ_A is found by integrating the total current

$$\theta_A = \frac{\int i_t dt}{Q} \qquad 2.23$$

where Q is the charge corresponding to full coverage by A.

Since the adsorbed layer essentially "stores" charge, it can be throught of as contributing to the electrode capacitance. This capacitance is called the adsorption pseudo-capacitance. So the electrode capacitance is composed of the double layer charging capacitance $C_{d.l.}$, and the adsorption pseudo-capacitance C_A. Usually $C_{d.l.} << C_A$. By definition

$$i = \frac{dq}{dt} = \frac{dq}{dV} \cdot \frac{dV}{dt}$$

$$= \frac{dq}{dV} \cdot S$$

$i = C \cdot S$ (by definition of the capacitance C)

so

$$i = C_{d.l.} S + C_A S$$

$$i \cong C_A S \qquad 2.24$$

By these general considerations it is easily seen that the current at all times is directly proportional to the scan rate S, and the proportionality constant is the adsorption pseudocapacitance. The form of the capacitance curve then determines the form of the current function. A detailed calculation, using equations 2.21 → 2.23, yields for a reversible reaction:

$$i = \frac{QF}{RT} \frac{K_1 e^{-VF/RT}}{(e^{-VF/RT} + K_1)^2} \cdot S$$

$$i_p = \frac{QF}{4RT} \cdot S \qquad 2.25$$

$$V_p = -\frac{RT}{F} \ln K_1, \quad K_1 = \frac{\vec{k}}{\overleftarrow{k}} \qquad 2.26$$

θ_A is equal to 0.5 at the current peak. The reverse scan is identical for a reversible reaction.

For an irreversible reaction, the reverse current can be ignored, that is, only equation 2.21 or 2.22 is used, but not the sum. In this case

$$i_p = \frac{1}{e} \cdot \frac{Q\beta F}{RT} \cdot S \qquad 2.27$$

$$\theta_p = 1 - \frac{1}{e} = 0.63$$

$$V_p = \frac{RT}{\theta F} \ln \frac{Q\beta F}{RT} + \frac{RT}{\theta F} \ln S \qquad 2.28$$

In this case, the forward and reverse scans are not alike. The peaks are shifted to higher potentials with increasing scan rate, and a θ_p equal to 0.63 means that a current peak is not symmetrical about V_p.

For the quasi-equilibrium case, the peak current is proportional to the scan rate S, as in the two previous cases, and the peak potential shifts, but the shift is a function of sweep rate. At high sweep rates, the quasi-equilibrium case displays the functional characteristics of the irreversible case.

In all of the above considerations, any mutual interactions of the adsorbed species were ignored. This approximation may not be valid for many adsorbed particles. A repulsive interaction between adsorbed particles will both broaden the current peak, lowering i_p, and shift the peak potentials, V_p, to higher values of the potential (44).

CHAPTER 3. EXPERIMENTAL

Crystal Growth

All measurements in this study were done on single crystals of the tungsten bronzes. The alkali tungsten bronze crystals were prepared by the electrolysis of a fused salt of the respective alkali tungstate and tungsten trioxide as described by Shanks (8). For the sodium tungsten bronze crystals grown, a seed crystal was not needed. Crystal growth was initiated from the tip of a gold wire drawn up a few millimeters from the end of a 2 mm O.D. quartz tube. Single crystals, approximately 2 cm on an edge, were normally obtained with a composition of $Na_{0.7}WO_3$. Platinum doping was achieved by the use of a Pt anode in the melt. The crystal used for the electrochemical studies contained 800 ppm Pt as determined by mass spectroscopic analysis.

Sample Preparation

For the electrochemical studies, these crystals were either cleaved or cut on a high speed diamond saw into smaller pieces, a typical sample size being 4 mm x 4 mm x 6 mm. The cleaved crystals were cleaned in boiling conductivity water, but the crystals cut on the diamond saw required a more elaborate cleaning procedure. A special wax (Aremco Products, Inc. crystal bond 509 adhesive) was used to mount the crystals on the diamond saw, and mineral oil was used to cool the blade. These contaminants were removed first by boiling ethyl acetate, followed by hot concentrated NaOH and finally by boiling conductivity water. The samples cut on the diamond saw were then either polished, or one end

was cleaved away to ensure a fresh, pure bronze surface. Polishing was performed after the crystal was mounted in teflon. Teflon mounting was performed using the method described by Nagy and McHardy (45). Sample mounting and electrical connection are illustrated in Figure 3.1.

The polishing procedure consisted of mechanical polishing on microcloth with alumina powder down to 0.05 μm particle size. Immediately before insertion into the cell, all samples were washed with acetone, then with isopropyl alcohol. The final cleaning was done with an isopropyl vapor phase degreaser. The area of each sample was determined from a photograph of the mounted crystal, with no corrections being made for surface roughness. After insertion into the cell, the potential on each electrode was cycled between -0.1 V and 1.6 V NHE for approximately twenty minutes to further clean the surface. Only small changes in the cyclic voltammetry curves were observed during this time.

Platinum Deposition

To test for a synergistic effect with Pt, a series of samples with increasing surface concentrations of Pt was made by plating in dilute chloroplatinic acid. A rotating electrode system was used for plating all samples, with a rotation speed of 900 rpm. The plating voltage was +0.120 V NHE and the plating times ranged from a few minutes to 3.5 hours. A base solution of 0.3 M HCl was used to provide a high conductivity for the plating solution. Cleaved samples were not used for plating because SEM photographs revealed large (1 μm) Pt platelets formed on the crystal, so all samples were polished before plating.

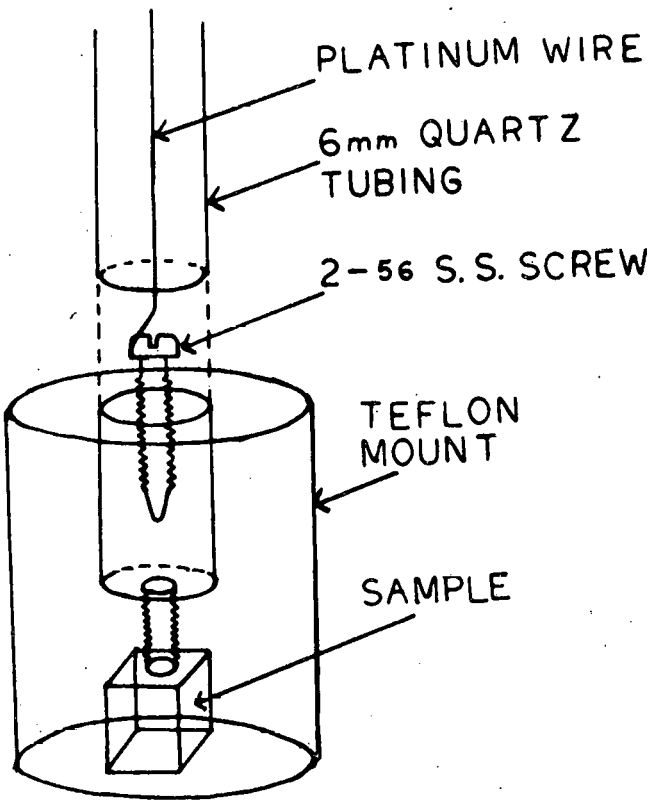

Figure 3.1. Sample mounting and electrical connection for the tungsten bronze samples

However, it was noted that Pt black deposits would not adhere to a fresh, thoroughly cleaned bronze surface. Therefore, all samples to be platinized were first anodized at 1 mA/cm^2 anodic until the potential reached 9 volts. The potential required approximately 9 hours to reach 9 volts. With this procedure, any amount of Pt from a fraction of a monolayer to Pt black could be plated onto the crystals.

The plating current was not at all indicative of the amount of platinum that adhered to the crystal. Auger analysis of platinized crystals revealed several orders of magnitude less platinum on the crystal surface than the amount calculated from the plating current. Fortunately, the amount of platinum on the crystal surface was found to be proportional to the plating time, up to a certain critical time after which platinum black rapidly formed on the surface. Apparently, a more diluted solution than the 7.5×10^{-5} M H_2PtCl_6 solution used would have been sufficient.

Platinum was deposited on several additional samples by two other methods. Both methods involve the in situ dissolution of a Pt electrode. With the first method, a large (20 cm^2) shiny Pt electrode was used as the counter electrode for cycling a preanodized bronze electrode between -0.2 V and 1.8 V NHE for approximately 12 hours. The sweep rate was 100 mV/sec. After using this procedure on two bronze electrodes, the solution was analyzed for Pt by an inductively coupled plasma method. The solution was found to contain 0.093 µg/ml of Pt, and the original solution volume was 100 ml. The second method was a variation on the first, in that the large (20 cm^2) Pt electrode itself was cycled between

0.0 V and 1.50 V NHE using the hydrogen-gold counter electrode. The Pt electrode was cycled for 3.5 hours in helium saturated 0.1 N H_2SO_4 solution. Oxygen was then passed into the cell and a bronze electrode lowered into the solution. An anodic current of 400 $\mu A/cm^2$ was passed for 1.5 hours, and then a cathodic current of 400 $\mu A/cm^2$ was passed. The initial cathodic potentials were low, but quickly increased with time, on the order of a few minutes.

Test Cell and Distillation Unit

Research in some areas of electrochemistry requires ultra high purity experimental conditions before reliable information can be obtained (46). The most notable problem area in this regard is the electrochemistry of oxygen. The correct rest potential of 1.23 volts vs. H.E. for oxygen reduction in acid solutions can be obtained only under incredibly stringent conditions of purity and on carefully prepared electrodes (47-49). Fortunately, a good Tafel plot, with the correct slope and exchange current, can be obtained under somewhat less stringent conditions, but the problem is still serious.

A common practice that has come into being is that of "pre-electrolyzing" the solution, usually with large platinum electrodes (35). However, it is now known that trace amounts of platinum are dissolved from these electrodes (13) and can even plate out onto the test electrodes (17). If the electrode being studied is also platinum, then no problem should result, but such a situation limits the use of pre-electrolysis to a minority of experiments. Therefore, a cell of

sufficiently high purity must be constructed which will permit studies of oxygen reduction to be performed without the use of pre-electrolysis. Such a cell must also be connected to a high purity water distillation unit that permits the in situ distillation of water and solution preparation.

A review of the literature indicates the features necessary for a high purity still. The recommended construction materials are glass, preferably quartz, and teflon (50, 51). Oxygen can be bubbled through the system to oxidize the organic impurities in the water and to carry off any dissolved gases in the water (46, 51). The oxygen bubbles also prevent bumping of the distillate. An efficient spray trap (52) and a throat heater (51) are recommended for high purity stills. The spray trap is an important component of commercially available high purity stills such as the Barnstead brand stills. Feed water for the high purity still should be water distilled from a potassium permanganate-potassium hydroxide solution. The permanganate is a very strong oxidizer and attacks the organic impurities present in ordinary "tap distilled" or deionized water.

Technical details of the still are given in Appendix A.

The electrochemical cell used was a three compartment cell constructed entirely of quartz and teflon. The counter electrode was a gold foil with H_2 gas bubbled over it. A palladium hydride electrode (53) was used as a reference electrode. The Pd-H electrode was constantly checked against a saturated calomel reference electrode since its potential tended to drift for long times after recharging with

hydrogen. Thus all potentials given here are referenced to the normal hydrogen electrode using the relation

$$V_{NHE} = V_{SCE} + 0.242 \text{ V} \quad .$$

Since the effects of traces of Pt were being investigated, no Pt electrodes touched the solutions used for studies on the bronzes, except where intentional Pt contamination was desired. For this reason, the standard pre-electrolysis of the solution was not carried out. The details of the test cell are given in Appendix A.

Extensive efforts were made to purify the gases bubbled into the cell. "Zero oxygen" with <0.2 ppm total hydrocarbons (THC) was passed through a quartz tube of platinized asbestos at 450°C, then over moist KOH and then through two traps containing Linde 13X molecular sieve. When an inert atmosphere was needed, 99.998 percent pure "zero helium" (<0.5 ppm THC) was passed over hot copper turnings and through two liquid N_2 cooled cold traps also containing Linde 13X molecular sieve. The gas handling system was constructed entirely of acid cleaned stainless steel and pyrex tubing, with Fischer and Porter glass-teflon valves and S. S. Swagelock tubing connectors.

The degree of cleanliness of the system is indicated in Figure 3.2 by a cyclic voltage scan on a high purity Pt electrode. The Pt electrode was mounted in teflon and polished in the same manner as described above for the bronze samples. Well defined hydrogen adsorption and desorption peaks, and platinum oxide formation and reduction peaks are observed. No impurity oxidation peaks were observed at lower sweep

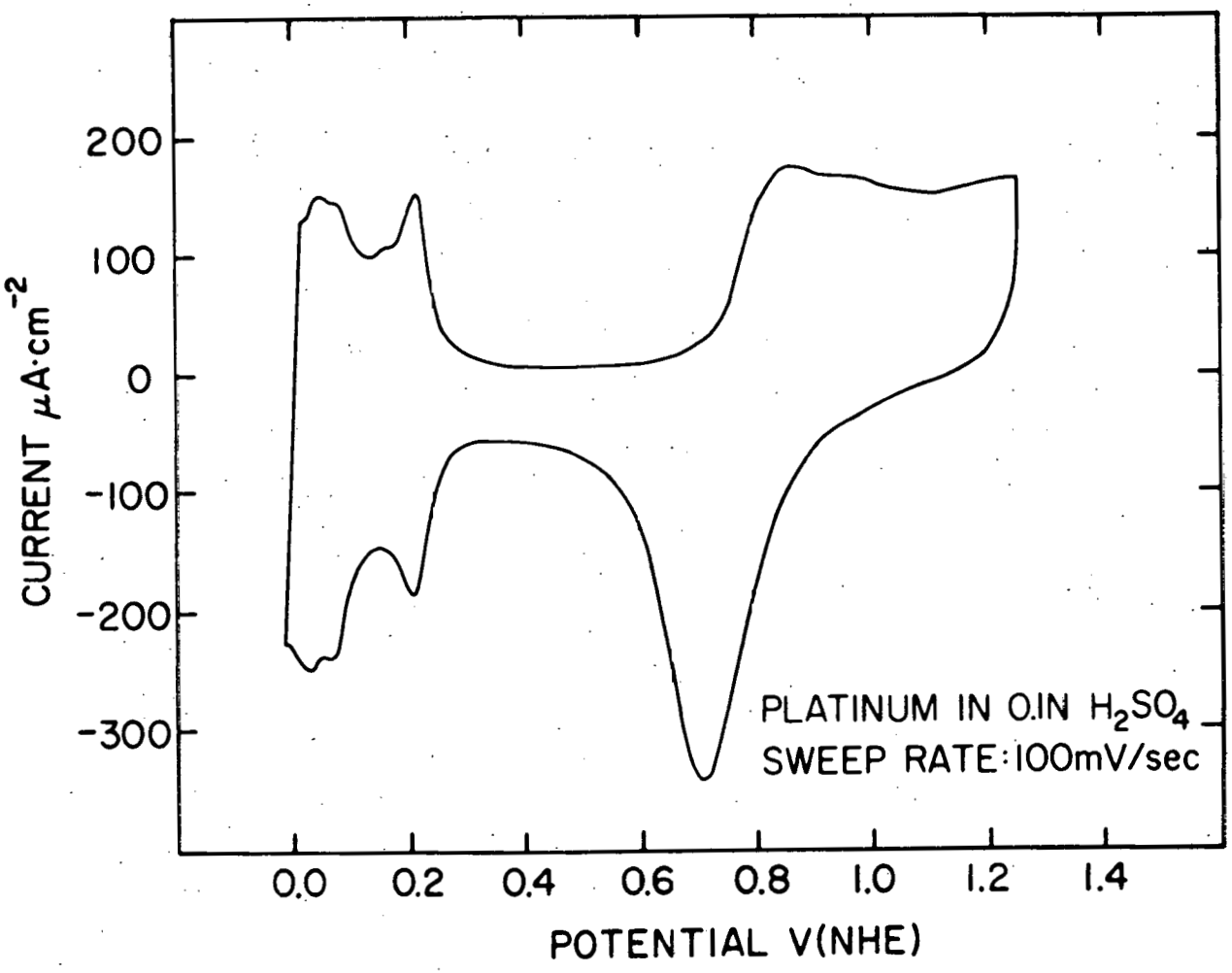

Figure 3.2. CV curve for Pt, taken in the high purity test cell. The large negative background current between 0.2 and 0.6 volts is due to traces of O_2 remaining in the cell. The well-defined H_2 adsorbtion and desorption peaks near 0.0 V, and the PtO formation and reduction peaks near 0.7 V indicate very pure experimental conditions in the cell

rates or when the solution was stirred. Rest potentials on the Pt test electrode in fresh solution were normally around 0.98 volts NHE. The only solution used in the cell for this study was 0.1 N H_2SO_4 (pH 1.2) mixed *in situ* from Apache Chemicals 99.9999% pure (distilled in Vycor) sulfuric acid.

Experimental Techniques

Three experimental techniques were used to study the catalytic, electrochemical, and chemical properties of the tungsten bronzes. The catalytic activity of a sample for the oxygen or hydrogen reaction was determined from the Tafel plots of the current-potential data. General electrochemical properties of the bronzes, including stability to corrosion or dissolution, were studied by linear sweep cyclic voltammetry. Chemical compositional analysis of the electrode surfaces was performed by Auger Electron Spectroscopy. In addition, SEM photographs helped reveal the surface morphology for the cases of cleaved, polished, and platinum-plated samples.

Data for the Tafel plots on all samples were obtained galvanostatically, in the current density range 10^{-3} A/cm^2 to 10^{-8} A/cm^2. Currents were generated with a very stable, constant current power supply (Appendix B). All samples required from 2 to 5 hours at each data point to reach a steady state potential. Steady state was defined to be a potential drift of less than 1 mV/10 min. True steady state conditions were checked by allowing 9 hours for the steady state condition to occur on approximately 1/6 of all data points. Also, the first point was

allowed at least eight hours to reach steady state. This procedure insured reproducible curves. Data were taken by starting at high currents and decreasing the current by halving it for each succeeding point. For a valid comparison to pure Pt, the Tafel plot on the Pt sample was obtained in exactly the same manner. For this reason, the Tafel plot shown for Pt is somewhat different than the data usually seen in the literature. A Keithley model 640 electrometer was used to measure the potentials, while its output was read on a Dymec model 2401A five digit integrating DVM. All potentiodynamic scans and Pt plating were done with a PAR model 173/176 potentiostat/galvanostat. All measurements were made at 25°C ± 2°C. The term galvanostatic refers to constant current measurements for which the current is held fixed and the potential is allowed to reach a steady-state condition. For potentiostatic measurements, the potential across the interface is held fixed and the current is allowed to reach a steady state. A schematic diagram of the constant current arrangement is shown in Figure 3.3. Only one electrode is studied at a time, the other electrode being used only out of the necessity of completing the electrical circuit. This "other" electrode is usually called the "counter electrode" from the German name gegen-electrode. The two electrodes are often put in separate compartments, separated by a porous membrane. The membrane prevents any contamination of the test compartment by chemical species produced at the counter electrode, for example molecular hydrogen. Most experimentally measured potentials are obtained by means of a comparison to a third, or reference, electrode. In the arrangement shown in Figure 3.3, the physical

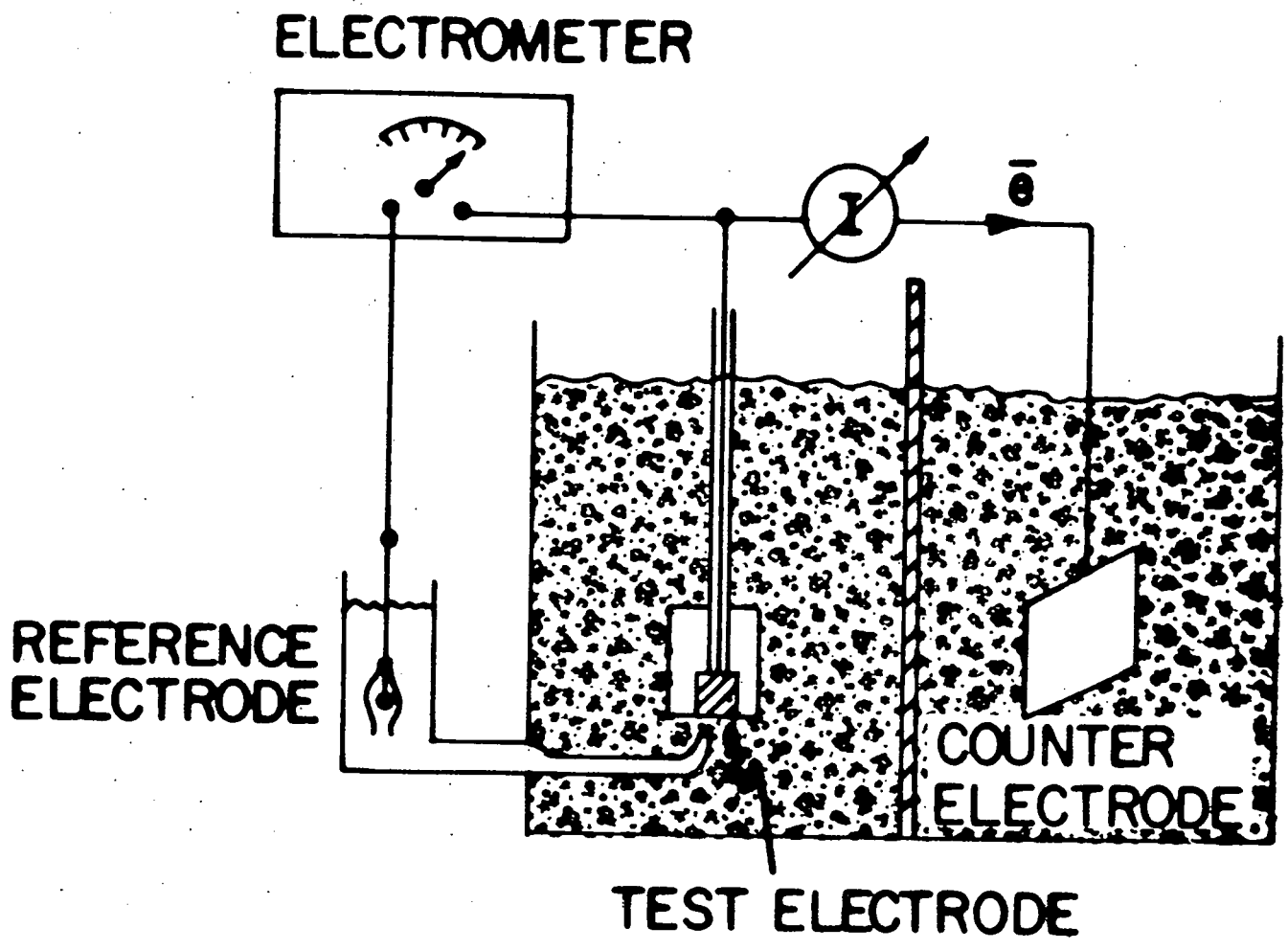

Figure 3.3. Schematic experimental arrangement for measurement of the steady-state i-v characteristics of the test electrode. The center divider is a porous membrane and the counter electrode is usually gold or platinum with H_2 gas bubbled past it. The electrometer is measuring the voltage drop across the test electrode-electrolyte interface.

parameter being measured is the voltage drop across the test electrode-electrolyte interface. Electrical connection to the back of the electrode is generally a simple matter, although an ohmic contact must be made if only a 3 probe experiment is used. Electrical connection to the electrolyte side of the interface is made by a reference electrode through a glass capillary. Ohmic contacts can never be made to an electrolyte, because any metal probe will have a potential drop across the interface. The next best thing is a standard, reproducible contact potential, so all potentials are known to within a constant. Several standard reference electrodes are commonly used, but all can be referenced to the hydrogen electrode, which is defined as the zero on the emf scale.

The Auger depth profiles of the platinized crystals were carried out with a Phi-Electronics Industries, Inc. Auger Electron Spectroscopy unit. The primary electron beam current was 5 μA at 4 keV with a spot diameter of 50 μm. Elemental abundances were determined from the peak to peak AES signals after correction for the Auger sensitivity factor for each element. The Auger analysis was carried out during continuous sputtering of the crystal surface by argon ions at 2.5 keV generated by a 3M Minibeam ion gun. To eliminate any crater edge effects, the ion beam was rastered over a 3 mm^2 area, and the Auger electron beam was centered in this area. The sputtered depth was calculated by assuming an average sputtering yield of two for sodium tungsten bronze. At the start of analysis, sputtering was carried out slowly, using a 30 nA ion beam, which gives a calculated sputtering rate of 1 Å/min. At greater depths, where the concentration profiles were changing more slowly, the

sputtering was performed at increasingly higher rates.

Sodium and oxygen are very difficult constituents to analyze with Auger spectroscopy because of uncertainties in their sensitivity factors. To obtain an accurate value of the sensitivity factor, an elemental sample must first be analyzed, but this becomes difficult for elements such as sodium or oxygen. Compounds having one of these elements as a component are usually used as standards, but considerable changes in the surface composition of the compound can occur by electron beam induced desorption or by preferential sputtering if an ion beam is used to sputter clean the surface. The problem of preferential sputtering inevitably arises if a depth profile of the sample is performed. Our measurements on the sodium tungsten bronzes consistently gave too low a value for both the sodium and oxygen concentrations on cleaved $Na_{0.7}WO_3$ samples. Oxygen stochiometries of 2 to 2.5 and sodium x values of 0.5 were generally observed, indicating that the surface was depleted of these elements.

An Auger spectrum taken on a clean sodium tungsten bronze with an x-value of 0.7 is shown in Figure 3.4. The recorder trace shown is the derivative of the electron spectrum N(E) emitted from the sample which was bombarded with a primary electron beam of several thousand electron volts. The numbers in parentheses are the Auger line energies in electron volts. The elastic peak lies at the far end of the spectrum and is not shown. The carbon signal shown is small, indicating a very clean surface on this sample. Oxygen has one peak at 510 eV, and sodium has one peak at 990 eV. Tungsten has several peaks, both at low and

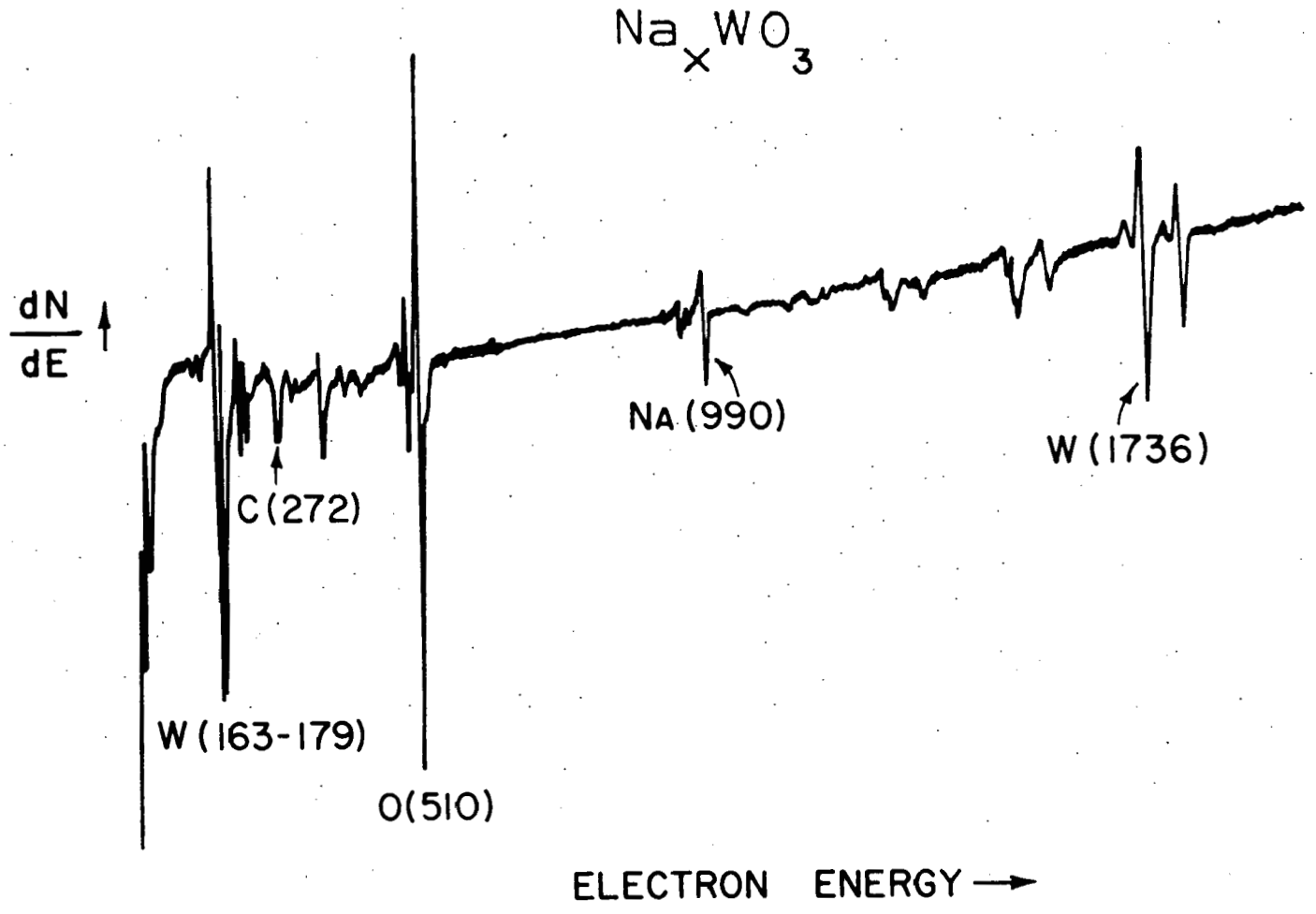

Figure 3.4. Typical Auger spectrum of a clean sodium tungsten bronze surface. The numbers in parentheses are the Auger line energies in electron volts for each particular element

high energies. The low energy peaks lie at 38 eV and 48 eV, and there is a doublet at 163-179 eV. Tungsten has two major high energy peaks, one at 1736 eV and the other 1796 eV. A spectrum for platinum is not shown here, but the two prominent peaks for platinum are at 64 eV and 1967 eV.

For any element, the low energy peaks are very surface sensitive because the escape depth for low energy electrons is only one or two monolayers. The best resolution in a depth profile and the most accurate surface coverage determinations are obtained by monitoring the low energy lines.

CHAPTER 4. RESULTS AND DISCUSSION

Oxygen Tafel Plots

Steady-state current-voltage (i-v) measurements of the oxygen reaction have been performed on several alkali tungsten bronzes, with special emphasis on the sodium tungsten bronze system. All steady-state results are presented in the form of Tafel plots, which were discussed in Chapter 2. The alkali tungsten bronzes studied were hexagonal thalium, rubidium and potassium tungsten bronzes, cubic lithium and sodium tungsten bronzes, tetragonal lithium and sodium tungsten bronzes, and monoclinic sodium tungsten bronze. The monoclinic crystal may be referred to as WO_3 although it has a sodium x-value of 0.02. All measurements were performed in 0.1 N sulfuric acid for valid comparison to the work of other investigators, particularly Bockris and McHardy (18), and to reduce corrosion currents to a minimum. In most figures shown here, a Tafel plot for O_2 reduction on Pt is shown for comparison with the bronzes. A variety of Tafel plots for Pt can be found in the literature because of different procedures of measurement and of different purities of the solution. Most steady-state data on Pt involves a two to five minute wait between data points. Prolonged cathodic polarization for O_2 reduction probably results in the buildup of hydrogen peroxide in the solution, which results in a lowering of the observed potentials (4). Each Tafel plot for the bronzes required two or three days because of a three to four hour wait for steady state to occur at each point. Comparison with Pt becomes difficult because Pt is more sensitive than the

bronzes to the buildup of impurities in the cell during a two day Tafel measurement. Since the cell was rather well sealed, and ultrapure solutions could normally be stored for several weeks in the storage flask, the impurity was probably hydrogen peroxide which was produced during oxygen reduction. The high rest potentials of 1.00 V RHE could not be reproduced after one day of measurements, and after two days of measurements, large deviations in potential occurred at the higher current densities on Pt. The data on Pt is shown in Figure 4.1. The solutions were not pre-electrolyzed, so the slope was less than the normal 100 mV/decade due to traces of impurities remaining in the solution. For all of the data presented here, the potentials are referenced to the normal hydrogen electrode (NHE). In 0.1 N H_2SO_4, the theoretical rest potential of the oxygen reaction is 1.158 V NHE and is -0.072 V NHE for the hydrogen reaction.

Tafel plots have been obtained for O_2 reduction on a large number of pure, platinum doped and platinized sodium tungsten bronze crystals. Several important i-v features of pure bronze and Pt doped bronze crystals have been found which were not reported by earlier investigators. Data for pure cubic Na_xWO_3 are shown in Figure 4.2, along with a typical Tafel plot for platinum. A definite break in the Tafel line for the bronze occurred at 4×10^{-5} A/cm^2, where the potential dropped abruptly towards the hydrogen reaction. This current density appears to be the limiting rate of oxygen reduction on a pure sodium tungsten bronze surface. In the lower current region, the Tafel slope was 110 mV/decade and the exchange current density was approximately 10^{-14} A/cm^2. At the high

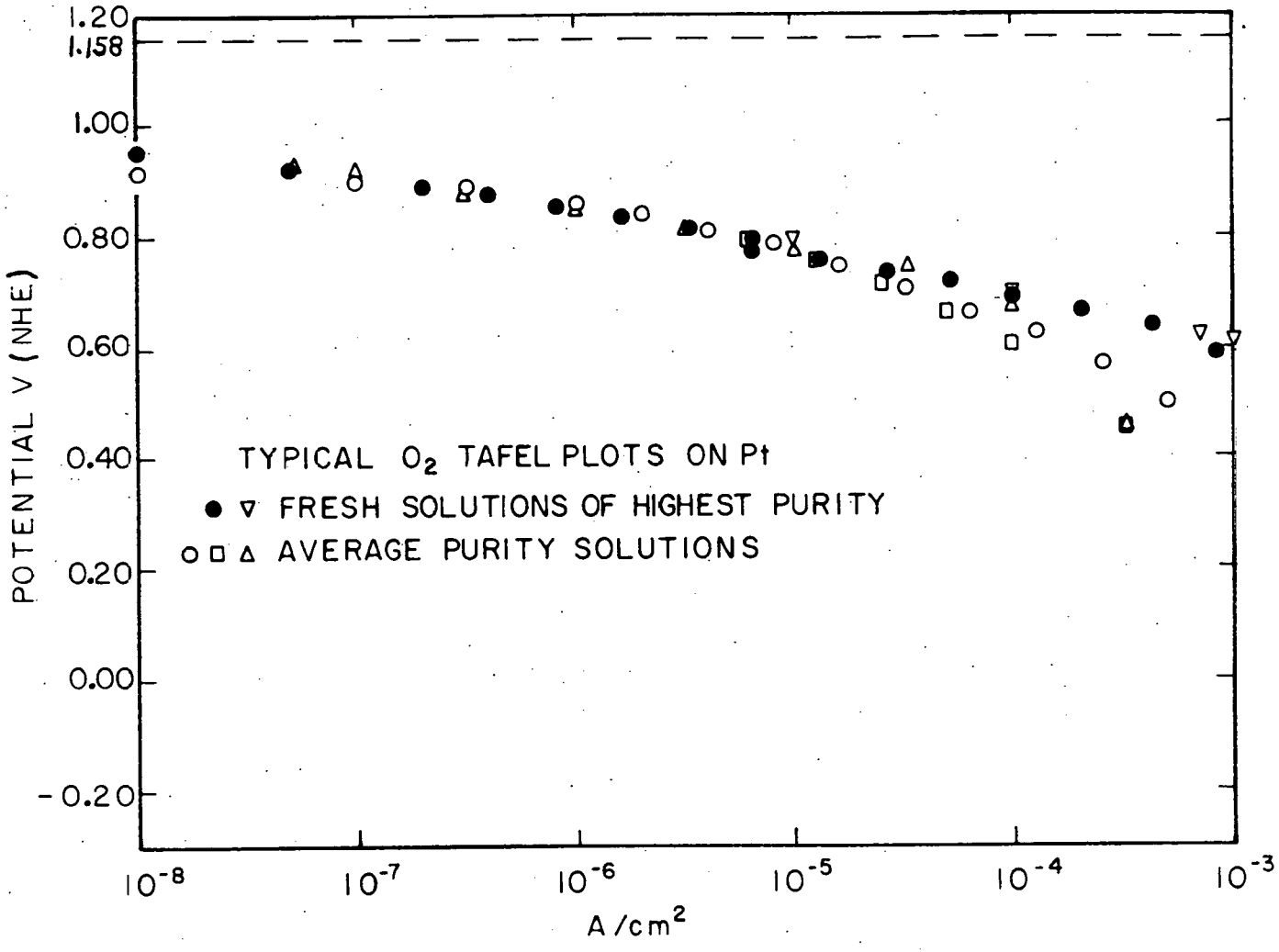

Figure 4.1. Oxygen Tafel plots taken on a Pt electrode under the same experimental conditions as used for testing the bronze crystals

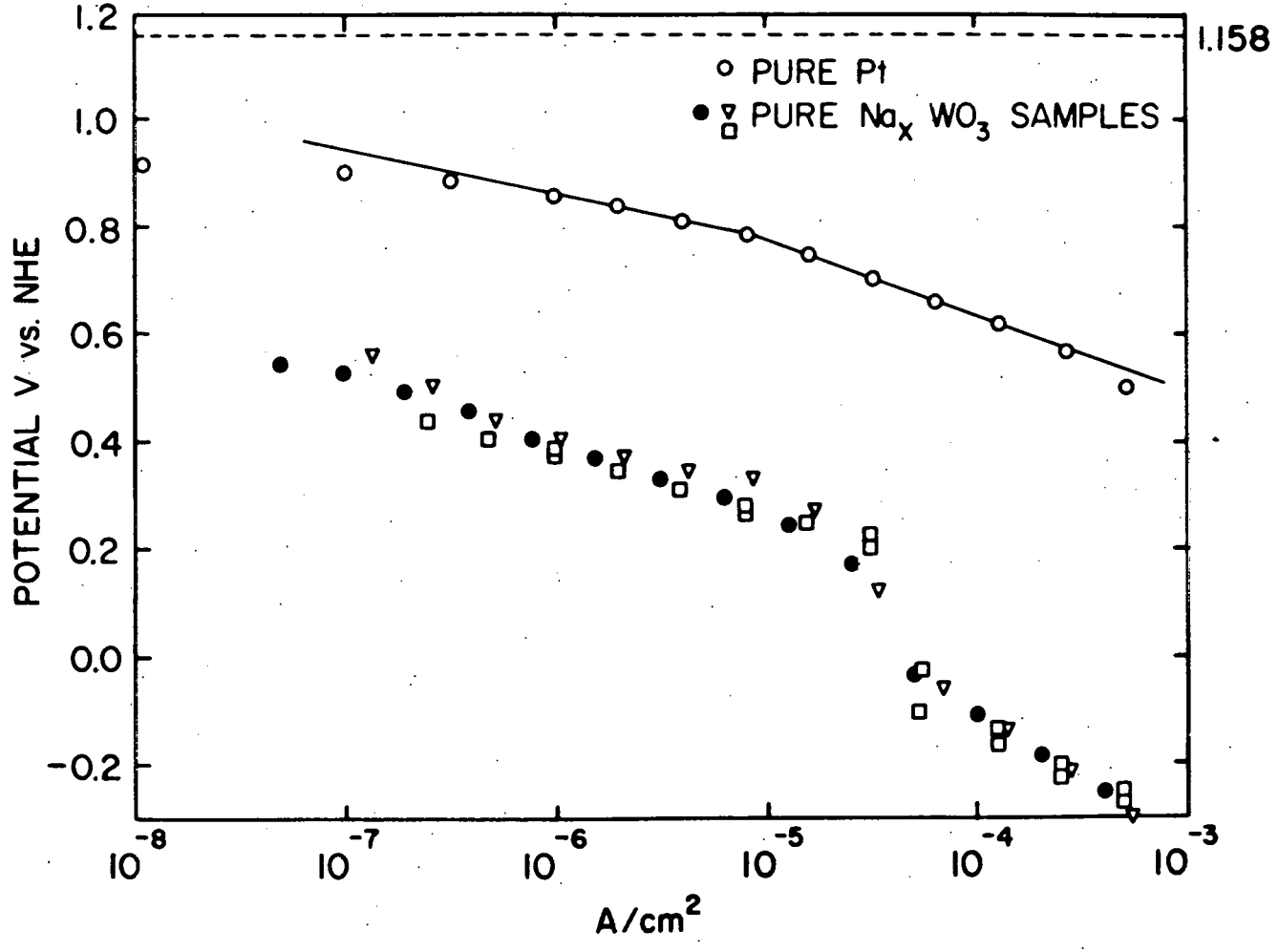

Figure 4.2. Oxygen Tafel plots for $N_{0.7}WO_3$ crystals: o polished, ∇ cleaved, and □ polished and etched in NaOH. Anodization of a crystal had no noticeable effect on its Tafel plot

current densities, the slope is 200 mV/decade, in agreement with the results by Randin (19). Based on the extremely high overvoltages in this region ($i > 4 \times 10^{-5}$ A/cm^2), Randin concluded that the sodium tungsten bronze does not support O_2 reduction. However, by viewing the results at the lower current densities, it is obvious that pure sodium tungsten bronze does exhibit some catalytic activity for oxygen reduction. Tafel behavior to current densities below 10^{-7} A/cm^2 indicated a very small corrosion rate on the bronze surface. Extended anodization of the crystal surface at 1 mA/cm^2, until the potential reached 9 volts, did not greatly affect the catalytic activity. A slight increase in catalytic activity was observed (higher potentials) in the low current region, but the break in the Tafel line occurred at lower current densities, so the effect was not due to a simple increase in surface area. There was no observable difference between the Tafel plots of polished crystals and cleaved crystals.

Samples of $Na_{0.7}WO_3$ doped with 800 ppm Pt also have a limiting current density of 4×10^{-5} A/cm^2, as shown in Figure 4.3. A second threshold was observed on these crystals at 10^{-6} A/cm^2 and we attribute this effect to the presence of the Pt incorporated into the sample during crystal growth. Prolonged anodization of these crystals (1 mA/cm^2 until V reached 9 volts) definitely improved their catalytic activity at the low current densities. After anodization there was an increase in potential at the low current densities and a shift in the second threshold from 1×10^{-6} A/cm^2 to 4×10^{-6} A/cm^2. The 800 ppm Pt had no effect at the higher current densities. Platinum doped samples, which did not

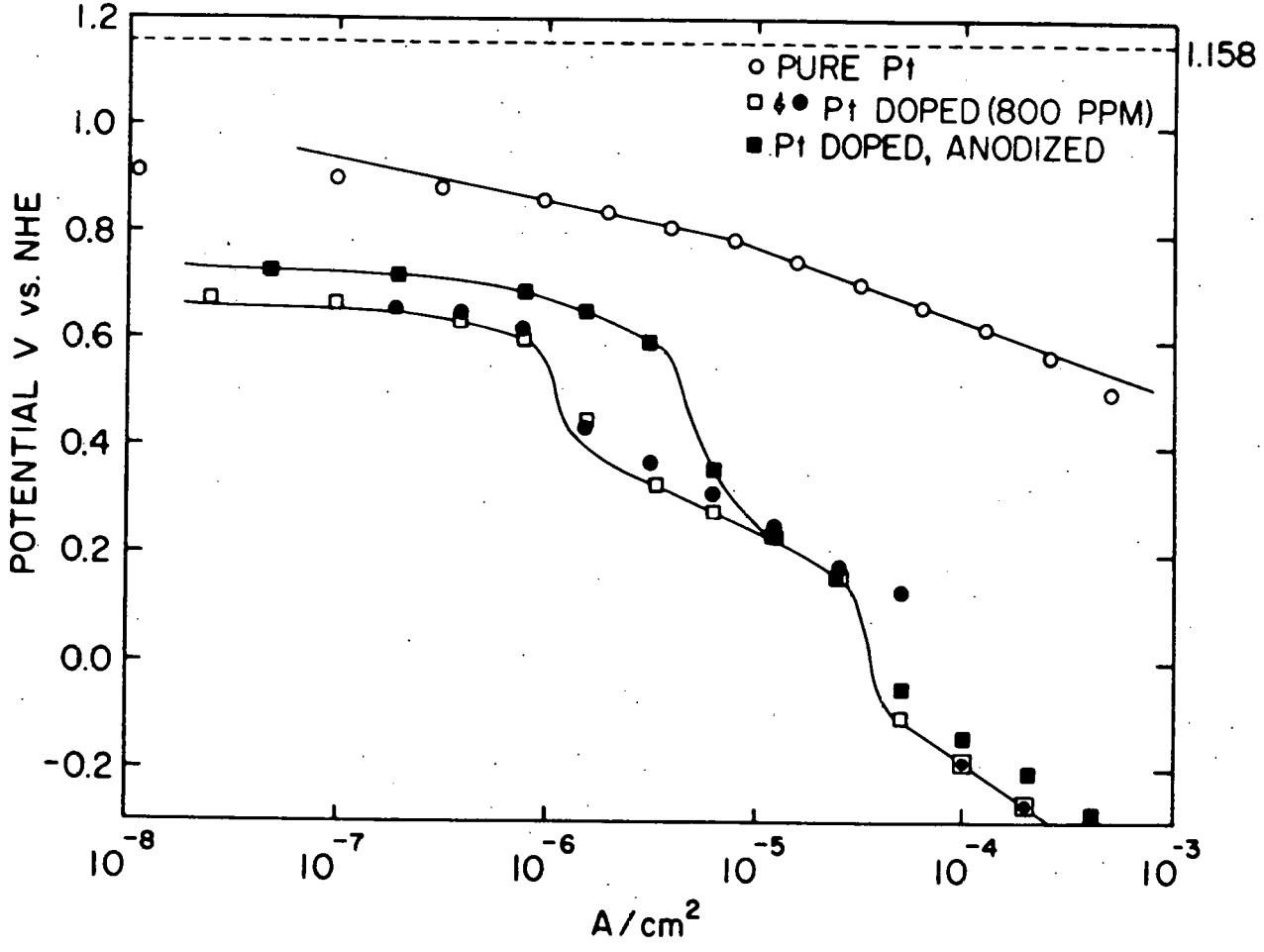

Figure 4.3. Oxygen Tafel plots for crystals doped with 800 ppm Pt, and for a doped crystal after anodization to 9 V. The Pt doping improves the catalytic activity only at very low current densities. Anodization improves the catalytic activity, but the reason for this is unknown

receive the isopropyl vapor-phase degreasing and the cyclic voltage scans before the measurements, did not exhibit the break in the Tafel plot at 10^{-6} A/cm^2.

The effect of Pt pre-electrolysis on the performance of a Pt doped crystal is shown in Figure 4.4. Extensive Pt pre-electrolysis of the solution tended to deposit traces of Pt on the samples, especially on preanodized samples. Both curves shown in Figure 4.4 are for the same preanodized 800 ppm Pt doped bronze crystal. After Pt pre-electrolysis, the potentials were higher at all current densities. Platinum concentrations of 800 ppm cannot be detected by our Auger spectroscopy system, but after Pt pre-electrolysis Pt was detected on the surface of this sample on the order of one percent Pt coverage. These results are given in the section on Auger analysis. An undoped crystal was affected in a manner similar to the doped crystals; the potentials were higher at all current densities, as shown in Figure 4.5, but not as high as for the Pt doped crystals. Evidently, more platinum is deposited from the solution on a doped crystal than on an undoped crystal.

A major difference exists between a Pt contaminated pure bronze and an 800 ppm Pt doped bronze. The curves in Figure 4.3 and 4.5 are strikingly different, at both the low and high current densities. Platinum contamination of a pure bronze by Pt pre-electrolysis increased the catalytic activity at all current densities, but produced no threshold at 10^{-6} A/cm^2. Doping the bronze with 800 ppm Pt had no effect on the potentials at the high current densities. These results indicate that the platinum may be incorporated in different forms on the surface by the

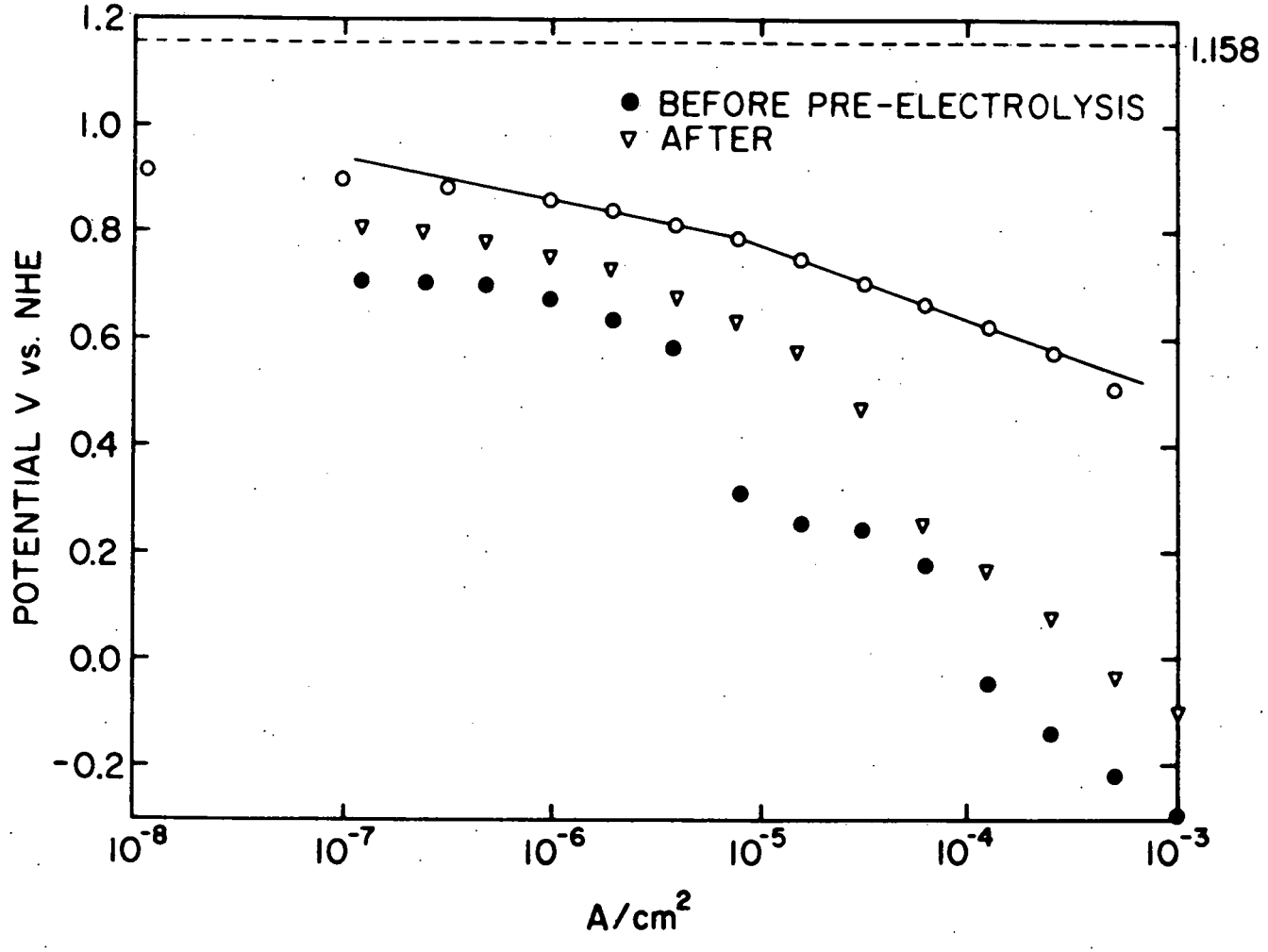

Figure 4.4. Oxygen Tafel plots for an anodized 800 ppm Pt doped crystal (371B#3) taken in fresh and Pt pre-electrolyzed solutions. Platinum plated out of the pre-electrolyzed solution onto the bronze surface, improving the bronze's catalytic activity

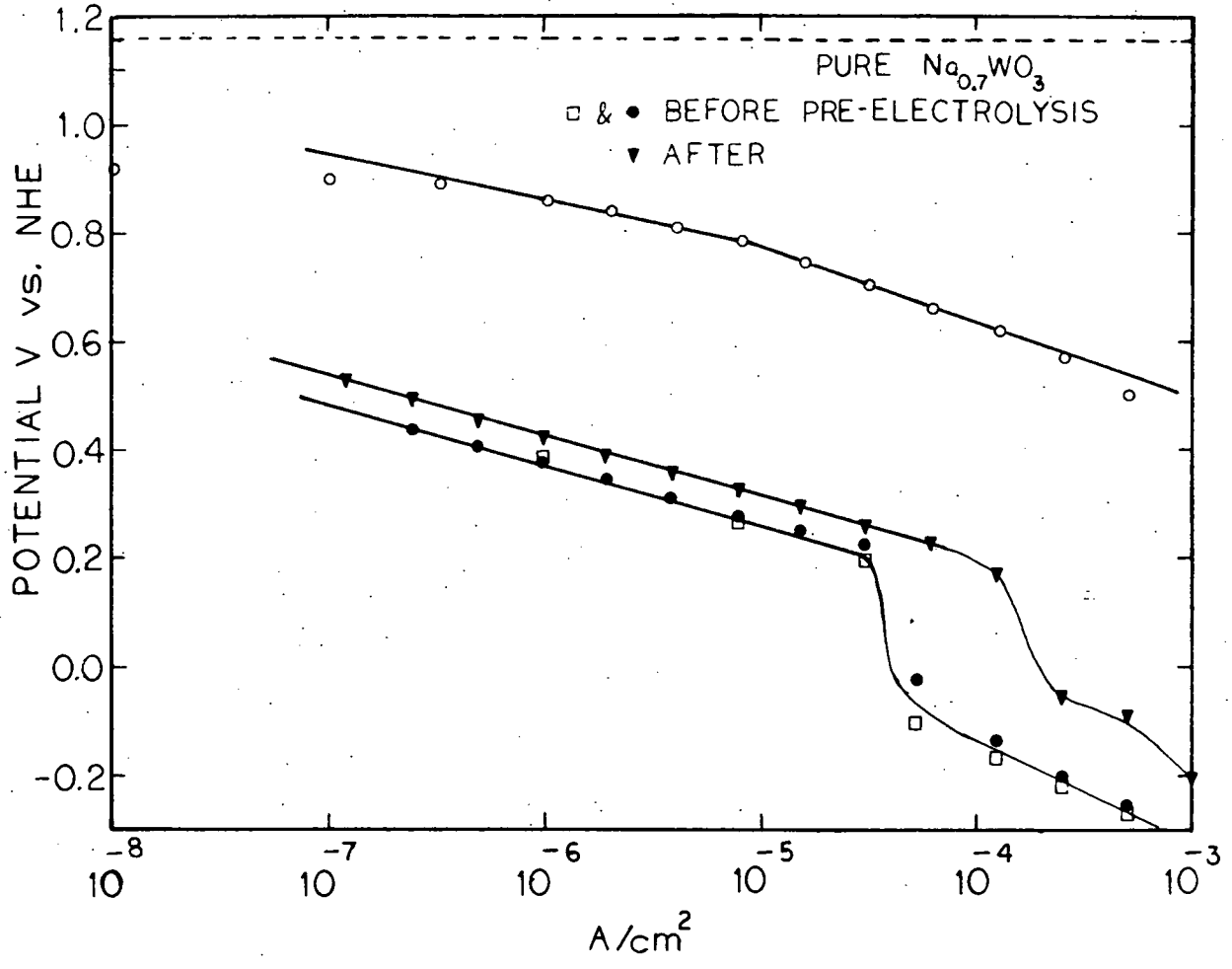

Figure 4.5. Oxygen Tafel plots on a pure bronze taken in fresh and Pt pre-electrolyzed solutions. Platinum pre-electrolysis contaminated the crystal with Pt, increasing its catalytic activity

two methods. Platinum pre-electrolysis was done with a large (20 cm^2) shiny Pt foil anode and a gold cathode using 20 mA of current for 24 hours, then with 5 mA continuous pre-electrolysis during the measurements.

Tafel plots are shown in Figure 4.6 for three types of sodium tungsten bronze crystals: a pure bronze, an 800 ppm Pt doped bronze, and the same pure bronze after it was used in solution which was pretreated by cycling a large Pt electrode from 0.0 V to 1.5 V NHE at 100 mV/sec for 3.5 hours. Later analysis by Auger spectroscopy revealed a Pt coverage of approximately 3% on the crystal surface. None of the samples were anodized and the Auger analysis showed that the sodium content on the surface was equal to the bulk value. For current densities above 10^{-6} A/cm^2, the Pt doped crystal behaved like a pure bronze; but at low current densities, approaching the rest potential, the Pt doped crystal behaved like the Pt contaminated crystal. The Pt doped crystal has less Pt on the surface than the Pt contaminated crystal by a factor of 40, yet it still has the same rest potential. Thus, the Pt doping of the bronze produced a definite electrocatalytic effect for O_2 reduction, although the effect was rather small. Experiments were then performed to determine whether or not the electrocatalytic activity was directly proportional to the Pt coverage fraction θ on the crystal surface.

Sodium tungsten bronze crystals, plated with varying amounts of Pt, were tested for O_2 reduction and later analyzed with Auger Spectroscopy to measure the Pt coverages. Platinum was deposited on several crystals by each of the three techniques discussed in Chapter 3. Only crystals plated from chloroplatinic acid had to be polished and anodized before

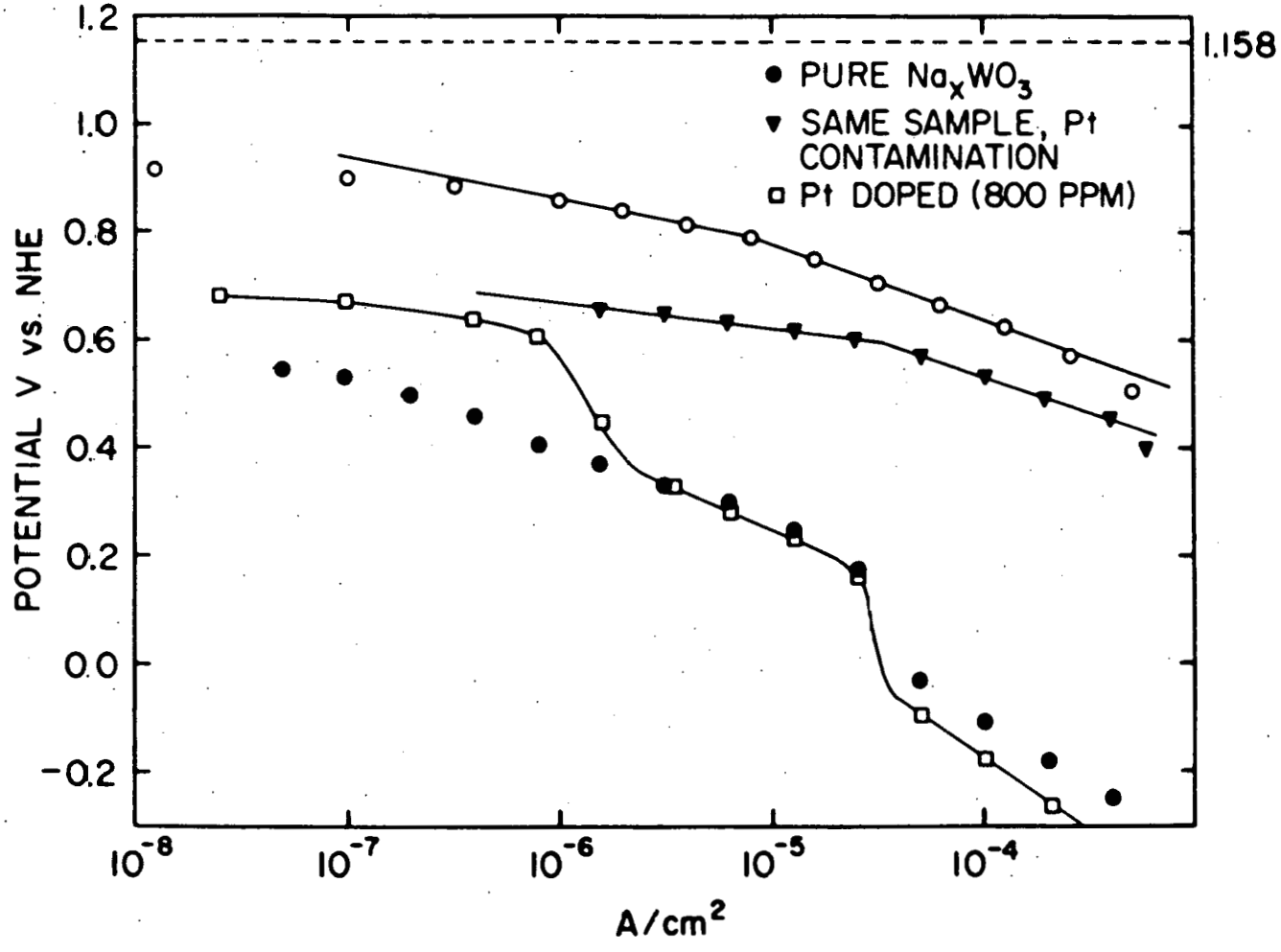

Figure 4.6. Comparison of a pure bronze (376A#10), a Pt doped bronze, and the same pure bronze with a 3% Pt coverage. The Pt contamination of the pure crystal was due to the presence and usage of a large Pt foil in the cell

plating. However, anodizing the crystals seemed to accelerate the Pt deposition process when the in situ plating procedures were used. The three Pt deposition methods will be referred to as methods a, b, and c. Method a consisted of plating from dilute chloroplatinic acid, while methods b and c were variations on an in situ process of slow dissolution of a large Pt foil. In method b, the Pt foil was used as a counter electrode to cycle the potential of the bronze crystal from -0.25 V to 1.25 V at 100 mV/sec. Method c consisted of cycling the Pt foil itself from 0.00 V to 1.5 V at 100 mV/sec for several hours, and then using the bronze sample in the same solution.

Tafel plots for the Pt plated crystals are shown in Figures 4.7 to 4.10. The data for two of the crystals were shown in Figures 4.4 and 4.6. A true steady-state condition was allowed to occur for all the data presented in these graphs. This condition is important, since considerably different potentials are obtained if fast measurements are made. A typical example of this difference is shown in the top graph of Figure 4.8. A stable steady-state condition could be obtained on the platinized bronzes because they were not as sensitive as Pt to the buildup of H_2O_2 in the cell during the course of a two day Tafel measurement. This observation is supported by the results of Randin (19), who reported good catalytic activity of undoped bronzes for the reduction of H_2O_2.

Exchange currents could not be determined from the Tafel plots because the low Tafel slopes and high overvoltages on many of the samples made extrapolation to zero overvoltage a very inaccurate procedure. The current density at 0.5 V was arbitrarily picked as a measure of the

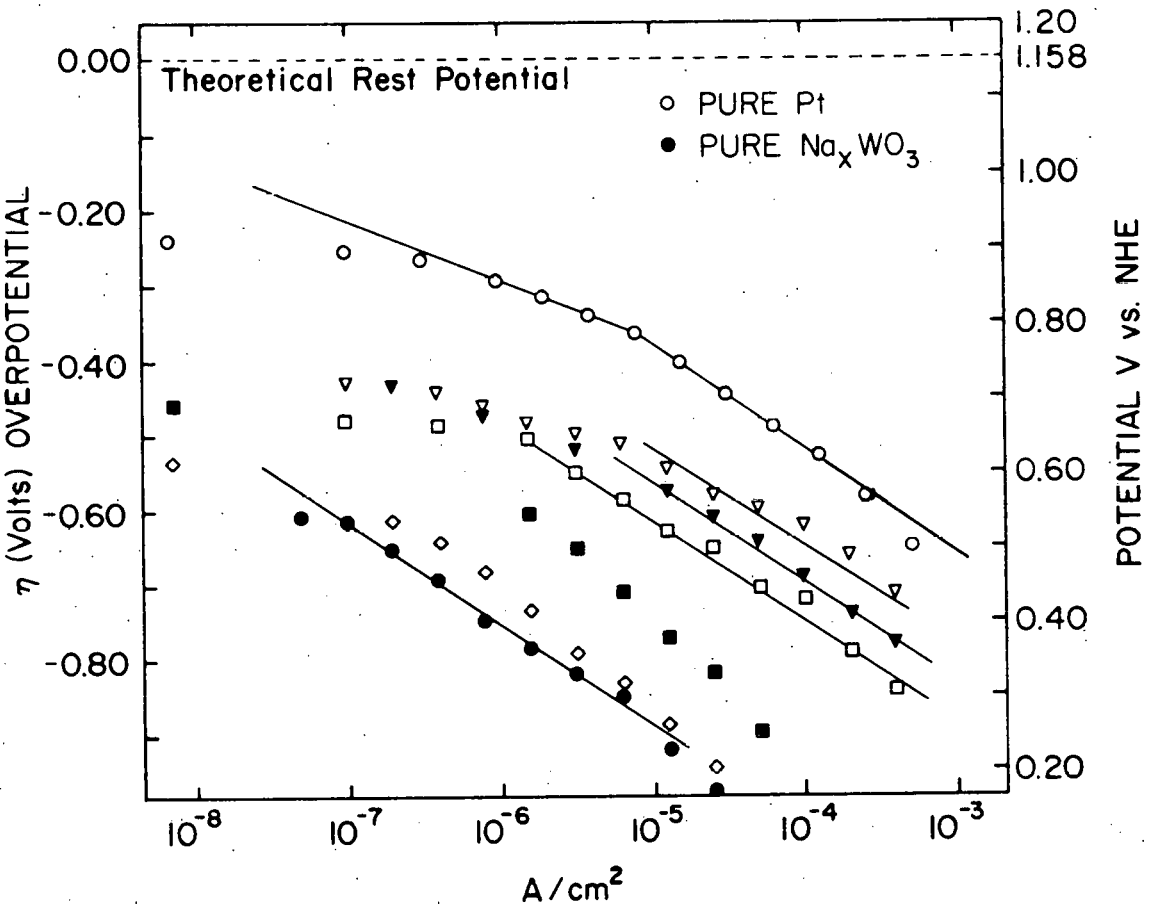

Figure 4.7. Oxygen Tafel plots for crystals plated at 0.120 V in chloroplatinic acid. The Pt coverages are given in Table 4.1. ▽ 376A#2, □ 376A#3, ▼ 376A#4, ■ 376A#1, ◇ 376A#14

Figure 4.8. The top graph illustrates the difference between quick measurements and true steady-state measurements that allowed at least 3 hours per point.
The middle graph presents successive O_2 Tafel plots for a crystal plated by a technique that gave very good activity for O_2 reduction.
The bottom graph presents two oxygen Tafel plots for a crystal that was anodized before plating, as usual, and then anodized again after the first Tafel measurements. Platinum was detected by cyclic voltammetry after the first Tafel measurements, but none was found after the second anodization, either by cyclic voltammetry or by the SEM. The Auger analysis revealed a Pt coverage fraction of only 0.007, yet the catalytic activity is good

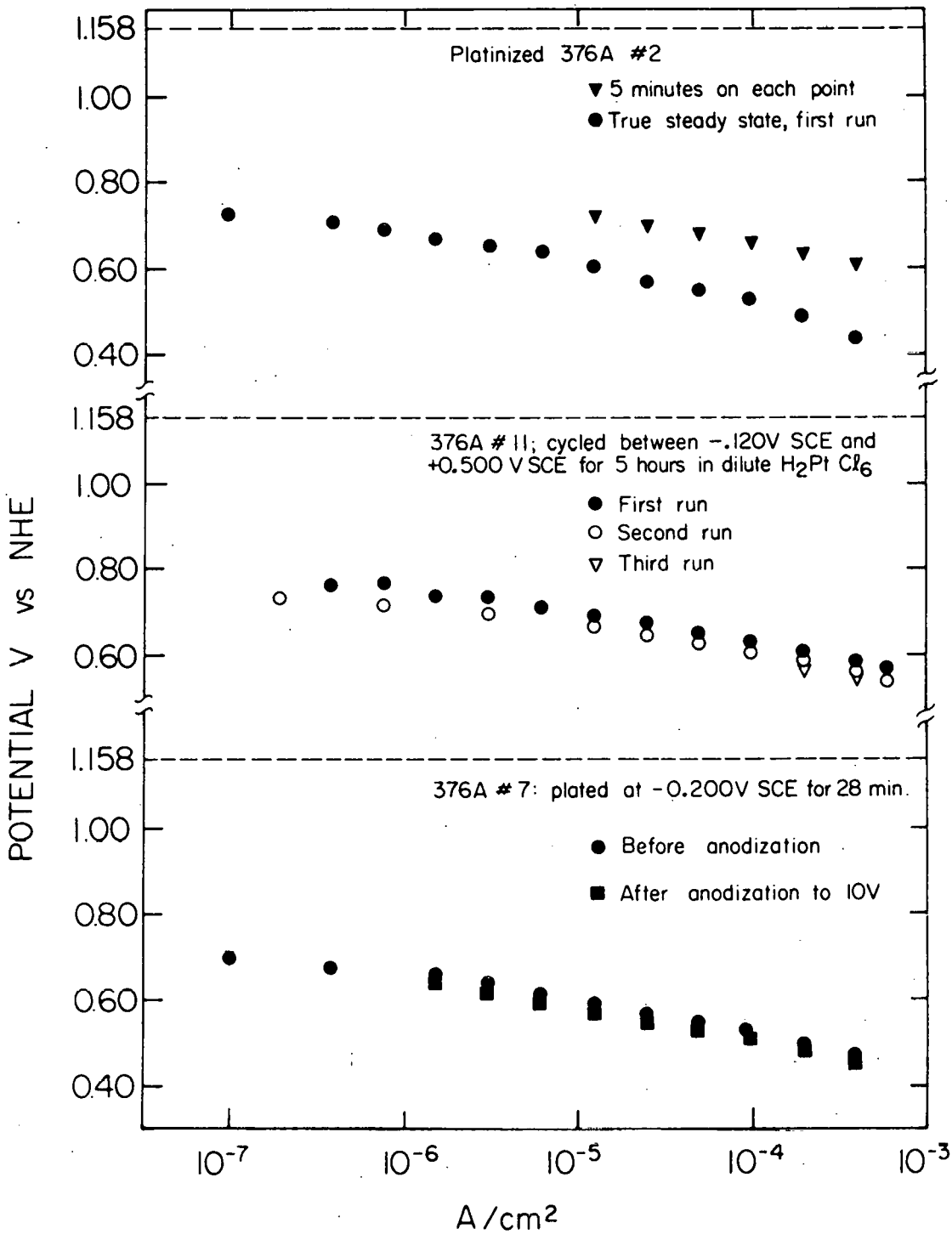
Platinized 376A #2
▼ 5 minutes on each point
● True steady state, first run
376A # 11; cycled between −.120V SCE and +0.500 V SCE for 5 hours in dilute $H_2Pt\,Cl_6$
● First run
○ Second run
▽ Third run
376A # 7: plated at −0.200V SCE for 28 min.
● Before anodization
■ After anodization to 10V
1.158
1.00
0.80
0.60
0.40
POTENTIAL V vs NHE
10^{-7}
10^{-6}
10^{-5}
10^{-4}
10^{-3}
A/cm²

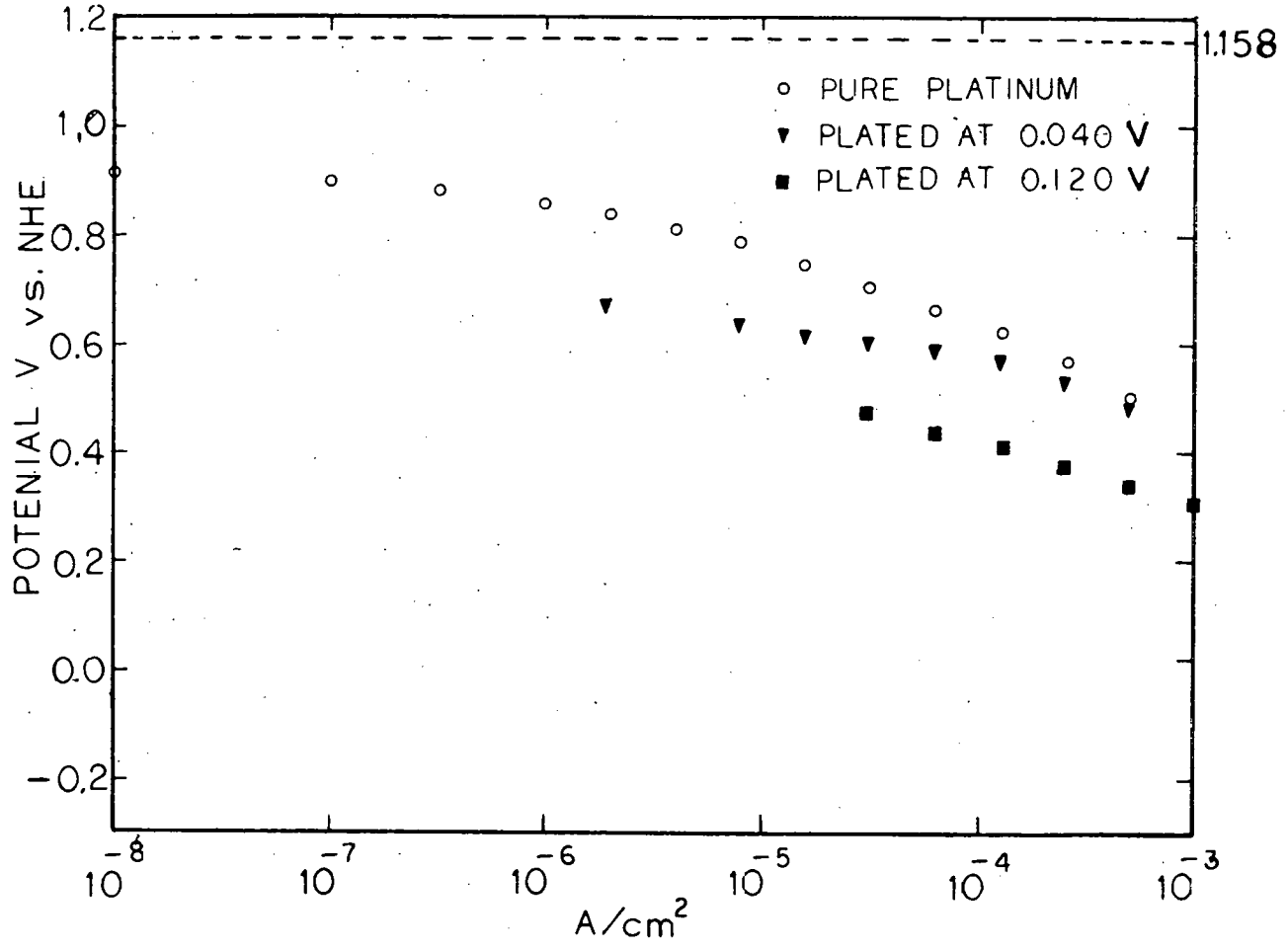

Figure 4.9. Oxygen Tafel plots for pure Pt and two bronze crystals plated from chloroplatinic acid (▼ 376B#2, ■ 376B#1). The bronze sample with the lower catalytic activity (376B#1) had slightly more Pt on its surface. Plating at 0.040 V gives higher catalytic activities with less Pt

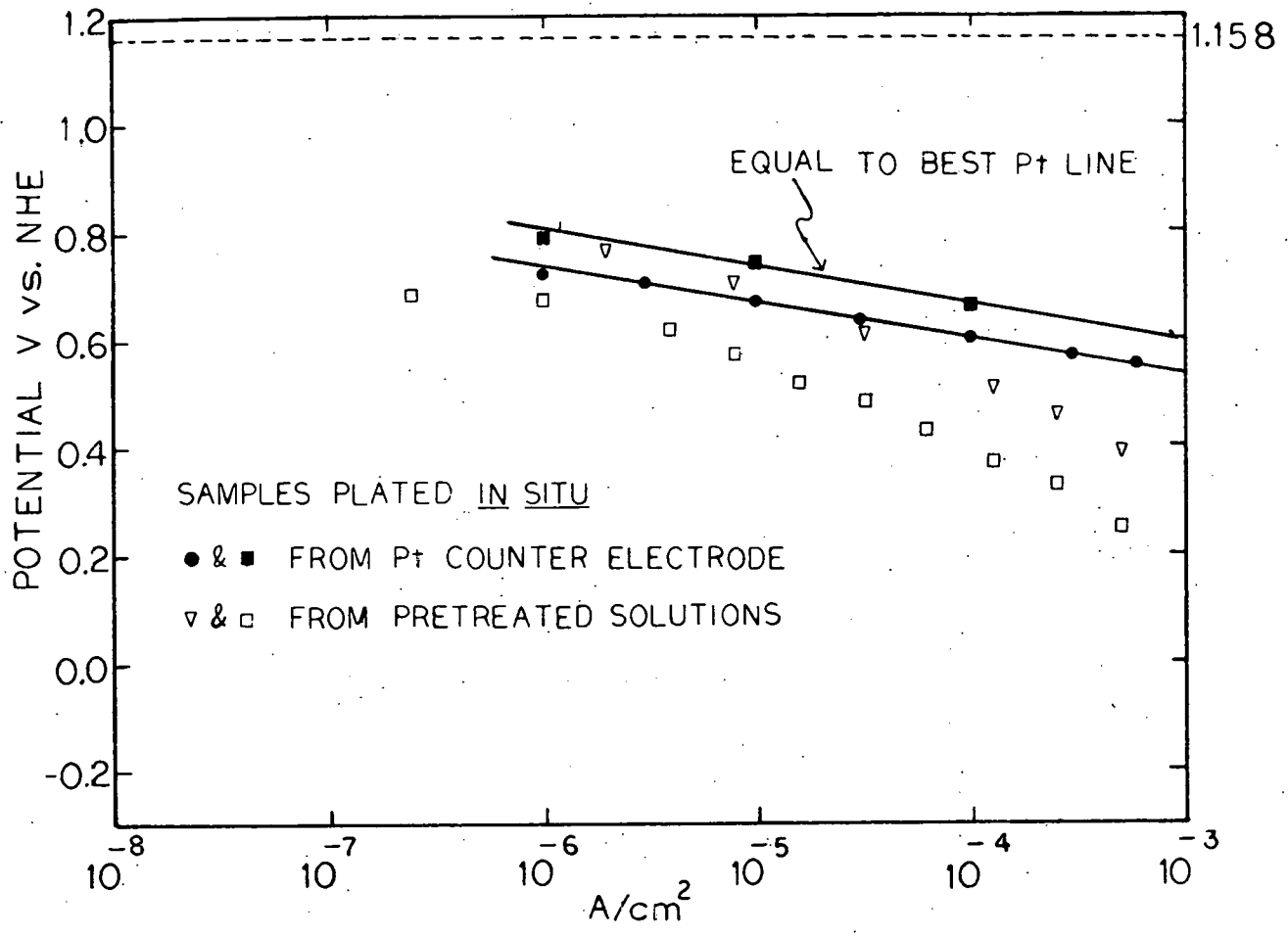

Figure 4.10. Oxygen Tafel plots for samples plated in situ by dissolving Pt from a Pt foil. The samples were: ■ 371B#5, ● 365C#2, ▽ 380A#5, □ 371B#8. The two crystals plated from the counter electrode had the lowest Tafel slopes and the highest catalytic activities of all the samples

catalytic activity of the crystals. For most crystals, the Tafel lines passed through 0.5 V, but short extrapolations were necessary for samples with a high catalytic activity. A list of the platinized bronze crystals, with the current density at 0.5 V, and the Pt coverage fraction θ for each crystal, is given in Table 4.1. The information in this table can be best examined by making a log-log plot of catalytic activity (i at 0.5 V) versus the Pt coverage. This graph is presented in Figure 4.11. Although there is considerable scatter in the intermediate points, the points at both extremes suggest a straight line fit to the data. A line drawn through the points which fits the extreme points and passes through the cluster of points has a slope of 1.5. A least squares fit for a straight line gives a lower slope of 1.2, due to the large amount of scatter in the points for intermediate Pt coverages. The scatter causes the least squares fit line to deviate substantially from the data points at both extremes. A slope of 1.0 on the log-log plot would imply that the catalytic activity is directly proportional to the Pt coverage θ on the crystal surface.

Bockris and McHardy reported a synergistic effect of Pt with the bronze (18), with the catalytic activity proportional to the cube of the Pt coverage. Bockris and McHardy did not measure the Pt coverages, but assumed that the surface Pt concentrations were equal to the bulk concentrations of Pt in the crystals. Other results, reported here (see Figure 4.6 and the Auger analysis results), indicated that this assumption was invalid, and that Bockris and McHardy's samples probably had higher Pt coverages than they thought. The Tafel results reported here show the

Table 4.1. Pt coverages and catalytic activities of the Pt plated samples.

Sample	Pt/W ratio[a]	θ[b]	i(μA) at 0.5 V
376A#4	0.0025	0.00085	0.47
376A#1	0.01	0.0033	3.1
376B#1	0.16	0.050	17
371B#3	0.01	0.0033	25
371B#8	0.013	0.0043	25
376A#3	0.03	0.01	25
376A#4	0.14	0.045	50
376A#7	0.02	0.0067	120
380A#3	0.05	0.016	150
376A#10	0.08	0.026	150
376A#2	0.22	0.068	150
376B#2	0.16	0.050	370
376A#11	0.25	0.077	1,400
365C#2	0.67	0.18	2,500
371B#5	2.20	0.42	10,000
Pt	-	1.00	10,000

[a] Pt/W ratio: determined from Auger analysis, except the first two, which were estimated from the plating times.

[b] $\theta = x/(3 + x)$, where x = Pt/W ratio. The number 3 arises from the approximation of a WO_2 surface stoichiometry, due to oxygen desorption during the Auger analysis.

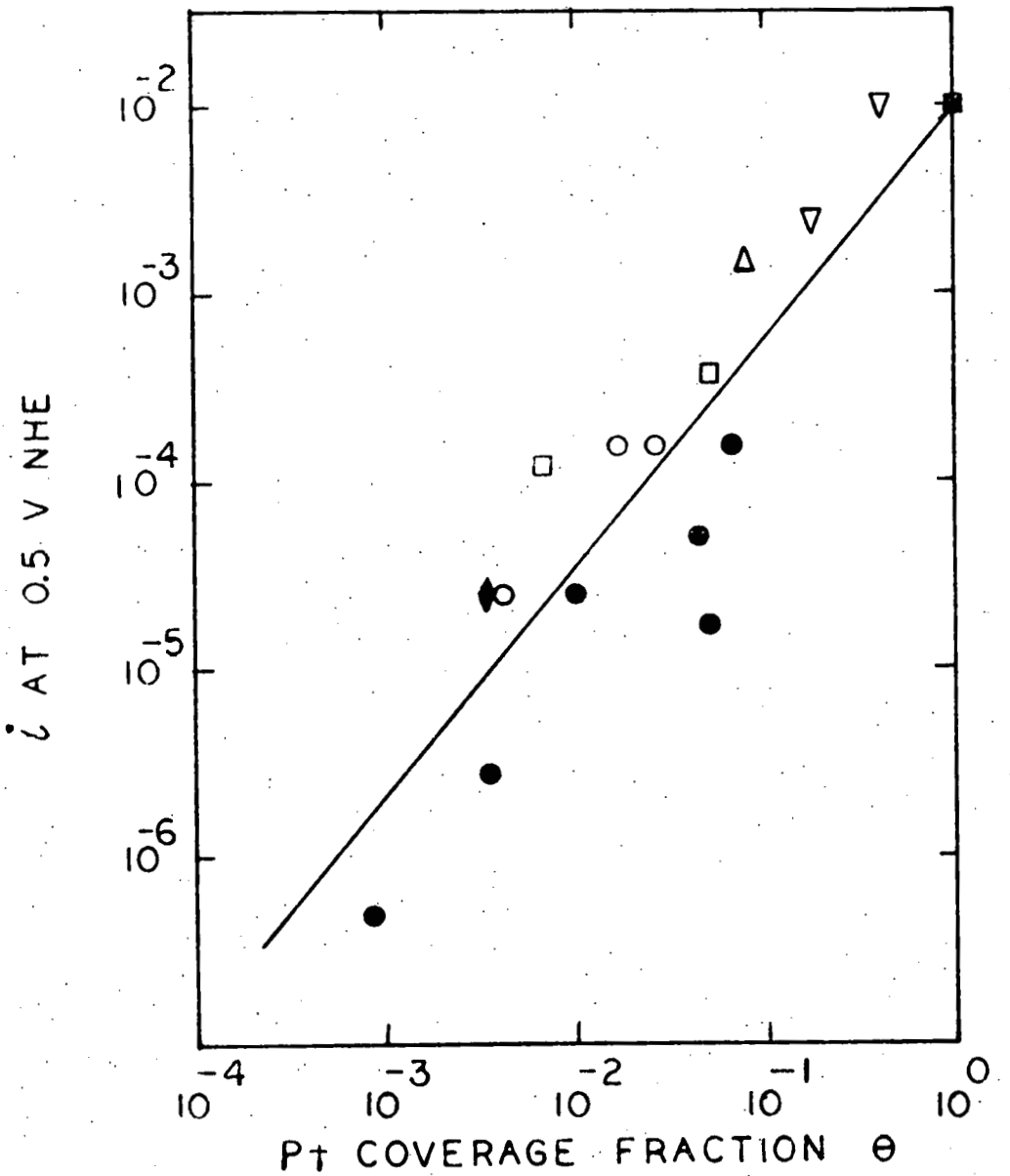

Figure 4.11. Log-log plot of catalytic activity versus Pt coverage. The slope of the least squares fit line is 1.2, so the catalytic activity is directly proportional to the Pt coverage. ■ Pure Pt, ● Pt plated at 0.120 V (from chloroplatinic acid), □ Pt plated at 0.040 V, ▽ plated from a Pt counter electrode (method b), ○ plated by dissolving Pt from a Pt foil (method c), △ cycled from 0.120 V to 0.50 V in chloroplatinic acid, ◆ contaminated by Pt pre-electrolysis

catalytic activity is proportional to the Pt coverage to the 1.5 power or less. Due to the experimental error in measuring θ, and the wide scatter in the catalytic activities, no synergistic effect can be claimed for O_2 reduction by a Pt-bronze system. However, the wide variation of Pt coverages, on samples with the same catalytic activity, may be a significant result in itself. These variations in the measured Pt coverages were much greater than the experimental error in the Auger analysis. Samples with more than an order of magnitude difference in Pt coverage have the same catalytic activity. The errors in measuring the Pt coverage by Auger analysis were much less than an order of magnitude, and were usually 50% or less. Several samples with about the same measured Pt coverage had one to two orders of magnitude difference in the measured catalytic activity.

These differences in catalytic activity for a given Pt coverage, and vice versa, imply that the Pt is present in different physical forms on different crystals, one form being more catalytically active than the other form. The symbols used for the points in Figure 4.11 indicate the procedure by which Pt was deposited on the crystal surface. Several trends are noticeable. Samples represented by points on the right side and beneath the line were plated in chloroplatinic acid solutions at 0.120 V NHE. These samples have a lower catalytic activity per unit amount of Pt than do the samples above the least squares fit line. Scanning electron microscope photographs revealed the presence of Pt crystallites on the bronze surface. Tafel plots for five of these samples are shown in Figure 4.7. Most of the other points on the graph

in Figure 4.11, to the left and above the line, either had no Pt particles visible to the SEM, or the Auger depth analysis indicated that any Pt particles on these samples would have been too small to be seen by the SEM. Two crystals plated at 0.040 V in chloroplatinic acid were exceptions in this case. SEM photographs showed that Pt particles were present on crystals plated in this manner. However, one of these crystals (sample 376A#7) was reanodized, a process which was shown by the cyclic voltammetry curves, and later by the SEM, to have removed the Pt particles without changing the catalytic activity. The catalytic activity can be evaluated from the Tafel plots in the bottom graph of Figure 4.8. Immediately after plating, sample 376A#7 exhibited high catalytic activity, and a 5 to 10 percent Pt coverage was indicated by the cyclic voltammetry curves. After reanodization, the Tafel plot was essentially unchanged, but no Pt was detected by the cyclic voltammetry or the SEM, and the Auger analysis gave a Pt coverage of only 0.7 percent. These results indicate that the catalytic activity may not be due to the Pt particles that are highly visible on the SEM, but that the activity is due to a different form of Pt on the crystal surface.

More evidence for the existence of two forms of Pt on the bronze surface was obtained in a careful study of two $Na_{0.6}WO_3$ crystals. Crystal 376B#1 was plated at 0.120 V for 3.5 hours, and crystal 376B#2 was plated at 0.040 V for 90 minutes; the other plating conditions were exactly the same. Both crystals were anodized to 6.0 V before plating. Later, the Auger analysis showed equal Pt coverages on the two crystals. Scanning electron microscopy photographs revealed large (3,000 Å dia.)

Pt particles on 376B#1, with the Pt particles covering about 10 percent of the crystal surface. The Pt particles were roughly spherical in shape, so the total area of the Pt was perhaps 30 percent of the geometric surface area. Smaller particles (1,200 Å dia.) were seen on sample 376B#2. The two samples were then characterized by three electrochemical measurements: Tafel measurements for both the hydrogen and oxygen reactions, and cyclic voltammetry (CV) measurements.

The CV curves for sample 376B#1 showed a Pt coverage of 20 to 30 percent, while only a 5 to 10 percent Pt coverage was indicated on sample 376B#2 (see the section on cyclic voltammetry). Current-voltage measurements for the hydrogen reaction were taken in the linear, or low overvoltage region, and these results are shown in Figure 4.12. The exchange currents were found from the slopes of lines by using Equation 2.12. The exchange currents were not expected to be directly proportional to the amount of Pt on the crystal, because a synergistic effect of the Pt-bronze system has been reported for the hydrogen reaction (54). The exchange currents were higher than a direct proportionality to the Pt coverage would predict; however, the H_2 measurements helped determine the relative amounts of Pt on the two crystals. The exchange currents are in rough agreement with the amount of Pt found by the CV curves. The electrochemical measurements of the Pt coverages differ from the Auger and SEM results, but there is a good reason why this could be so. The electrochemical methods measure the average Pt coverage over the entire crystal surface, while the SEM and Auger methods sample only a tiny spot on the surface. In fact, both the Auger and SEM detected no Pt in

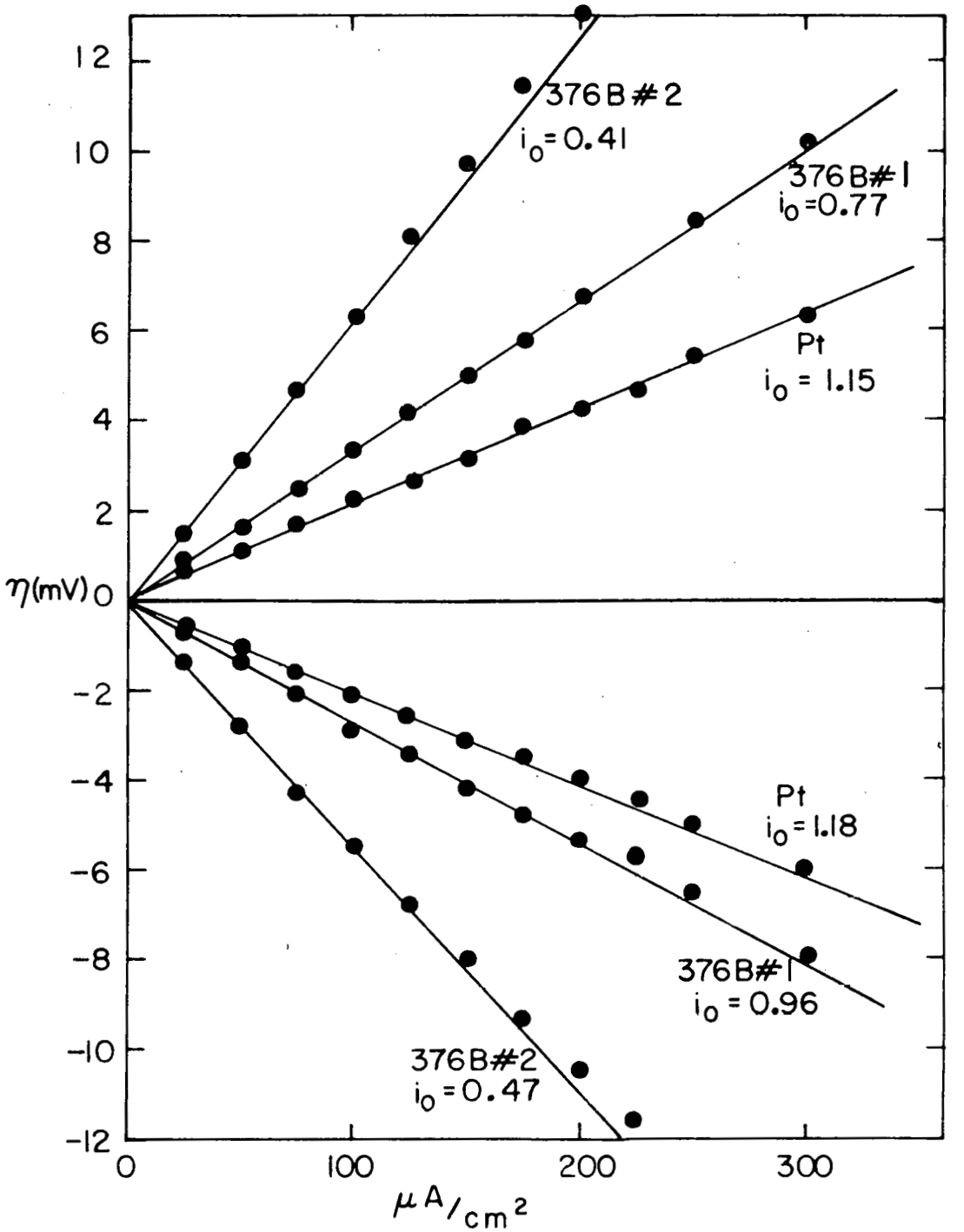

Figure 4.12. Current-potential data for the hydrogen reaction on Pt plated bronzes. Data were taken in the low overpotential region and is plotted on a linear scale. The exchange currents are twice as large as a direct proportionality to Pt coverage would predict

several spots on sample 376B#2. So in fact, the electrochemical methods (CV and H_2 Tafel plots) may give the better measure of Pt on the crystals. Oxygen Tafel plots were then obtained for these two crystals, and a large difference in their catalytic activity for O_2 reduction was found, but in reverse order to the amount of Pt on each sample. Oxygen Tafel plots for these two crystals are shown in Figure 4.9. The current densities at 0.5 V were 17 $\mu A/cm^2$ and 370 $\mu A/cm^2$ for samples 376B#1 and 376B#2 respectively. The results of all measurements are summarized in Table 4.2.

Table 4.2. Comparison of samples 376B#1 and 376B#2.

Auger analysis:	equal platinum coverages
Cyclic voltammetry:	1/4 PtO ratio
H_2 measurements:	1/2 i_o ratio
O_2 measurements:	22/1 O_2 catalytic ratio

The difference in the oxygen catalytic activity of the two samples cannot be explained simply by the size difference of the Pt particles on the surface. These results may be explained by the presence of two forms of Pt on the crystal surface: the larger Pt crystallites and another, more active, form of Pt on the surface. Both samples had roughly equal amounts of Pt present in the form of Pt crystallites, but sample 376B#2 must have had both forms of Pt on its surface, while sample 376B#1 had only the Pt crystallites.

The existence of a different form of Pt, on the surface of a sodium tungsten bronze, is supported by the results of Fishman et al. (17) who

platinized some bronze crystals by using a Pt counter electrode to cycle the potential of the bronze crystal in an acid solution. Their crystals were assumed to be platinized because the crystals were activated as catalysts for O_2 reduction. Fast potential scans (CV measurements) on the crystals failed to reveal the presence of Pt, so Fishman et al. concluded that the Pt was incorporated in the bronze in a form distinct from the bulk metal state. Of the crystals represented in Figure 4.11, the ones with the highest Pt coverages and the highest catalytic activities were platinized by the method of Fishman et al. The Tafel plots for these two crystals are shown in Figure 4.10.

There would seem to be only two possibilities for a distinctly different form of Pt on the bronze surface: small clusters of Pt atoms, or a chemical compound involving the Pt atoms. The existence of small clusters of Pt atoms seems unlikely, due to the method of Pt deposition. All of the larger Pt particles on a given crystal are of a fairly uniform size, a common occurrence in the deposition of metals by electrochemical plating. Small clusters of the metal, initiated during the plating process, grow continuously larger until the plating potential is removed. If instead of Pt clusters, a new chemical compound is formed on the bronze surface, this compound would very likely be a platinum tungsten bronze (Pt_yWO_3). Formation of a platinum tungsten bronze would result in the Pt donating the $6s^1$ electron to the bronze conduction band, similar to the sodium $3s^1$ electron in Na_xWO_3. The d-electrons would remain localized in the bronze, as they are in metallic platinum. The band structure of cubic $PtWO_3$ has been calculated, and a large peak in

the density of states occurs near the Fermi level (55). This peak is due to the highly localized Pt d-electrons. The existence of the compound Pt_yWO_3 on the surface of cubic Na_xWO_3 has not been verified by the experimental results given here, but instead, the formation of platinum tungsten bronze on the surface of cubic Na_xWO_3 is postulated as a possible explanation of these results. To our knowledge, no electrochemical measurements have been performed on Pt_yWO_3. The results of O_2 measurements on Pt_yWO_3 may help verify or deny the existence of Pt_yWO_3 as the highly active form of Pt on the sodium tungsten bronze surface.

No mechanistic studies were done for the oxygen reaction on any of the samples, both platinized and pure bronzes. The pure sodium tungsten bronzes and even the Pt doped bronzes have such a small catalytic activity that such measurements would probably yield no meaningful numbers. The platinized crystals may be similar to those of Bockris and McHardy (18), so their results can probably be applied to our crystals in this case. Bockris and McHardy studied the mechanism of oxygen evolution and reduction on their platinized samples, and found that the first electron transfer step was the rate determining step. They concluded that this step was probably the same as that postulated for other electrodes in acid solution:

$$O_2 + H^+ + e^- \rightarrow \text{(adsorbed intermediates)}$$

Oxygen reduction was studied on several other tungsten bronzes to determine if the crystal structure or the alkali ion has any effect on the electrocatalytic activity of the bronzes. As the results in Figures 4.13 and 4.14 show, there is little difference between any of the

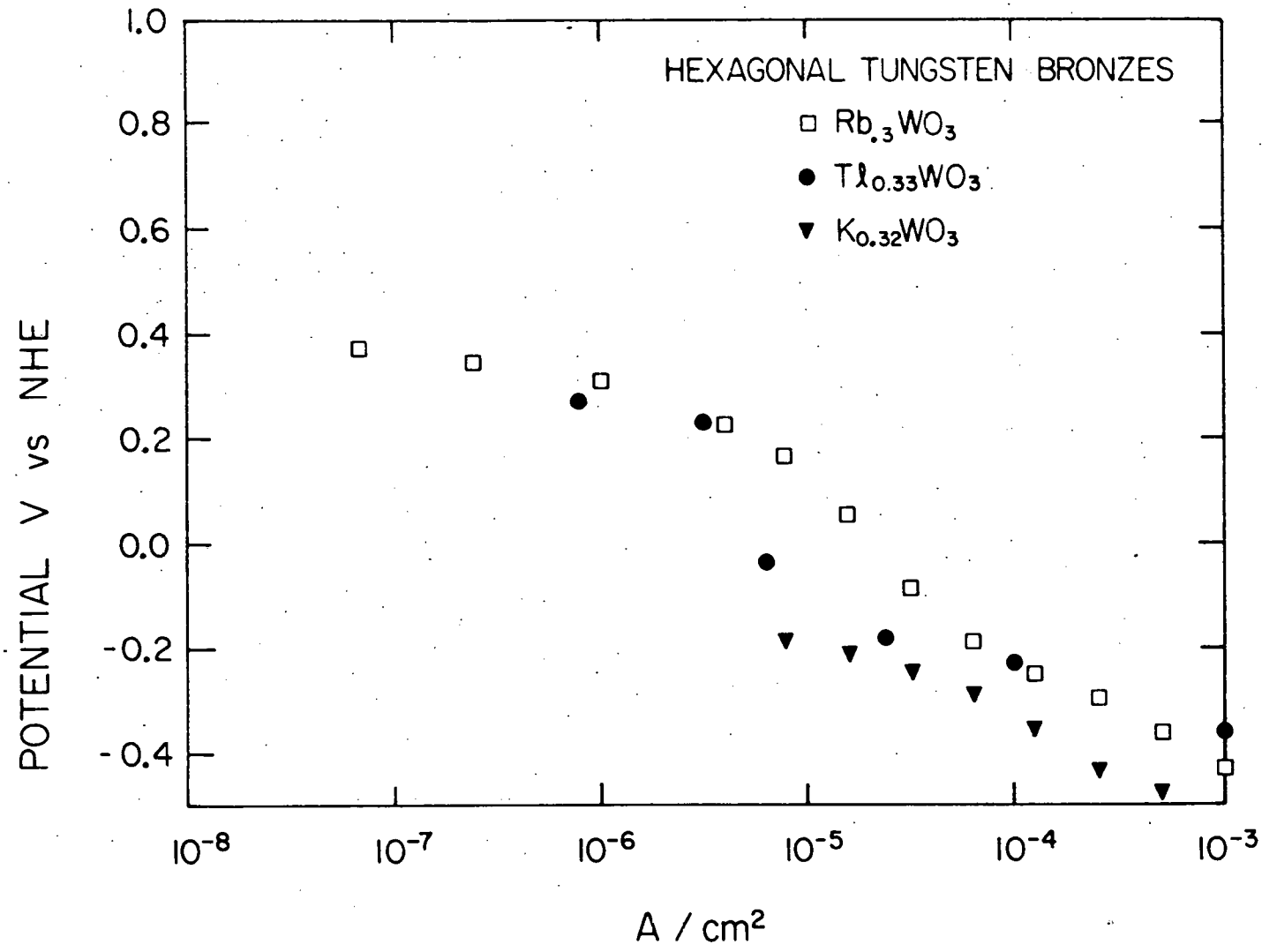

Figure 4.13. Tafel plots for O_2 reduction on three tungsten bronzes with hexagonal crystal structure. Rubidium and thalium tungsten bronzes are similar to sodium tungsten bronze, but potassium tungsten bronze does not catalyze the oxygen reaction, having a rest potential of -0.10 V.

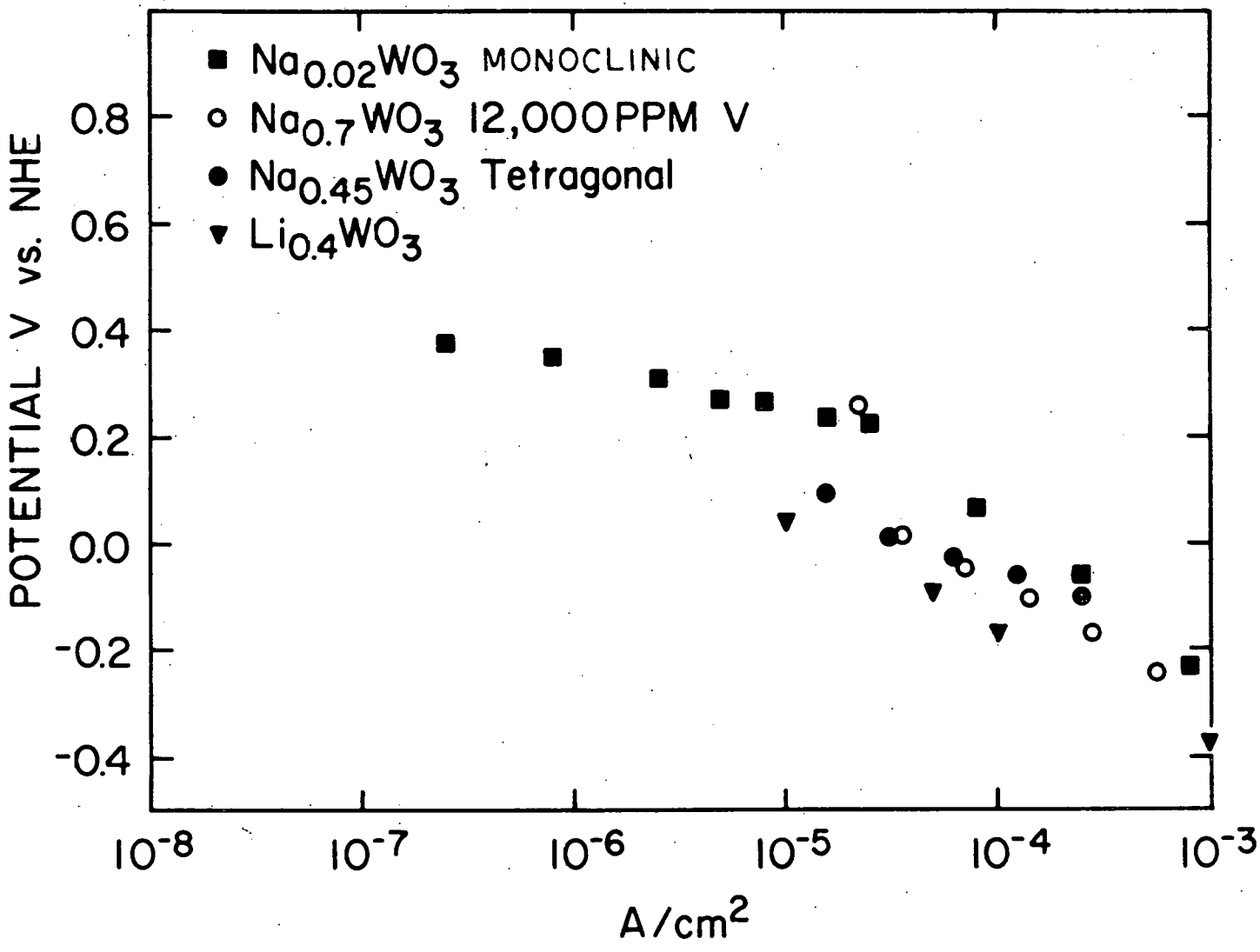

Figure 4.14. Oxygen Tafel plots obtained on WO_3, tetragonal Na_xWO_3, vanadium doped Na_xWO_3, and cubic Li_xWO_3. All are similar to cubic Na_xWO_3 Tafel plots, except Li_xWO_3 which has slightly lower potentials

crystals in the bronze system. Potassium tungsten bronze is the one exemption, and it apparently does not catalyze the oxygen reaction at all. The overpotentials are extremely high at all current densities, and the rest potential is -0.2 V NHE, compared to +0.4 V for the other bronzes. The i-v curves for the rubidium and thallium bronzes are very similar to the curves for Na_xWO_3, which were shown in Figure 4.2.

Data shown in Figure 4.14 were not obtained in the high purity electrochemical system, but in an older cell under moderately pure conditions. On most samples, the data were taken in a smaller range of current densities because the electrode potentials leveled off at the lower current densities. However, the data are sufficiently good to see that WO_3 and tetragonal Na_xWO_3 have the same catalytic activity as cubic Na_xWO_3, and that doping the cubic Na_xWO_3 with large amounts of vanadium has no effect on the i-v curves. Cubic lithium tungsten bronzes gave lower potentials at all current densities.

Oxygen Evolution and Anodic Behavior

Oxygen evolution was shown to be impossible at reasonable potentials on all Pt-free tungsten bronze crystals. The best anode was the as-grown surface of a rubidium tungsten bronze. A steady-state potential of 3.8 volts was recorded at 1 mA/cm^2 on this sample, which is still quite high compared to 1.9 V on platinum at the same current density, but it is the best of any bronze. When a bronze crystal is pulled from the melt at 800°C, considerable differences between the alkali content at the surface and in the bulk can be created, so the exact nature of

that particular crystal was unknown. All polished or cleaved crystals, including $Rb_{0.3}WO_3$, did not support oxygen evolution. Anodic i-v curves for several crystals of the bronze system are shown in Figure 4.15. A polished rubidium tungsten bronze crystal had anodic i-v curves similar to the curve shown for hexagonal potassium tungsten bronze. The large currents, at low potentials, were shown by cyclic voltammetry to be supported by corrosion of the crystal surface, and not by oxygen evolution. For the other bronzes, potentials of up to 9 V were not uncommon at anodic current densities of 1 mA/cm^2. However, there seemed to be a lot of variability among cubic sodium tungsten bronzes, as shown by the two different i-v curves for similar $Na_{0.7}WO_3$ crystals. Sodium was removed from the surfaces of these crystals when anodic potentials were applied. This fact was established by Auger depth analysis. The positive sodium ions are apparently pulled out of the crystal by the high electric fields present at the interface. After the sodium is removed from the crystal, an n-type semiconducting layer remains on the crystal surface (12, 56). When positive potentials are applied, as in oxygen evolution, the majority carriers are swept away from the crystal-solution interface, resulting in diode-like behavior. The semiconductor-electrolyte interface has all the properties of a Schottky semiconductor-metal interface. Mott-Schottky plots have been obtained for anodized sodium tungsten bronzes by Bockris and McHardy (12) and by Randin (56).

Confusing results were reported by Bockris and McHardy, including several values for the flat band potential and a sharp decrease in donor concentration as the potential is raised above 1.1 V NHE. Randin

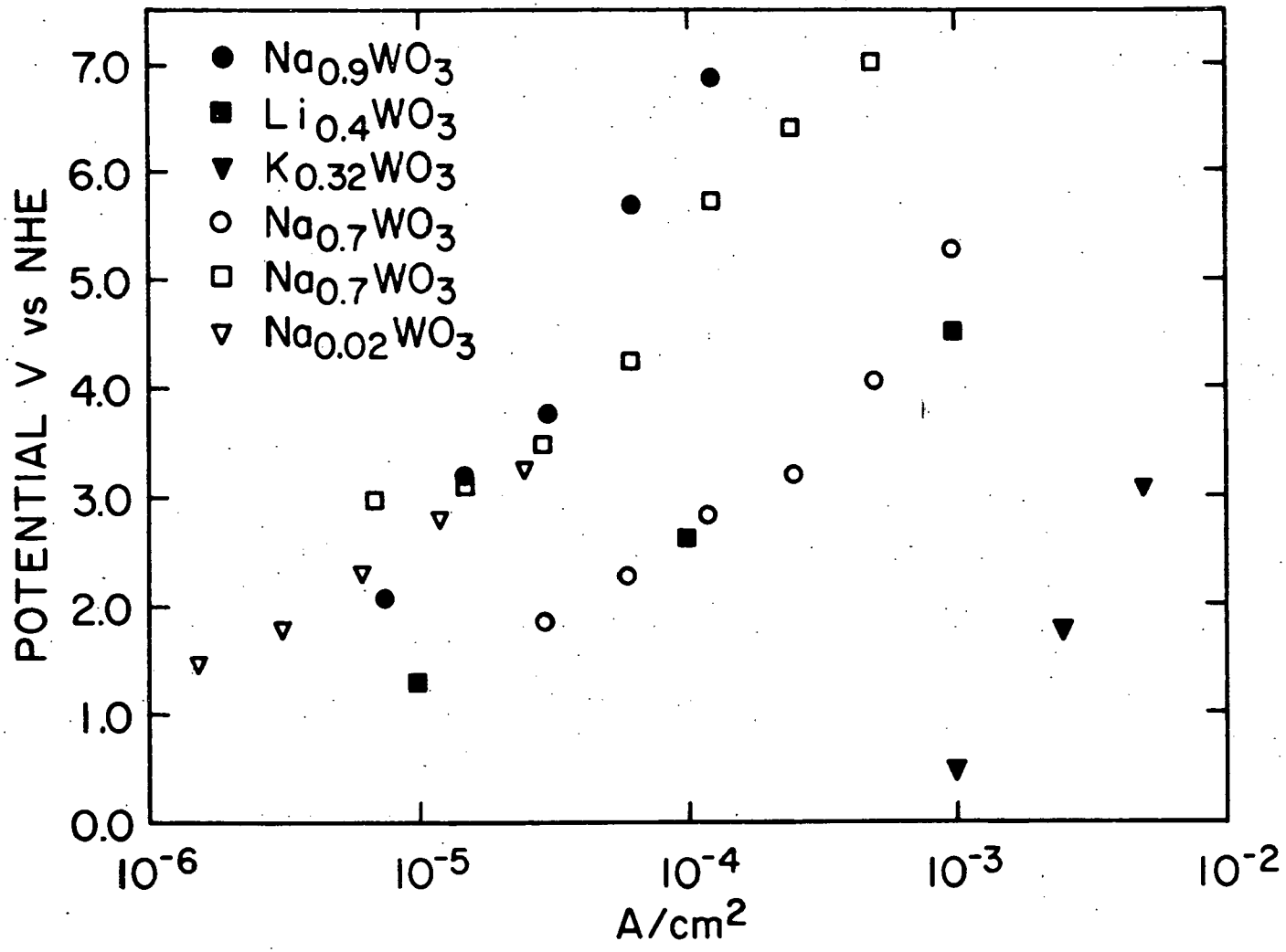

Figure 4.15. Anodic current-voltage characteristics of some tungsten bronze crystals. The surfaces are depleted of the alkali metals and have become n-type semiconductors. The semiconductor-electrolyte interface acts like a Schottky diode

reported a flat band potential of 0.6 V NHE and a sharp increase in donor concentrations above 1.0 V NHE. Our measurements on anodized cubic sodium tungsten bronzes consistently gave Mott-Schottky plots identical to those of Randin, and so our data will not be reproduced here.

Hydrogen Tafel Plots

Exchange currents for hydrogen evolution on anodized cubic sodium tungsten bronze crystals were measured in H_2 saturated solutions. The results, shown in Figure 4.16, agree with the previously reported results of Vondrak and Balej (57), Sepa et al. (58), and Mannan (59), when one takes into account the extremely low x-value of the anodized bronze. The exchange current density for a metallic bronze surface was reported by these researchers to be 10^{-5} A/cm^2. From Figure 4.16, the exchange current density for an anodized bronze is about 10^{-7} A/cm^2. This is to be compared to the high exchange currents of $\sim 10^{-3}$ A/cm^2 on the platinized bronze samples (Figure 4.12). Obviously, not much platinum is needed to activate the sodium tungsten bronze crystals to catalyze the hydrogen reaction, but the amount of data is insufficient to determine if a synergistic effect definitely exists in the Pt-bronze system for the hydrogen reaction.

SEM Studies

Scanning electron microscopy provided a direct visual study of the bronze surfaces which were used in the electrochemical studies. The SEM pictures were needed to reveal the forms in which platinum was deposited on the bronze surface, as well as to provide an approximation of surface

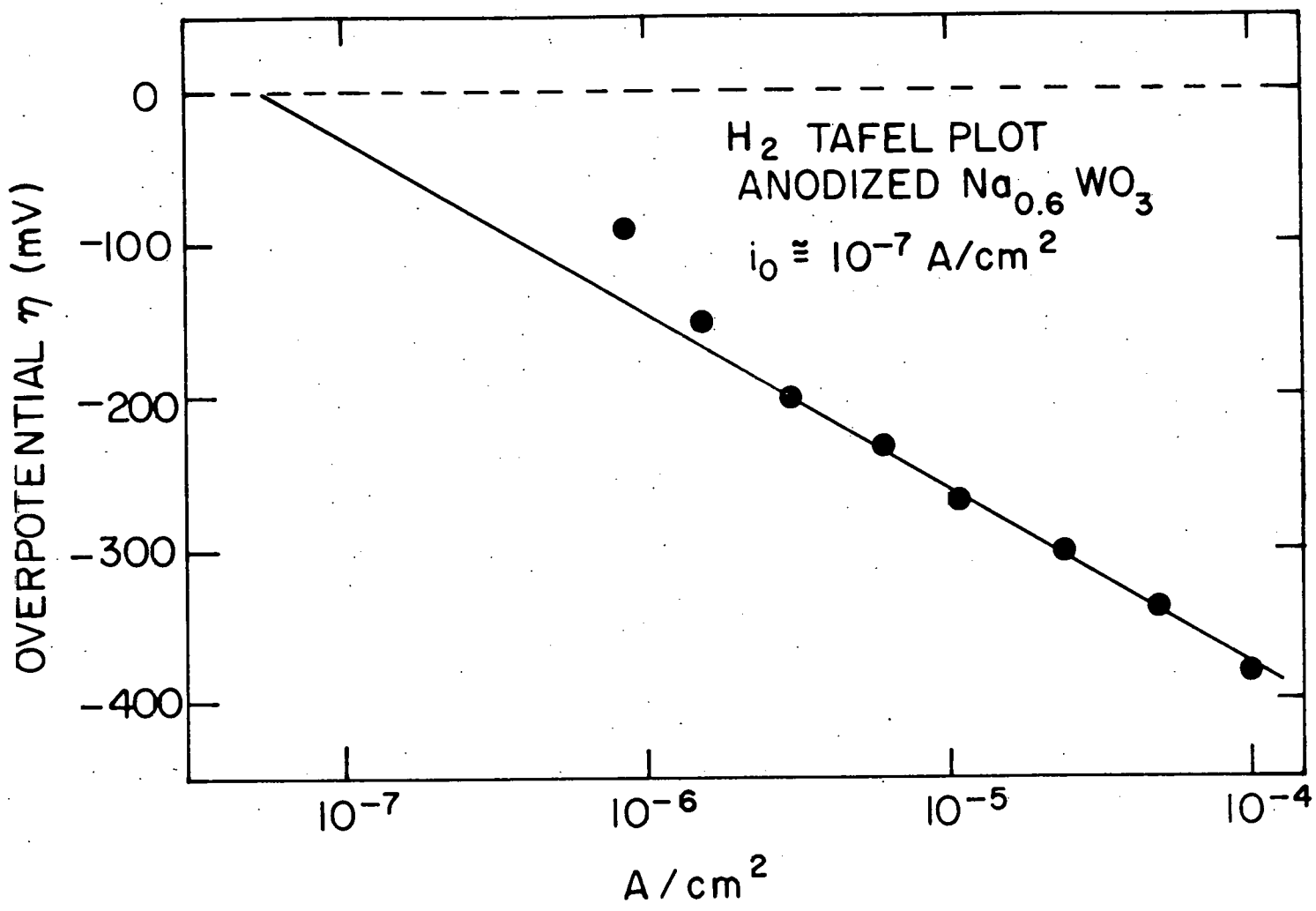

Figure 4.16. Typical H_2 Tafel plot for an anodized Na_xWO_3 crystal. The slope is 120 mV/decade and the exchange current is approximately 10^{-7} A/cm^2. Such a low exchange current is very poor for a hydrogen electrode

areas and corrosion rates of the crystals.

Evidence from the cyclic voltammetry data on cubic Na_xWO_3 indicated small corrosion rates at high anodic potentials, implying that this particular bronze surface is fairly stable against anodic corrosion in acid solutions. The scanning electron microscope (SEM) pictures gave more evidence to support this conclusion. The SEM picture in Figure 4.17 shows the surface of a polished $Na_{0.6}WO_3$ crystal which was anodized to 9 V at a current density of 1 mA/cm^2. This particular crystal was not electrochemically cleaned by potential cycling, nor was this crystal used in the high purity test cell. Consequently, considerable foreign matter remained on the surface and can be seen in the photograph. There are few corrosion etch pits or other rough features caused by the anodization process. A few polishing scratch marks are barely visible in the photograph. Platinum deposition by electrochemical plating from a dilute chloroplatinic acid (H_2PtCl_6) solution was first attempted with cleaved crystals, but the SEM photograph revealed large (2-3 μm) Pt platelets growing perpendicular to the surface. Crystals which were to be Pt plated were therefore first polished, anodized, and mounted on a rotating electrode arrangement to provide a more even Pt distribution. Samples 376B#1 and 376B#2 were plated in this manner and SEM photographs of their surfaces are shown in Figures 4.18 and 4.19 respectively. These crystals are the samples discussed earlier which had roughly equal Pt coverages, but the sample with slightly less Pt (376B#2) had a much greater catalytic activity for O_2 reduction (see Figure 4.9). A lower magnification photograph of sample 376B#1 is shown in Figure 4.20 to

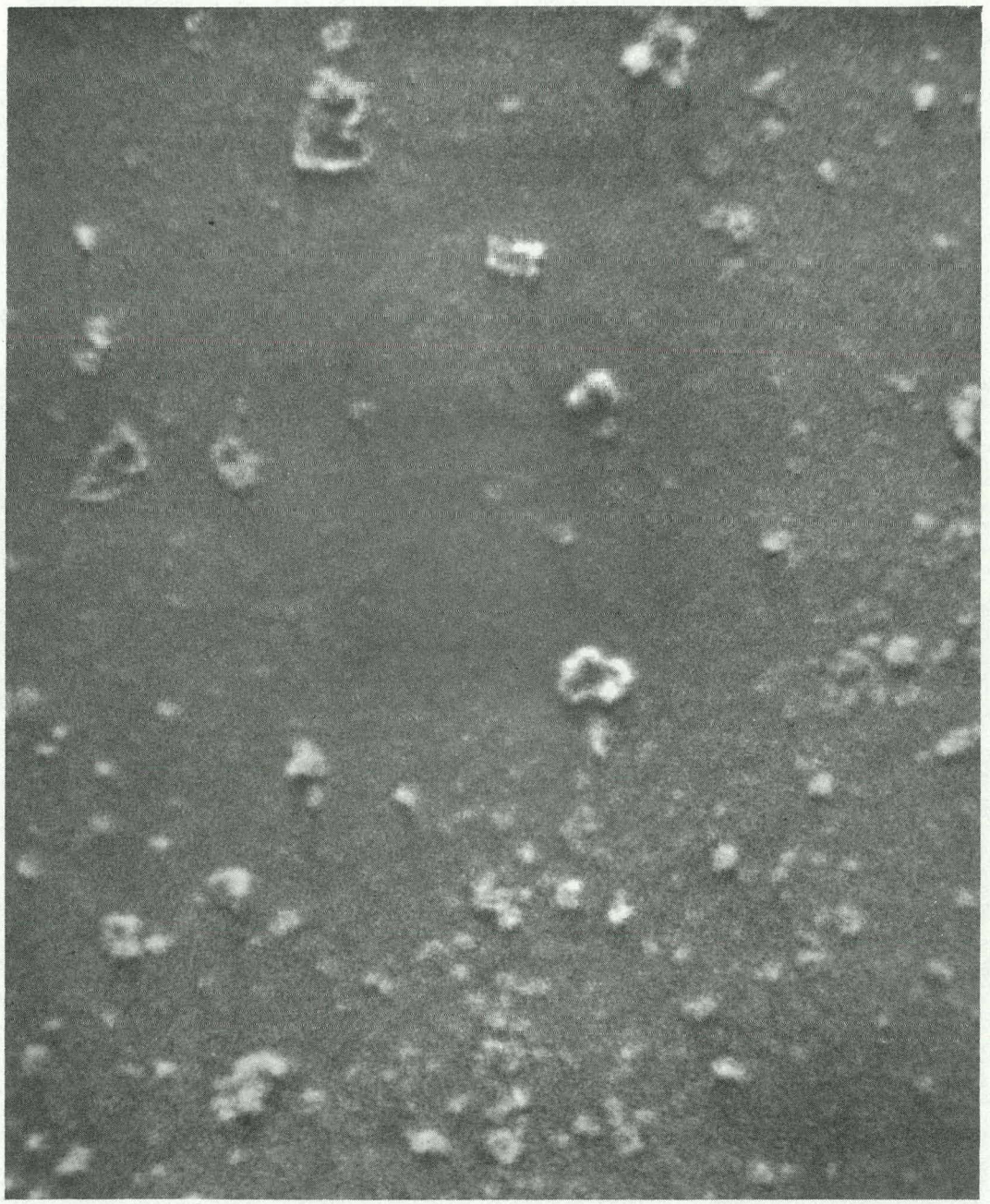

Figure 4.17. SEM photograph of a polished $Na_{0.6}WO_3$ crystal which was anodized to 9.0 V NHE. Considerable amounts of foreign matter are present on this sample, but otherwise the surface is quite smooth and shows no evidence of corrosion. The magnification is 40,000X

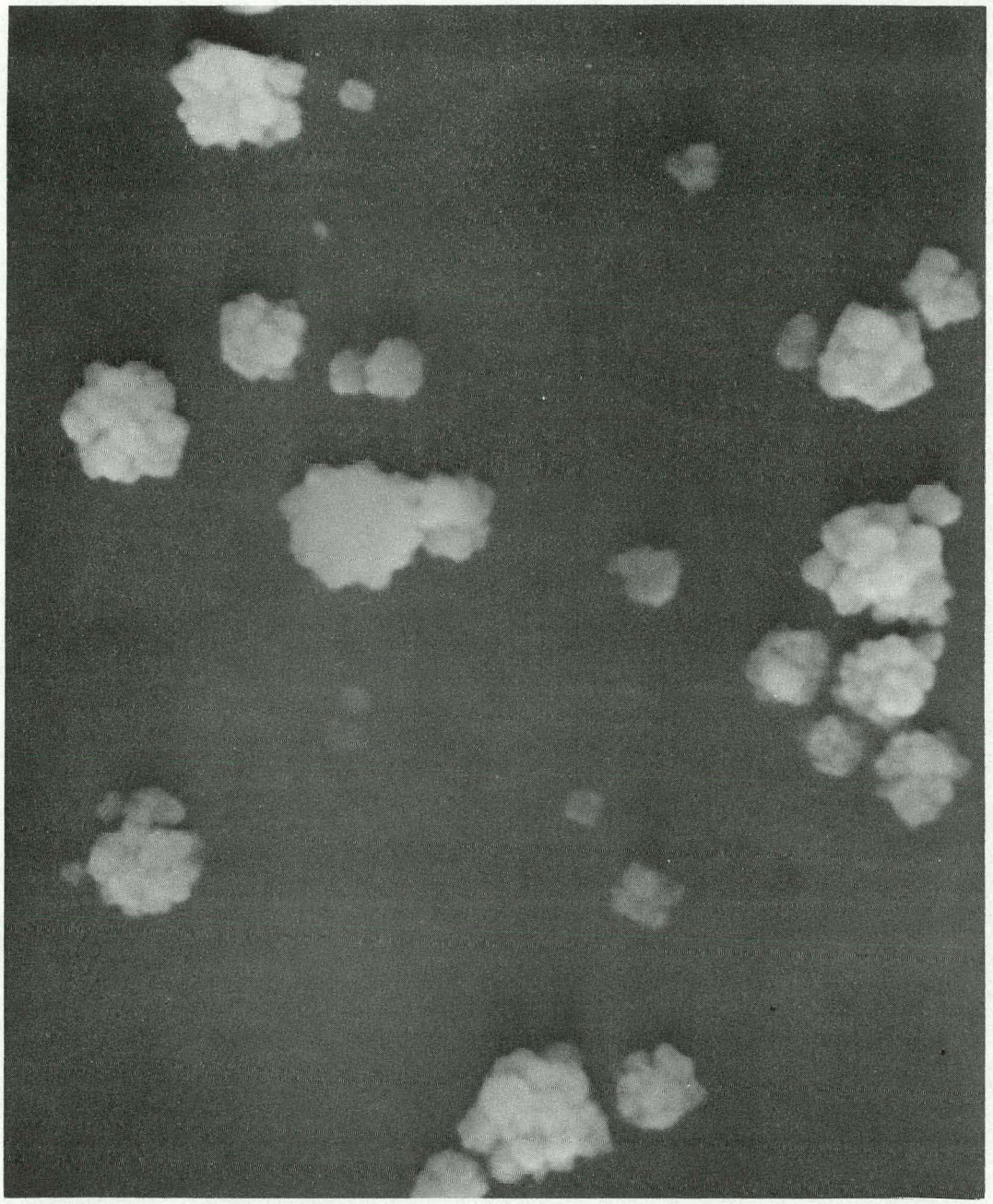

Figure 4.18. SEM photograph of a polished and anodized $Na_{0.6}WO_3$ crystal (376B#1) which was Pt plated at 0.120 V NHE in 7.5×10^{-5} M chloroplatinic acid. The Pt was not deposited uniformly, as this photograph revealed small (3,000 Å diameter) Pt particles on the surface. The magnification is 40,000X

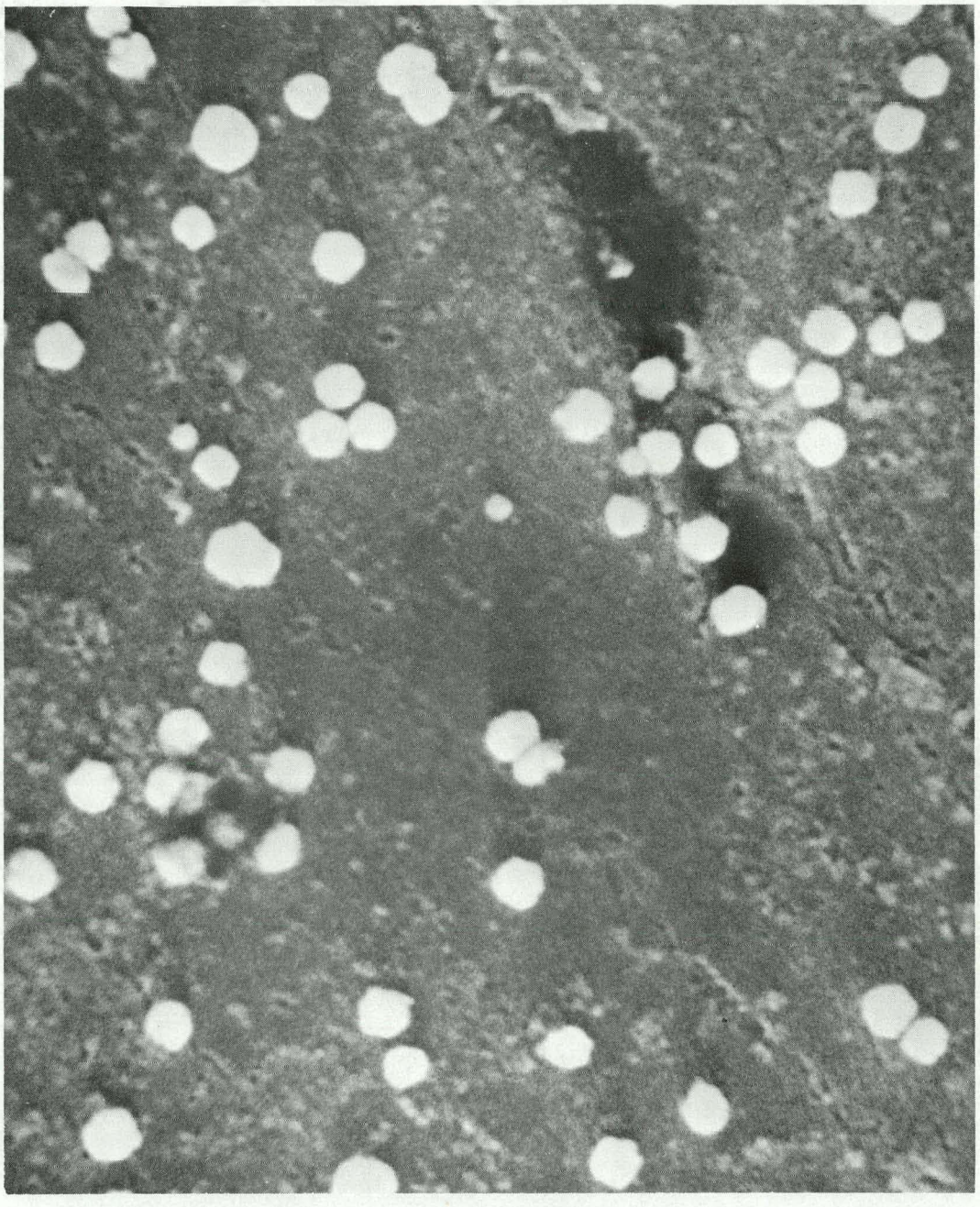

Figure 4.19. SEM photograph of a polished and anodized $Na_{0.6}WO_3$ crystal (376B#2) which was Pt plated at 0.040 V NHE in 7.5×10^{-5} M chloroplatinic acid. Platinum particles 1,500 Å in diameter were found on this surface. The magnification is 40,000X

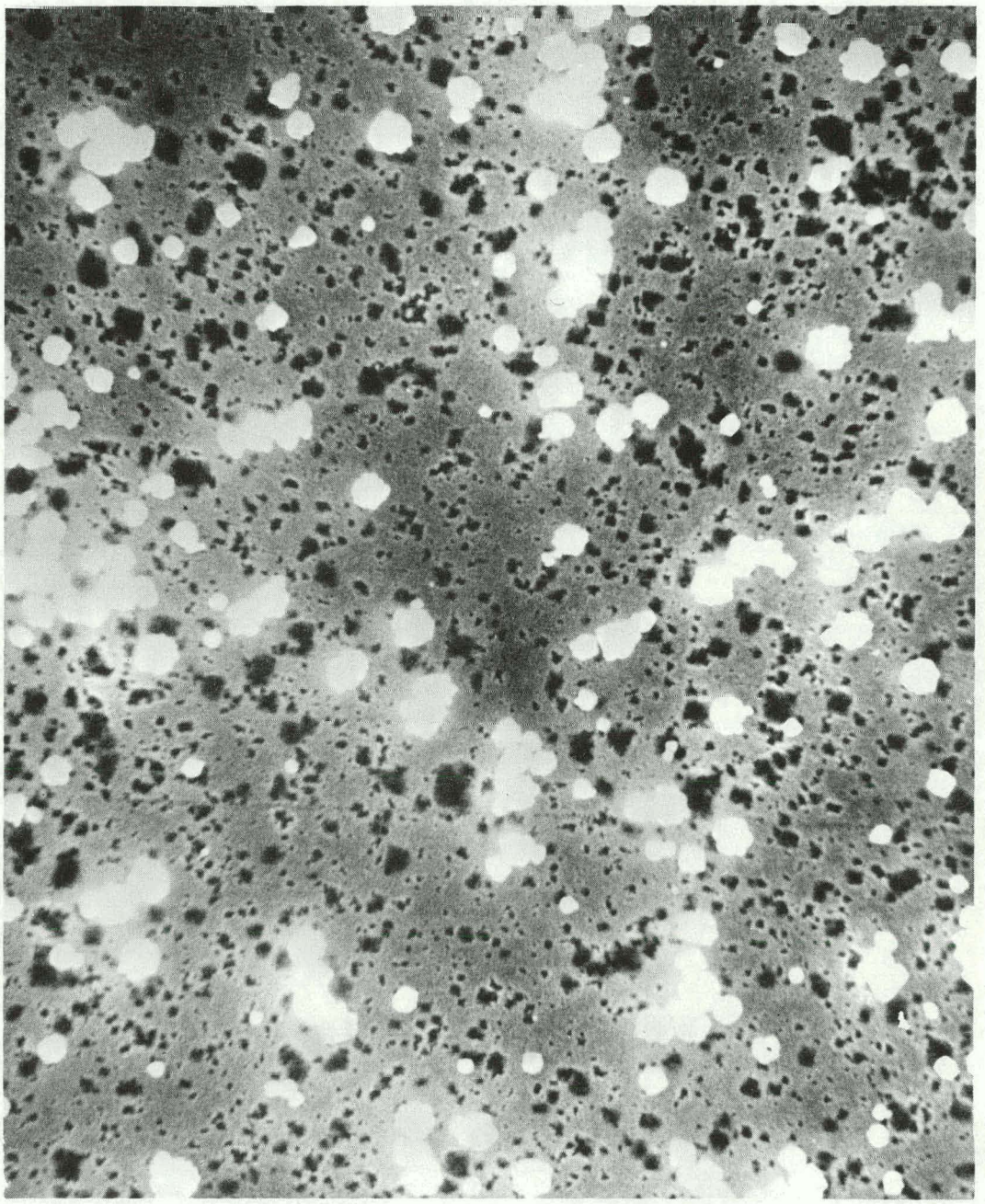

Figure 4.20. Same surface as in Figure 4.18 but at a lower magnification. In this photograph, the lighting is enhanced to show the features of the bronze surface instead of the platinum particles. Magnification is 12,000X

give a better indication of the Pt particle size distribution and coverages. The individual particles on the surface were shown to be Pt by using the SEM electron beam as a microprobe while monitoring the x-ray output lines. Photographs of other crystals plated in the same manner revealed similar platinum particles. The average particle size in Figure 4.20 is 3,000 Å, and those in Figure 4.19 average 1,500 Å in diameter. Later Auger analysis of these crystals agreed rather well with the visual observation that the crystals have approximately equal Pt coverages. The fact that sample 376B#2 was the much superior oxygen catalyst implies a difference exists between these two crystals that is not readily seen in the photographs.

Platinum particles were not present on all crystals which exhibited high catalytic activities. Sample 376A#7 was prepared in the same manner as sample 376B#2. After plating and testing for catalytic activity, sample 376A#7 was reanodized to 9 volts. The catalytic activity remained the same after the reanodization (see Figure 4.8), but the SEM photograph shows no Pt particles. The SEM photograph is shown in Figure 4.21. The surface is rather rough with many etch pits, but no Pt particles are visible. Auger analysis gave a Pt coverage of 0.07 percent. Cubic sodium tungsten bronzes with a catalytic activity close to that of pure Pt were prepared by using a Pt counter electrode in the same compartment to sweep the potential on the bronze repeatedly from -0.25 V NHE to 1.8 V NHE. These samples were cleaved crystals, and the SEM photograph of one of these crystals (365C#2) is shown in Figure 4.22. No Pt particles are visible in this photograph either, even

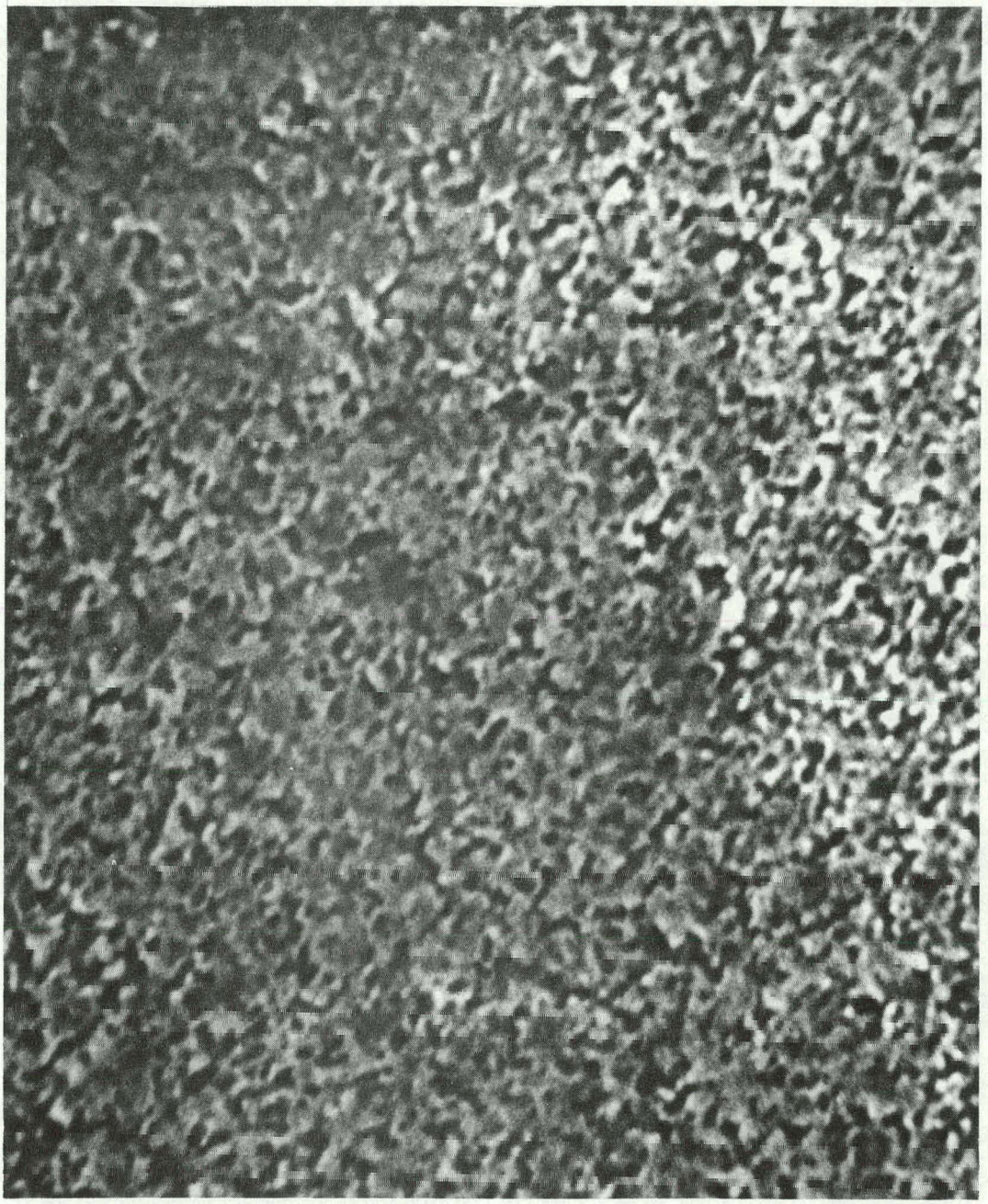

Figure 4.21. SEM photograph of an anodized, platinized, and reanodized $Na_{0.6}WO_3$ crystal (376A#7). No Pt particles remain, but the surface is quite rough with many corrosion pits. The catalytic activity of this surface was very good. The magnification is 40,000X

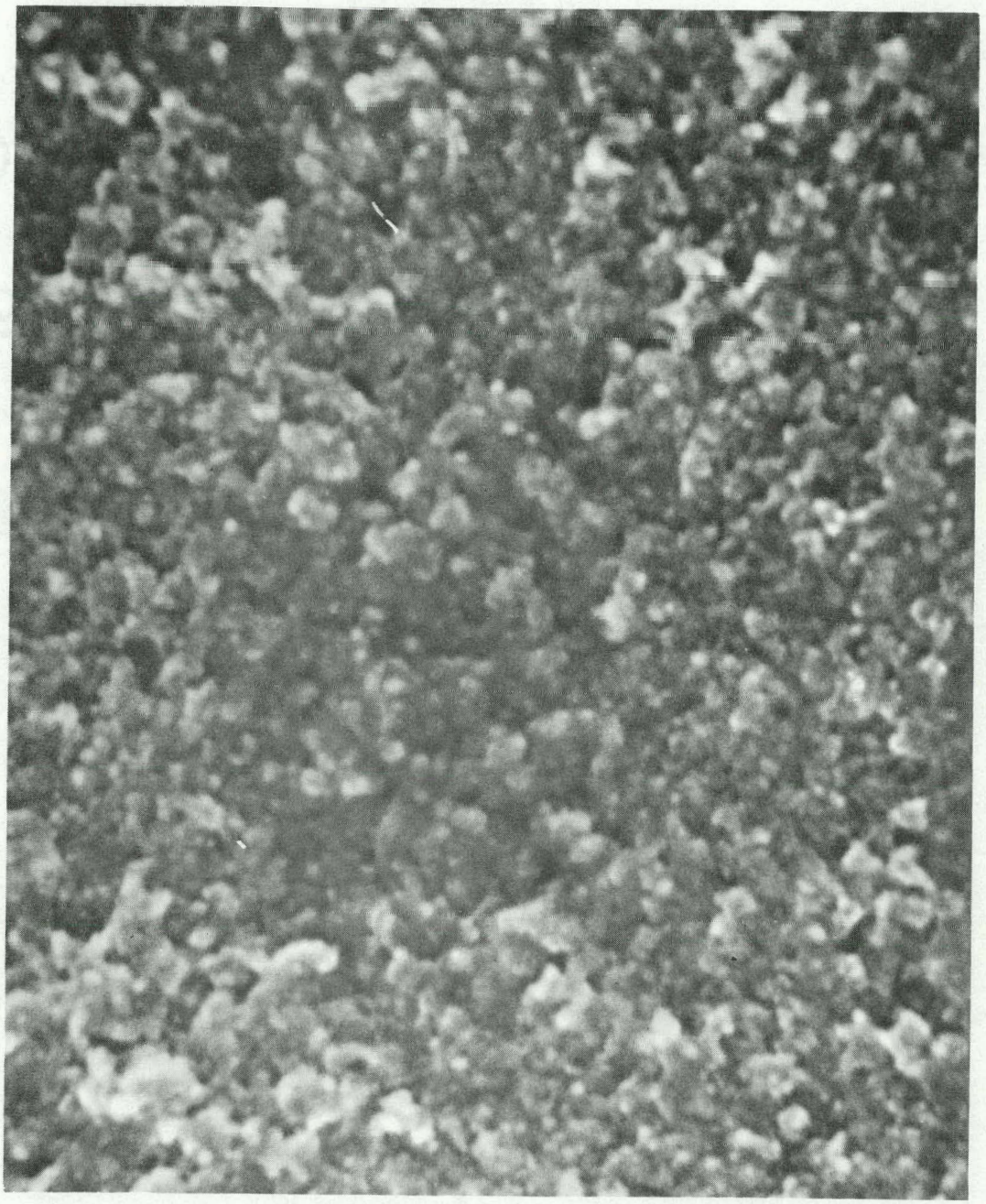

Figure 4.22. SEM photograph of an anodized and platinized $Na_{0.7}WO_3$ crystal (365C#2). Platinum was deposited *in situ* by transport from a large Pt foil. The Pt coverage is 22 percent, but no Pt particles are visible. The magnification is 40,000X

though the Auger analysis revealed a Pt coverage of 22 percent. The exact form in which the Pt exists on the surfaces of these samples is still unknown.

All of the platinized crystals have rather rough surfaces, with numerous etch pits, particularly sample 365C#2. However, in the case of sample 365C#2, 12 hours of cyclic voltage scans were needed to deposit the Pt. The other samples were subjected to numerous voltage scans and i-v measurements for complete sample characterization. The surface roughening is probably due in most part to the cyclic voltage scans.

An anodized sodium tungsten bronze, with no platinum, is a poor catalyst for the hydrogen reaction, as was shown by the cathodic H_2 Tafel plot in Figure 4.16. Rather large, negative potentials were obtained at the higher current densities; which undoubtedly created a high x-value hydrogen tungsten bronze in the sodium depletion layer. (For details of the hydrogen tungsten bronze formation, see the section on the cyclic voltammetry results.) The effect of these large, negative potentials on the bronze surface are shown in Figures 4.23 and 4.24. The striking features of these photographs are the cracked sodium depletion layer, which is flaking off the surface in some spots, and the extremely smooth surface of each flake. There are no etch pits and not even the remains of any polishing scratches. Other pictures with a magnification of 40,000X also show a very smooth surface on each flake. Vondrak and Balej, in their paper on hydrogen absorption by sodium tungsten bronzes (60), reported the development of deep cracks in the surfaces of crystals which were subjected to long polarizations at -0.8 V NHE.

Figure 4.23. SEM photograph of the cracked surface on a strongly reduced $Na_{0.6}WO_3$ crystal which had been previously anodized. Aside from the cracks, the surface is very smooth except for the small round particles which are of unknown composition. The magnification is 6,000X

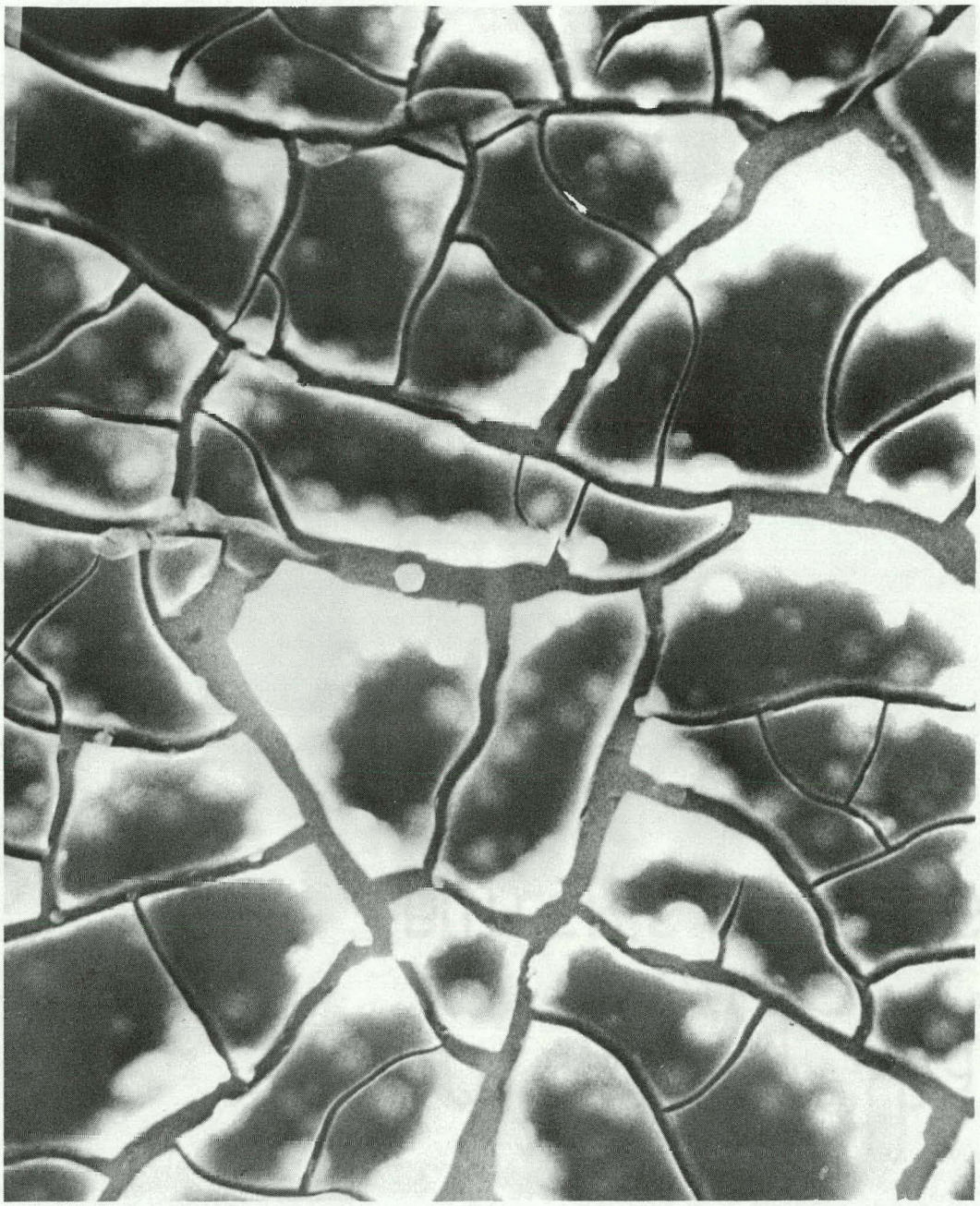

Figure 4.24. SEM photograph of a different spot on the same crystal pictured in Figure 4.23. Here the cracks can be seen to be only in the sodium depletion layer which is flaking off the crystal. The magnification is 6,000X

Auger Analysis

Auger Electron Spectroscopy (AES) was used to determine the surface chemical composition of the anodized and platinized alkali tungsten bronze crystals. The analysis was performed by Dr. A. J. Bevolo of the Ames Laboratory in the surface analysis laboratory. Most of the work was concerned with the sodium tungsten bronze system. The first objective was to measure the sodium content of an anodized sodium tungsten bronze surface. Other workers (12, 13, 56) have studied the semiconducting surface layer of anodized bronze crystals, but good profiles of sodium content as a function of depth have not been reported. Depth profiles for two crystals, anodized to different potentials, are shown in Figures 4.25 and 4.26. The first crystal was anodized with 0.5 mA/cm^2 for 3 hours, during which time the potential slowly rose to 5.5 V NHE. Sodium was depleted to a depth of approximately 800 Å, although there was no sharp cutoff in the sodium concentration. The x value at the surface was about 0.25. The second crystal was anodized with 1 mA/cm^2 for 9 hours, and the final potential was 9.0 V NHE. The abscissa on this graph (Figure 4.26) is in units of the sputtering time, but to a good approximation, 1 minute corresponds to 1 angstrom with the sputtering parameters used for this depth profile. Sodium depletion extends to a depth of 1,500 Å. The bulk sodium x-value for this crystal was known to be 0.6, so the x-value in the depletion region near the surface is about 0.1. These numbers were consistently measured on crystals anodized under the same conditions. Considering the high potentials needed to create the depletion layer, reports of depletion layers over

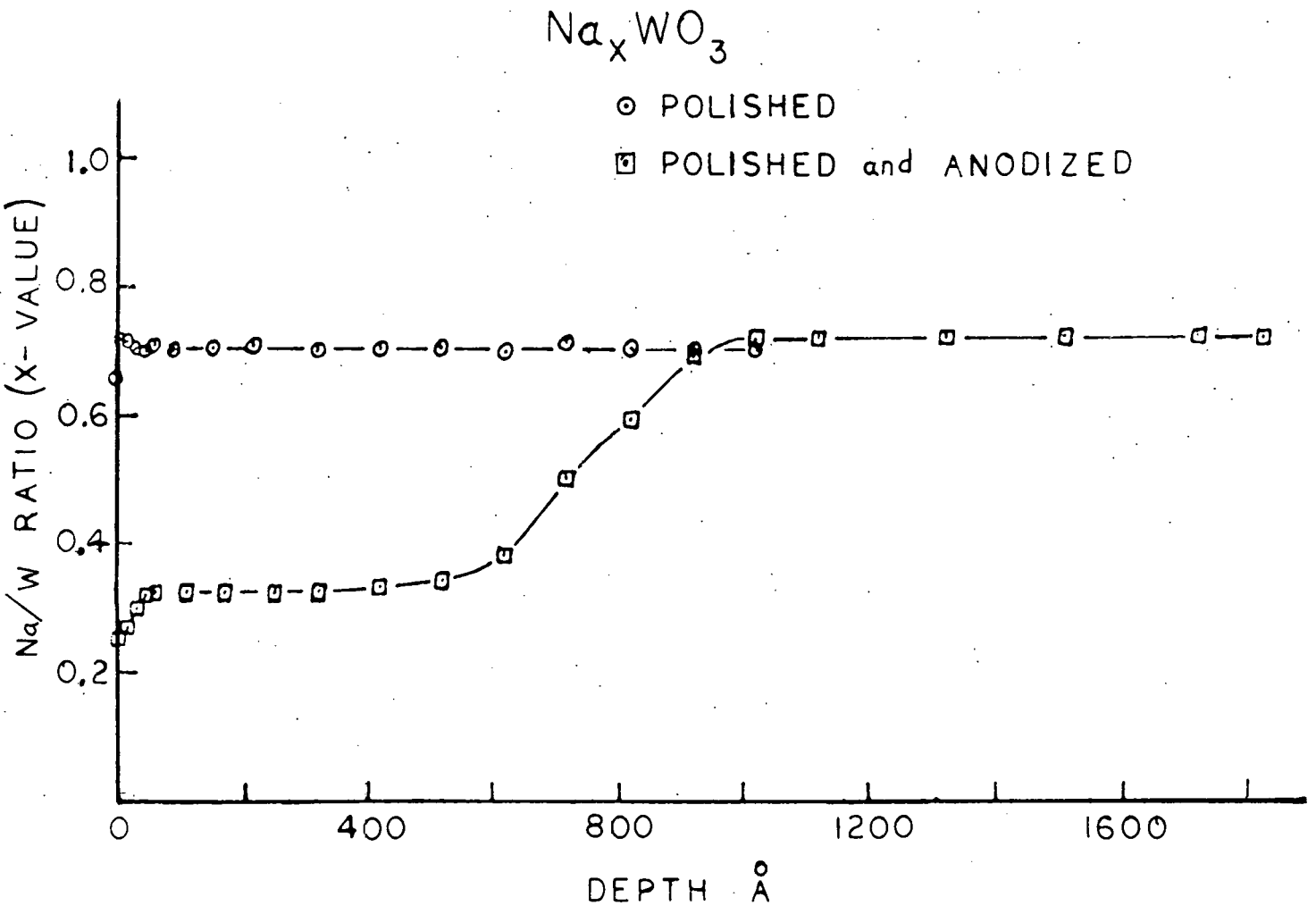

Figure 4.25. Auger depth profiles of a fresh polished crystal and a polished crystal which has been anodized to 5.5 V. The x-value at the surface of the anodized crystal is 0.25 and the thickness of the depletion layer is 800 angstroms (analysis performed by PHI Electronics Inc.)

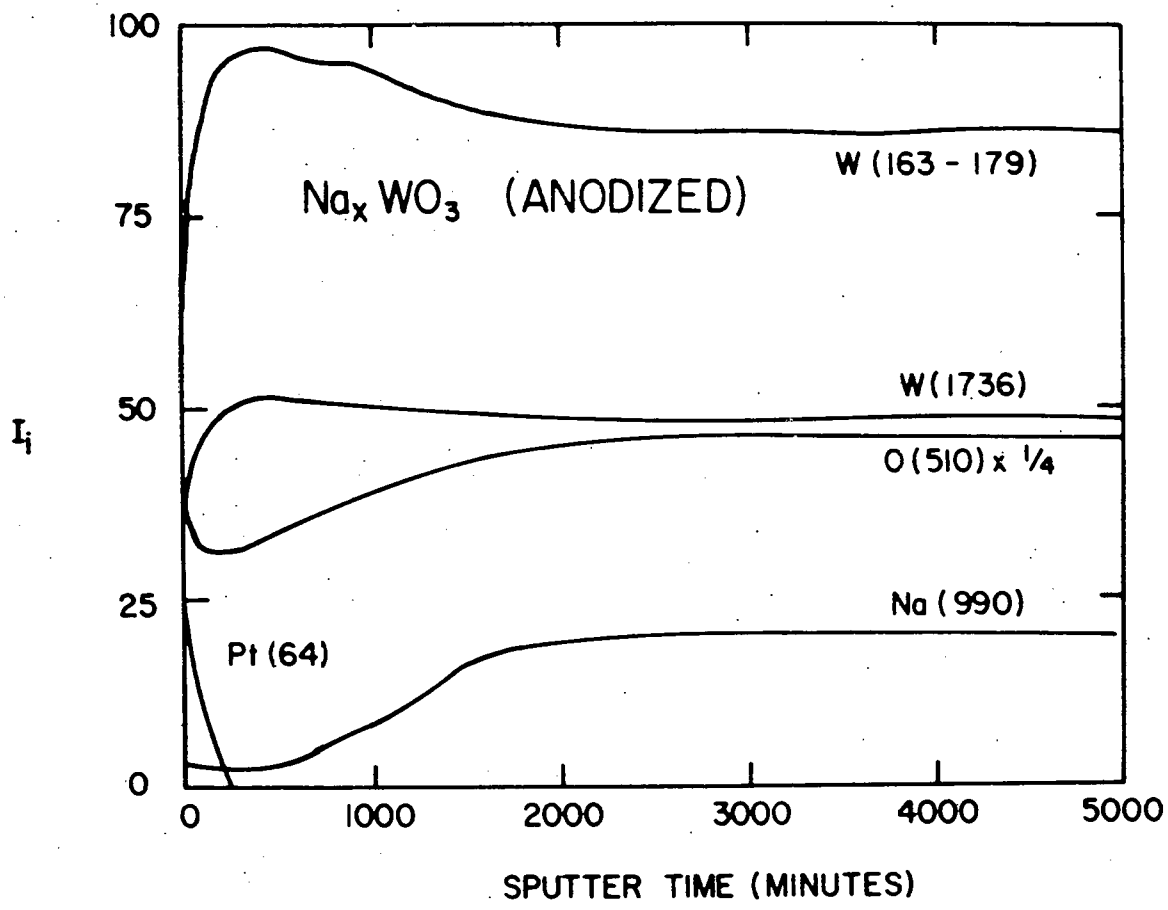

Figure 4.26. Extended depth profile showing sodium depletion layer on a sample (376A#2) anodized to 9 V. Platinum was plated onto the crystal after anodization. The sodium depletion layer was 1,500 Å thick and the sodium content near the surface is 0.08. The abscissa can be read approximately as angstroms

100 μm thick (25) must be viewed with considerable skepticism. The ion microprobe results of Bockris and McHardy (12) indicated depletion layers over 1,000 Å thick on samples anodized to only 2 volts. In view of the consistency of our measurements, a 1,000 Å depletion layer formed by only 2 volts seems unreasonably high.

Platinum coverages on the platinized and Pt contaminated crystals were also measured by AES. The first such samples examined were the Pt doped crystals used in the Pt pre-electrolyzed solutions. Platinum was shown to have plated out onto the bronze crystal from the solution. A Pt doping of 800 ppm (0.08%) is below the limits of the Auger sensitivity and no Pt was detected on the surface of such a crystal. An Auger trace at the highest instrumental gain is shown in Figure 4.27 for such a crystal. No Pt peak appears near 1967 eV, which is the position of the high energy Pt Auger transition. However, a definite Pt Auger signal, shown in Figure 4.28, was obtained on a similar crystal after it was used in a Pt pre-electrolyzed solution as both an anode and a cathode. The tungsten 1796 eV and Pt 1967 eV Auger lines have about equal sensitivities, so equal signals at gains of 1 and 100 respectively, indicate a Pt/W ratio of 0.01 on the surface or a Pt coverage of about 0.3%. The value of 0.3% is arrived at by assuming a surface composition of WO_2, due to electron beam induced oxygen desorption. The measured oxygen content on the surface was always much too low and usually corresponded to oxygen stochiometries of 2 or less. The assumption of a surface of WO_2 is only a rough approximation, but was used consistently to determine the Pt surface coverages from the Pt/W ratios.

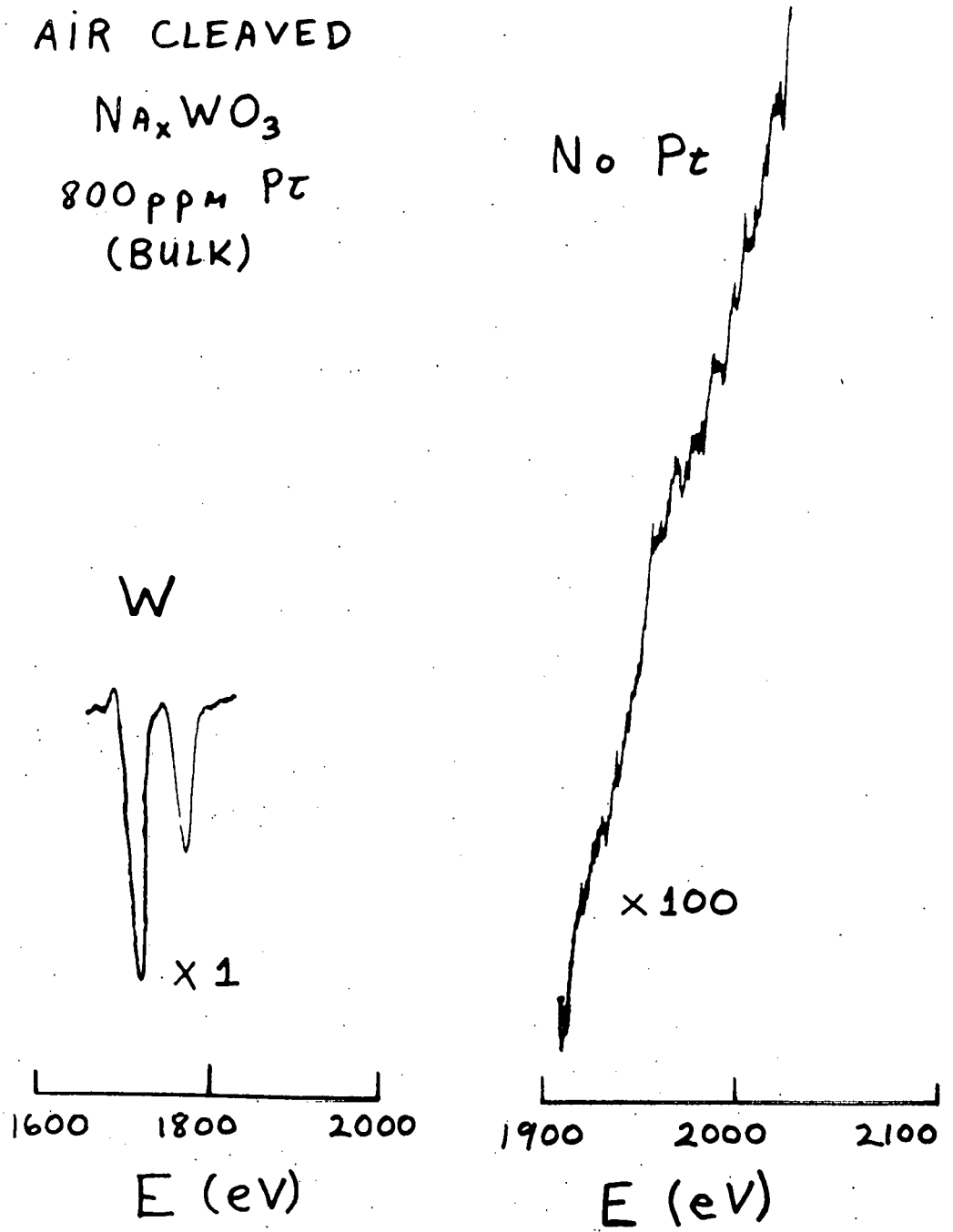

Figure 4.27. Auger high energy spectrum on a Pt doped (800 ppm) sample. Platinum has a high energy line at 1967 eV but no Pt signal is detectable in this trace

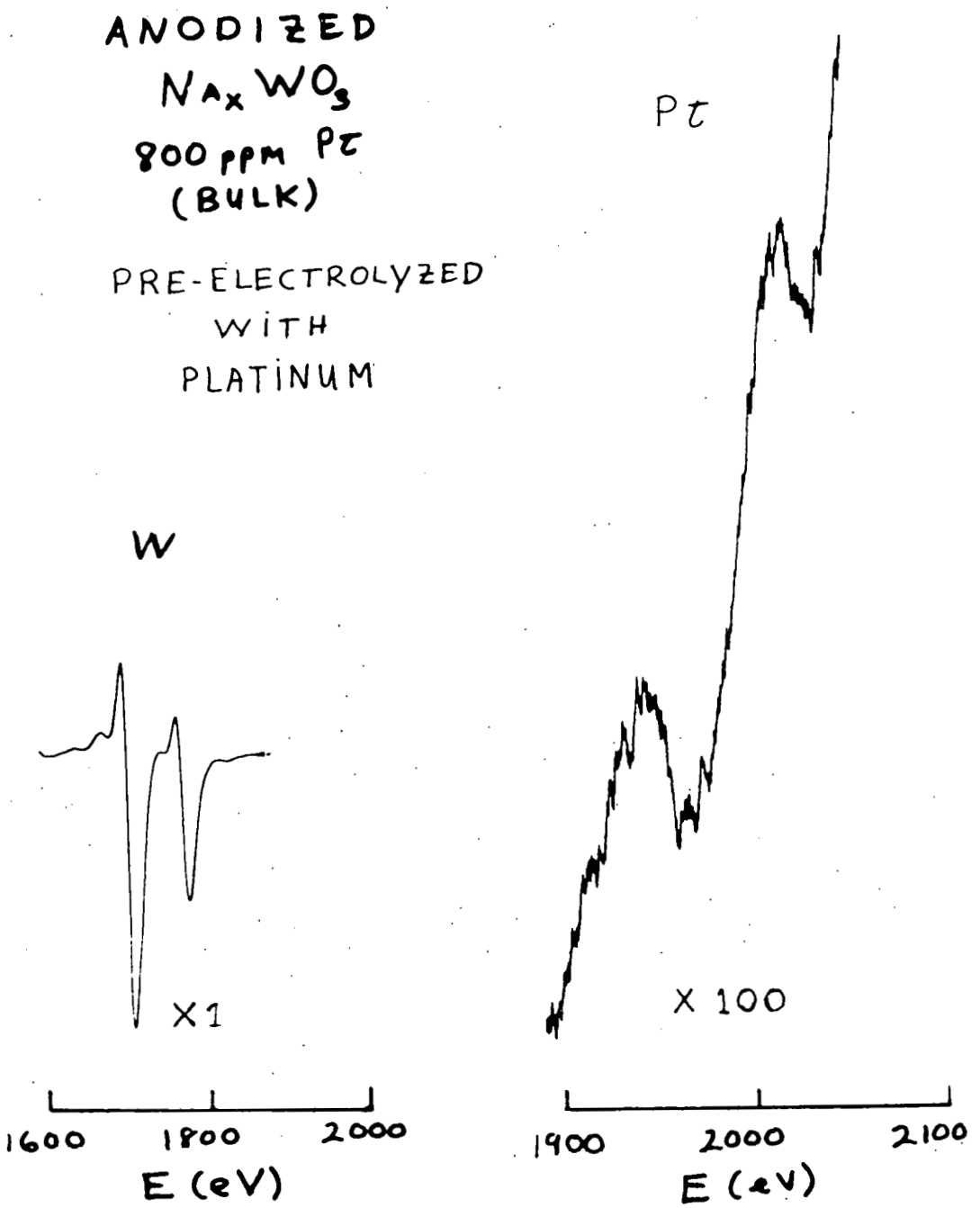

Figure 4.28. Auger high energy spectrum on an 800 ppm Pt doped crystal which was used as an electrode in a Pt pre-electrolyzed solution. The Pt/W ratio is approximately 0.01

All of the platinized sodium tungsten bronze crystals were analyzed to measure the surface Pt coverages, and a depth profile was performed on some crystals to find the thickness of the Pt deposits. A typical depth profile for a crystal plated from chloroplatinic acid is shown in Figure 4.29. The scale on the ordinate is relative. The data plotted as a function of depth were taken directly from the measured peak to peak Auger line intensities and were not normalized at each depth. For the latter reason, the tungsten appears to increase with increasing depth only because the carbon and Pt are decreasing. The sputtering ion beam was 30 nA and an average sputter rate of 2/incident ion was assumed for the tungsten bronzes. With these parameters the sputtering rate was about 1 Å/min, so the scale on the abscissa can be read in angstroms. Integration of the Pt profile gives approximately 2 $\mu g/cm^2$ of Pt on the surface.

The Pt 64 eV line intensity dropped to zero long before the 1967 eV line does, which implies a serious Pt knock-on problem. The high ion energies used in sputtering drive some Pt atoms into the crystal instead of sputtering them away. The low energy Pt line is not detected from these atoms because they are below the surface of the crystal. A 5 keV argon ion beam was used to depth profile this sample, but on subsequent samples a low ion energy (2.5 keV) was used and the problem was much less serious. An extended depth profile of this sample was shown in Figure 4.25 to give an indication of the sodium depletion layer. From the profile in Figure 4.25 the oxygen desorption problem is quite noticeable in the sodium depletion layer.

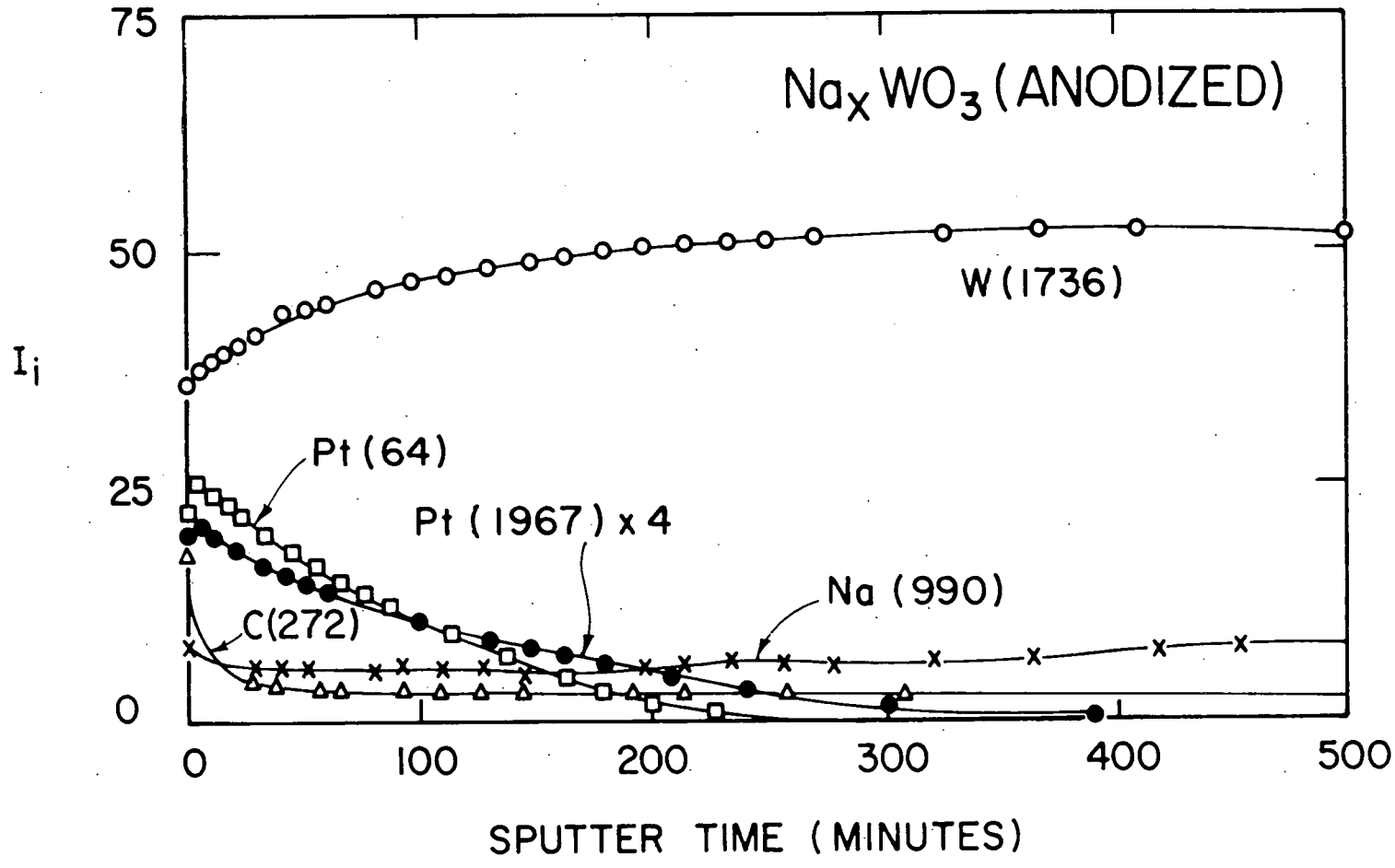

Figure 4.29. Auger depth profile of a sample (376A#2) plated from chloroplatinic acid. (The abscissa can also be read in angstroms.) The surface Pt/W ratio is 0.22 and the sodium depletion layer extends to 1,500 angstroms. The Pt 64 eV line intensity drops to zero at 250 angstroms. Assuming a Pt sputter rate of 4/incident ion, the Pt deposits are 500 angstroms thick

Platinum can be deposited on nonanodized bronze crystals, as the depth profile in Figure 4.30 shows. Although the sodium Auger line intensity drops sharply near the surface, this is not an indication of a sodium depletion layer, because the tungsten line intensity drops just as rapidly. All intensities are lower at the surface due to the carbon layer on the surface. This sample was used as an anode with 1 mA/cm^2 anodic currents, but the potential never exceeded 3 V and no sodium was depleted from the surface of the crystal. The Tafel plot for this platinized crystal was shown in Figure 4.6, and the Pt coverage was approximately 0.03. Apparently the Pt stabilizes the bronze surface against anodic dissolution by providing a competing reaction, that of oxygen evolution. An interesting feature of this depth profile is the way the oxygen Auger intensity parallels the sodium line intensity. This same phenomenon was observed with the depth profile shown in Figure 4.26. The reason for this trend is not known.

Sodium tungsten bronzes with x values $0.25 \leq x \leq 0.5$ have a tetragonal crystal structure and are metallic conductors. A sodium depletion layer 1,200 Å thick was found on a tetragonal $Na_{0.45}WO_3$ crystal which had been anodized to 5 V NHE.

The Auger analysis revealed no depletion layers on the hexagonal crystals of potassium, thallium and rubidium tungsten bronzes. The thallium tungsten bronze crystal had been anodized to 5.0 V. The existence of a detectable thallium depletion layer is implied by such a high overvoltage. At least a small alkali depletion layer was expected on the potassium and rubidium tungsten bronzes, because of the results

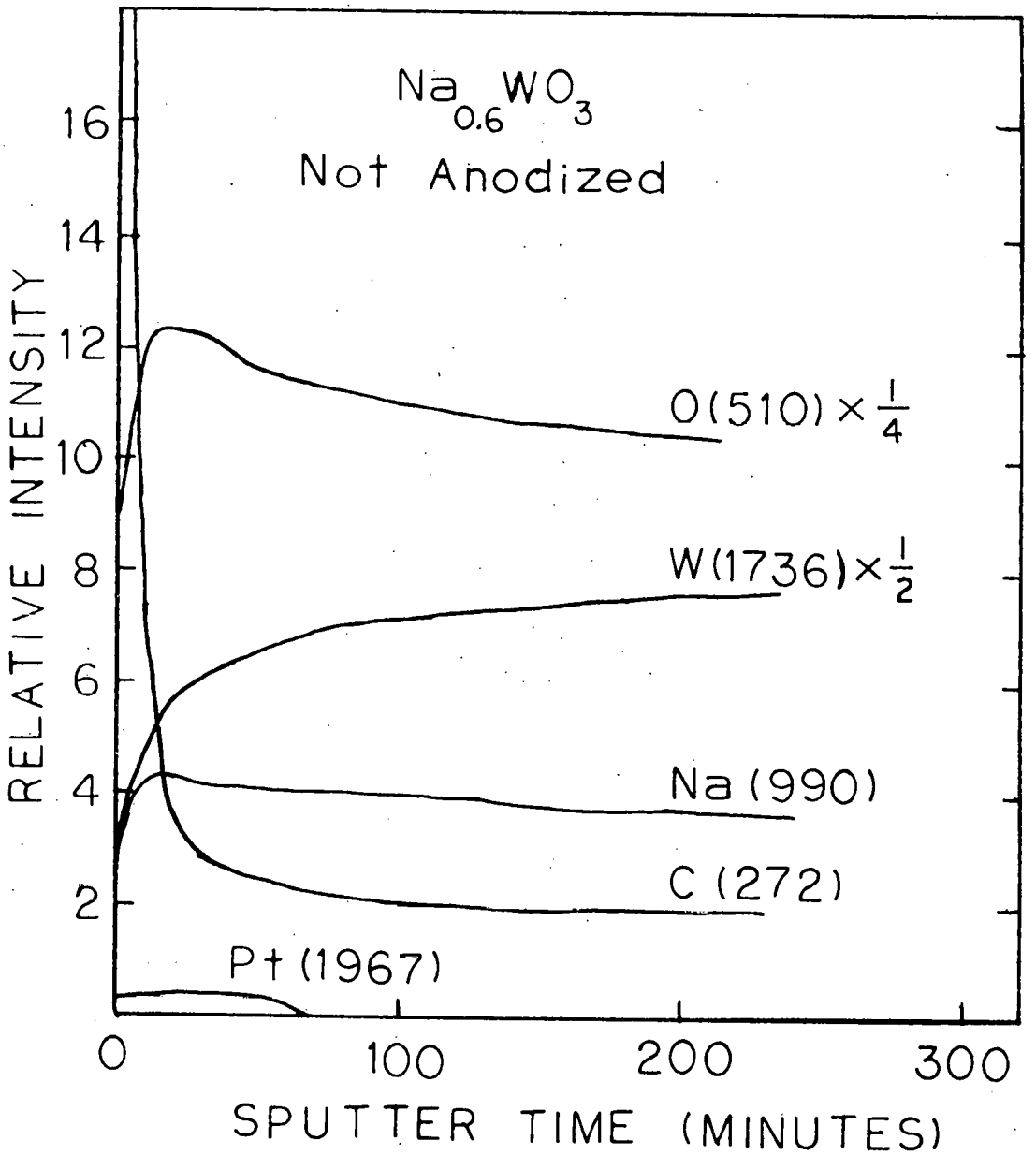

Figure 4.30. Auger depth profile of a Pt contaminated bronze sample (376A#10). The crystal was subjected to cathodic and low anodic potentials while in a solution which contained dissolved Pt. The Pt was dissolved from a large Pt foil during cyclic voltammetry studies on the Pt foil

of Remeika et al. (61). Remeika and coworkers were able to raise the superconducting transition temperatures of powders of these crystals by etching them in acid solutions at 100°C. The etching process was shown to reduce the alkali content in the powders by a factor of 1/3 to 1/2. However, the cyclic voltammetry results on single crystals show that the surfaces of these crystals are subject to anodic corrosion, and that as a depletion layer is created, this layer also dissolves at high anodic potentials. So this combination of results, some contradictory, imply that the surface layers on anodized hexagonal tungsten bronzes are either only partially depleted of metal atoms, or that the depletion layer is rather thin, on the order ot 100 Å or less.

Linear Sweep Cyclic Voltammetry

Important electrochemical information about the bronze surface was obtained by using the technique known as linear sweep cyclic voltammetry. The electrochemical properties were found to depend both on the crystal structure and the alkali metal of an alkali tungsten bronze. Two electrochemical processes were studied by this technique. These processes were the anodic dissolution of the bronzes, and the formation of hydrogen tungsten bronzes on their surfaces at certain potentials. The cubic sodium tungsten bronze has been studied for both of these reactions (13, 56, 60), but little or no data has been reported for the other tungsten bronzes. Several questions still remain concerning the hydrogen bronze formation on cubic Na_xWO_3, and the crystal structure of the sodium depletion layer on this compound. Even though hydrogen

bronze formation has been studied on cubic Na_xWO_3, the x-value of the resulting hydrogen bronze (H_xWO_3) has not been determined. Since the x-value is unknown, the electronic state of the surface (semiconducting or metallic) is also unknown. Therefore, cyclic voltammetry (CV) curves for cubic and tetragonal Na_xWO_3, cubic and tetragonal Li_xWO_3, monoclinic $Na_{0.02}WO_3$, and hexagonal thallium, potassium, and rubidium tungsten bronzes were obtained and will be presented here.

The CV curve for an anodized $Na_{0.9}WO_3$ crystal is shown in Figure 4.31. This same curve was reported by Randin et al. in a comprehensive study of the surface properties of cubic Na_xWO_3 (13). The large peaks centered around 0.15 V were shown to be due to charge transfer for the formation of hydrogen tungsten bronze and its reverse reaction:

$$xH^+ + WO_3 + xe^- \rightleftarrows H_xWO_3 \qquad 4.1$$

The potentials at which the peak currents occur approach a difference of 60 mV as the sweep rate approaches zero. This behavior is typical of a reversible, but diffusion-limited reaction (39, 40). For a diffusion limited reaction, the peak current i_p should be proportional to the square root of the sweep rate S. However, for the curves shown in Figure 4.31, i_p is not proportional to $S^{\frac{1}{2}}$, but is almost proportional to S. If i_p is proportional to S, a surface reaction is occurring, which is limited only by the activation energy for the reaction, and the surface coverage fraction θ (43, 44).

Randin and coworkers were able to show that a surface reaction (reaction 4.1) was occurring, but that it was limited by diffusion in

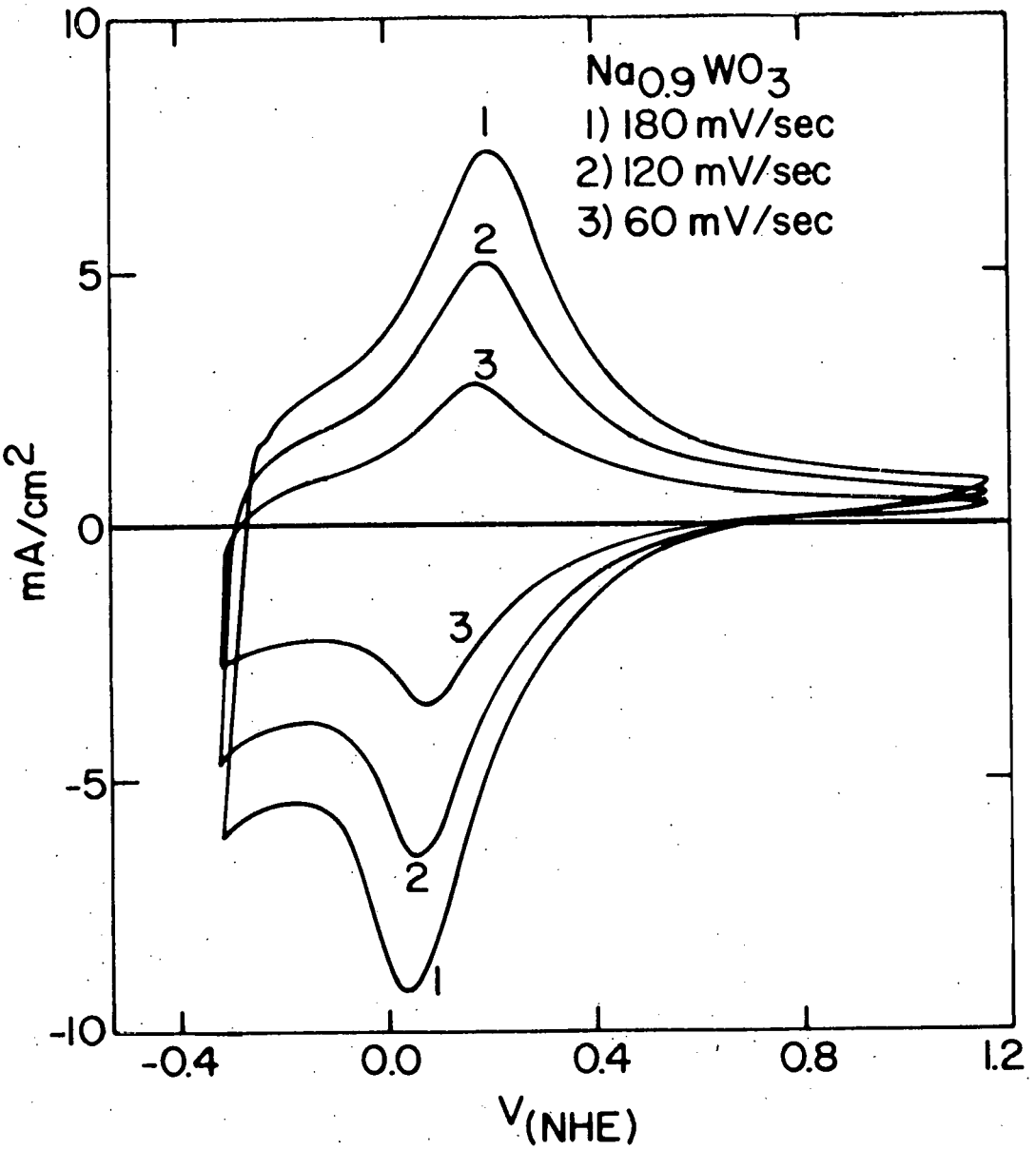

Figure 4.31. CV curves for an anodized cubic sodium tungsten bronze. The redox reaction at 0.15 V is the formation of hydrogen tungsten bronze in the sodium depletion layer. The reaction is reversible and the surface undergoes no net change. No anodic corrosion currents were observed at anodic potentials up to 2.0 V

the solid state. Hydrogen atoms (or ions) are the diffusing particles, moving through the crystal to fill the empty sodium sites. All cubic Na_xWO_3 crystals which had a significant sodium depletion layer exhibited the CV curve shown in this figure. Cubic crystals with x-values ranging from 0.6 to 0.9 were examined.

Freshly polished crystals of cubic Na_xWO_3 have CV curves of the same form as those for anodized crystals, but the peak currents are an order of magnitude smaller at similar sweep rates. The CV curve for such a crystal is shown in Figure 4.32. These curves are further evidence that the large current peaks, centered around 0.15 V, are due to reaction 4.1, because a hydrogen bronze can be formed at 0.15 V only if empty sodium sites are available for the hydrogen atoms to occupy. Some sodium is probably lost from the surface just by etching from the acid, and by the CV experiment itself when potentials above 1 V are reached on the CV trace. The amount of sodium depleted by these processes is much smaller than the amount of sodium lost by anodizing the crystal to 5 or 10 volts, and the differences in the current peak heights in Figures 4.31 and 4.32 are obvious.

On both anodized and unanodized crystals, the current approaches zero as the potential approaches more positive values. Extended potential scans out to 2.0 V show that no reactions occur in this potential region, or more specifically the cubic Na_xWO_3 surface does not dissolve at these high potentials. Also, the integrated current on the positive going scan equals the integrated current on the reverse scan. This equality implies that a totally reversible reaction is occurring,

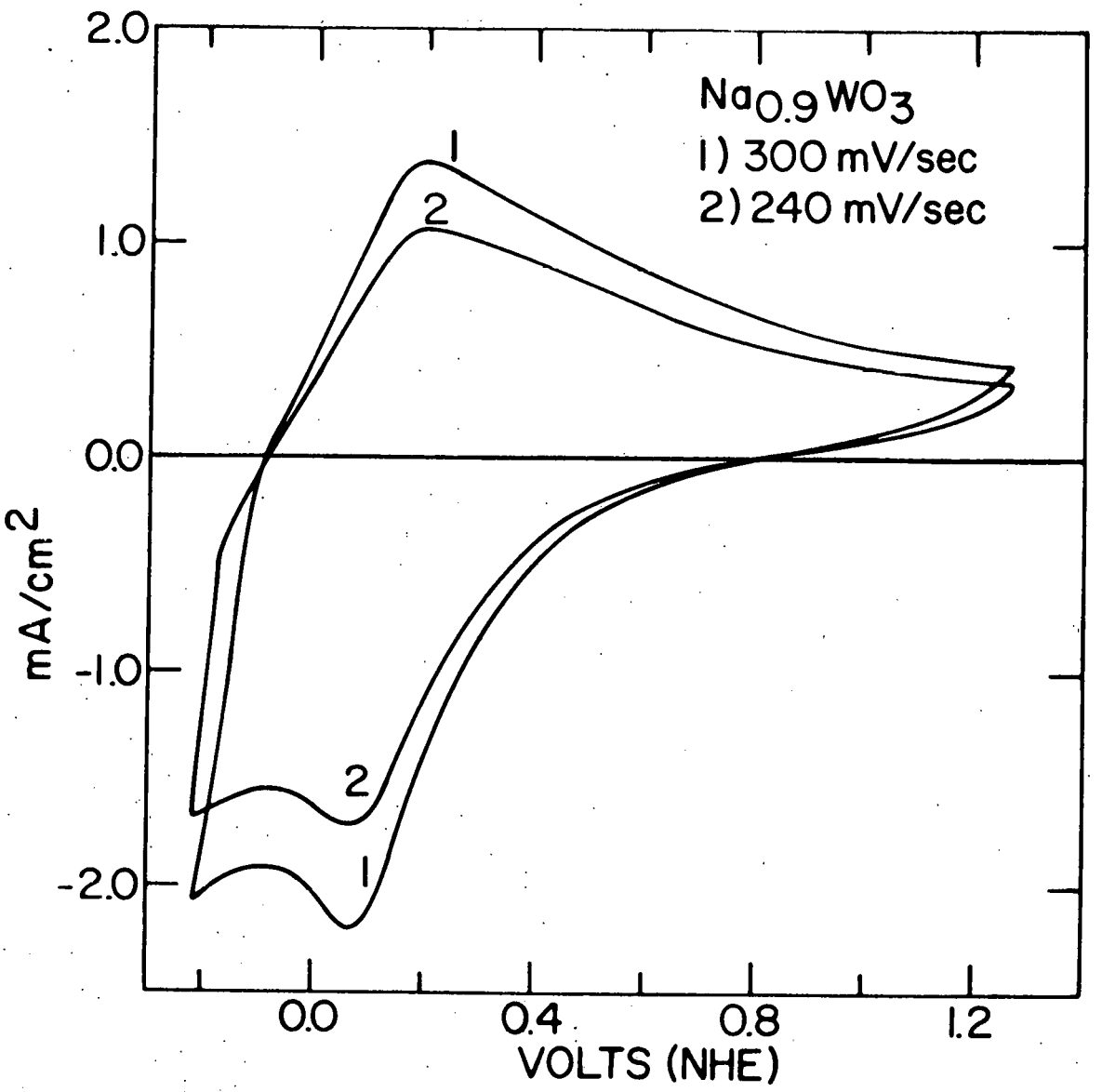

Figure 4.32. CV curve for a freshly polished cubic sodium tungsten bronze crystal. The peak currents are an order of magnitude lower than those on an anodized crystal, because hydrogen occupies only the vacant sodium sites

with no net change of the bronze surface. However, the first scans on all freshly polished crystals exhibited a corrosion current above 1.2 V, which disappeared after several voltage cycles. An example of a first CV scan is shown in Figure 4.33. The corrosion reaction above 1.2 V is probably the removal of sodium atoms from the first few layers of unit cells near the crystal surface. The first few CV traces on some crystals did not have well-defined peaks, but only broad current maxima. A broadened current peak implies a hindered reaction. One explanation of the broadening is simply a dirty surface, but the curve shown in Figure 4.33 was consistently observed on samples obtained from a large crystal with an x-value of 0.75. On most samples, the peaks sharpened up after several voltage scans. The reason for the difference is unknown. After a strong anodization (5 V or greater), all cubic sodium tungsten bronzes exhibited the curve shown in Figure 4.31.

The hydrogen bronze formation peak (cathodic current peak) in Figure 4.33 is only a shoulder on a larger background current, which introduces the question of the origin of this background current. One possibility was hydrogen evolution, but the high overvoltages on the hydrogen Tafel plot (Figure 4.30) show that this background current cannot be hydrogen evolution. The extended cyclic voltammetry scan in Figure 4.34 shows this to be the case. Hydrogen evolution does not begin until around -0.6 V, and a second reaction is occurring, with a broad peak around -0.3 V. This second reaction could be greatly enhanced by first holding the crystal at a lower potential than -0.3 V for several hours. The effect of reducing a crystal at -0.7 V for 3

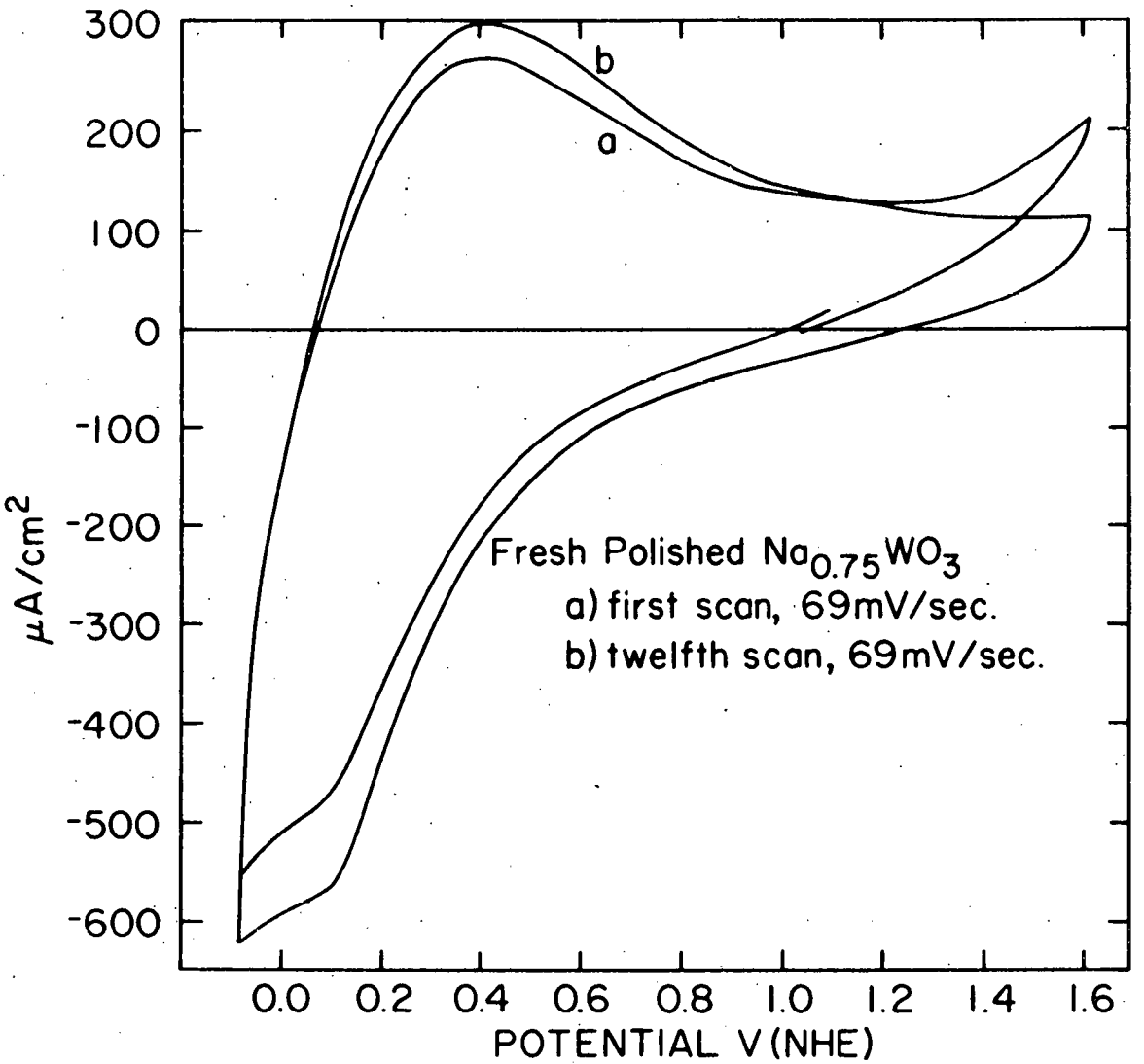

Figure 4.33. First and twelfth CV scans on a freshly polished sodium tungsten bronze crystal. Some sodium is removed at potentials above 1.2 V on the first few scans

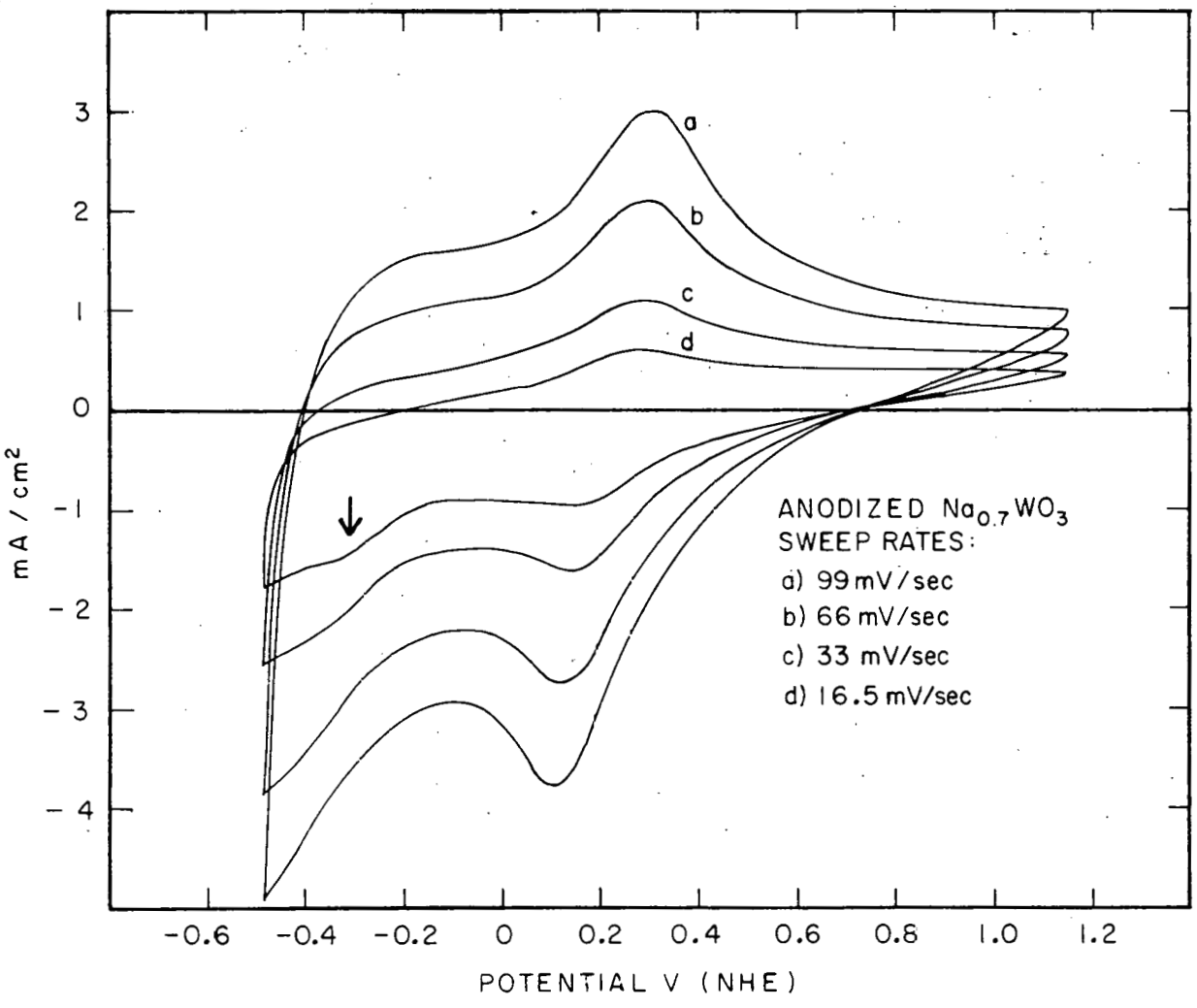

Figure 4.34. CV scans over an extended range of potentials. A second reaction is observed near -0.3 V. The reaction near 0.15 V is unaffected by the extended scan. Both reactions are shown to be due to hydrogen bronze formation

hours is shown in Figure 4.35. (This crystal had been anodized to 2 V in a previous experiment.) Marked changes in the CV curve show that the reduction process has changed some physical property of the bronze surface. The positive current peak at -0.3 V is now much larger than the peak at +.15 V. Anodizing the crystal did not restore the crystal to its original state, that is, the reduction process caused irreversible changes to occur on the crystal surface. This conclusion was reached by examining the CV curves taken after anodizing the crystal to 7 V, and these curves are shown in Figure 4.36. The anodization process increased the peak heights at 0.15 V as usual, but the reaction at -0.3 V still remains.

The top halves of the curves shown in Figure 4.36 are almost identical to the curves obtained by Vondrak and Balej in their study of hydrogen absorbtion by sodium tungsten bronzes (60). Contrary to Randin (13), and to the conclusions reached here, they did not attribute the current peak at 0.15 V to hydrogen bronze formation, but attributed only the peak at -0.3 V to that process. All researchers agree that a strong reduction of a sodium tungsten bronze crystal results in a severe blistering or cracking of the crystal surface. Such stresses must be associated with changes in the crystallographic properties of the crystal and are obviously irreversible. SEM photographs of such a surface were shown in Figures 4.23 and 4.24. The CV curves in Figure 4.36 indicated that the stresses on the crystal have caused a permanent change in the crystal which allows more hydrogen to enter the crystal at -0.3 V. In their study of hydrogen absorption in the bronze, Vondrak

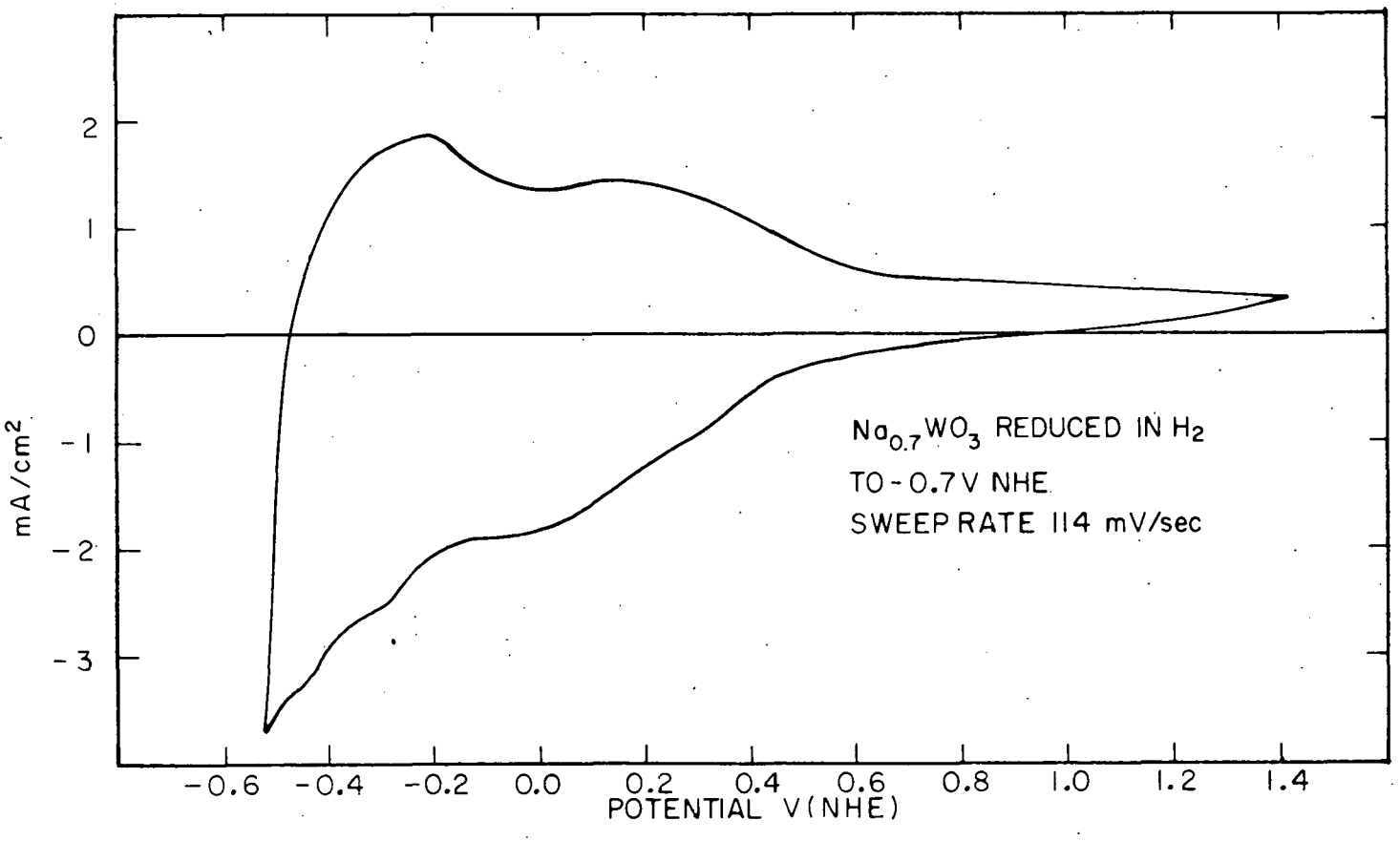

Figure 4.35. CV curve for a strongly reduced cubic sodium tungsten bronze. The reduction process in some way changed the crystal surface, allowing more hydrogen to enter the crystal at -0.3 V. The integrated anodic and cathodic currents are equal, implying that the reactions are still completely reversible

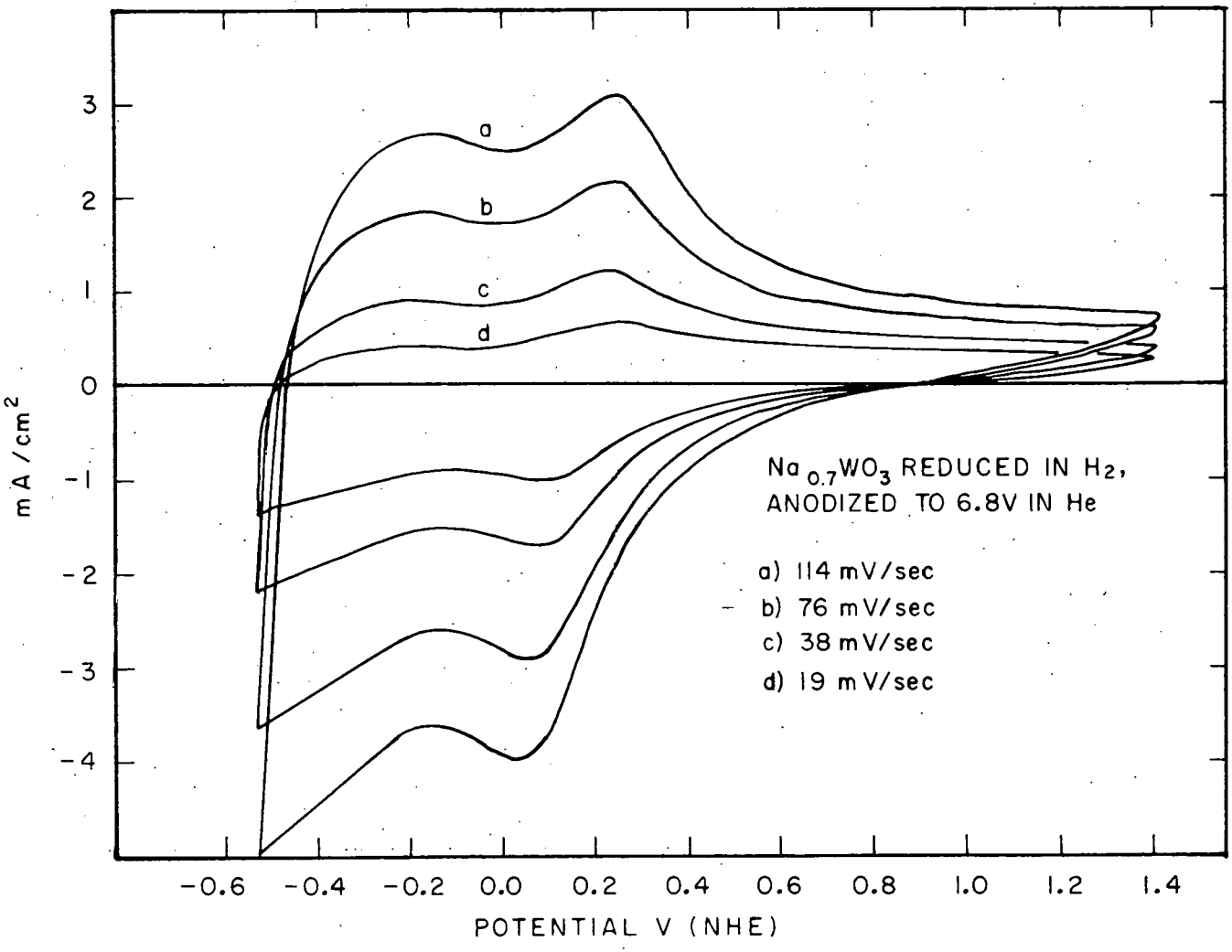

Figure 4.36. CV curves for the reduced crystal after it was anodized to 6.8 V. The anodization process increased the peak currents at 0.15 V as usual, but did not greatly affect the reaction at -0.3 V. The reduction process irreversibly changed the crystal surface

and Balej (60) studied freshly polished crystals with x-values of 0.3 to 0.9. From their results, they calculated that all empty sodium sites were filled with hydrogen when the crystal was held at -0.80 V. Cracks which appeared on the crystal surface were probably caused by the stresses which accompanied the filling of the lattice with hydrogen.

No results have been reported in the literature for hydrogen filling as a function of potential, or why there are two separate potentials associated with the formation of the hydrogen tungsten bronze on the Na_xWO_3 surface. Both of these questions can be answered from two observations that have been made. First, Siclet et al. studied the reduction of powdered WO_3 on a mercury electrode (62). By x-ray analysis of the powders, they found that orthorhombic $H_{0.1}WO_3$ was formed at potentials near +0.340 V, and that either the tetragonal I or cubic phase, corresponding to $0.33 \leq x \leq 0.5$, was formed at potentials near -.136 V. The resolution of their equipment was insufficient to give an exact x-value for the latter compound. The second clue to the nature of the two reactions on the surface of Na_xWO_3 is a simple visual observation made during CV scans on all the anodized cubic sodium tungsten bronzes. The normal color of this surface is a light green. As the electrode potential passes 0.15 V on the cathodic scan, the surface turns dark blue and highly absorbing in appearance. When the potential passes through the region of the current peak around -0.3 V, the surface turns a light red violet and highly reflecting in appearance.

Hydrogen tungsten bronzes have crystallographic and electrical properties similar to the other bronzes (15). The crystal structure is

cubic for $x > 0.50$, tetragonal I for $0.33 < x < 0.50$ and tetragonal II for $0.15 < x < 0.50$. The range of x values for the orthorhombic phase is not known, but is probably limited to low x values as it is for Na_xWO_3 (see Figure 1.4). Crystals of the orthorhombic and tetragonal II phases are semiconductors, and crystals of the tetragonal I and cubic phases exhibit metallic conductivities. So with the above observations on the color changes, and the results of Siclet et al., the two current peaks on the CV curves can be ascribed to the formation of the semiconducting and metallic phases of H_xWO_3.

The semiconducting transition may occur at a slightly different value than $x = 0.33$ if the sodium depleted region of cubic Na_xWO_3 is also cubic. A comparison of CV curves for several tungsten bronzes indicates that the surface layers on cubic Na_xWO_3 do retain the cubic structure. First of all, anodizing the cubic crystals changed only the current peak heights on the CV curves, but not their shapes. Cyclic voltammetry curves for tetragonal $Na_{0.45}WO_3$ and monoclinic WO_3 are shown in Figures 4.37 and 4.38. The current peaks which were so sharply defined on cubic Na_xWO_3 are much broadened, indicating that the electron transfer is slower and hindered by some repulsive interaction. The different crystal structure may hinder the diffusion of hydrogen through the crystal. Vondrak and Balej reported data that supports this hypothesis (60). Their current peaks at -0.3 V were an order of magnitude smaller for tetragonal $Na_{0.45}WO_3$ crystals than for cubic $Na_{0.5}WO_3$ crystals. Very slow cyclic voltage scans on monoclinic WO_3 are shown in Figure 4.39. On the two slowest scans, the two current peaks on both the anodic and

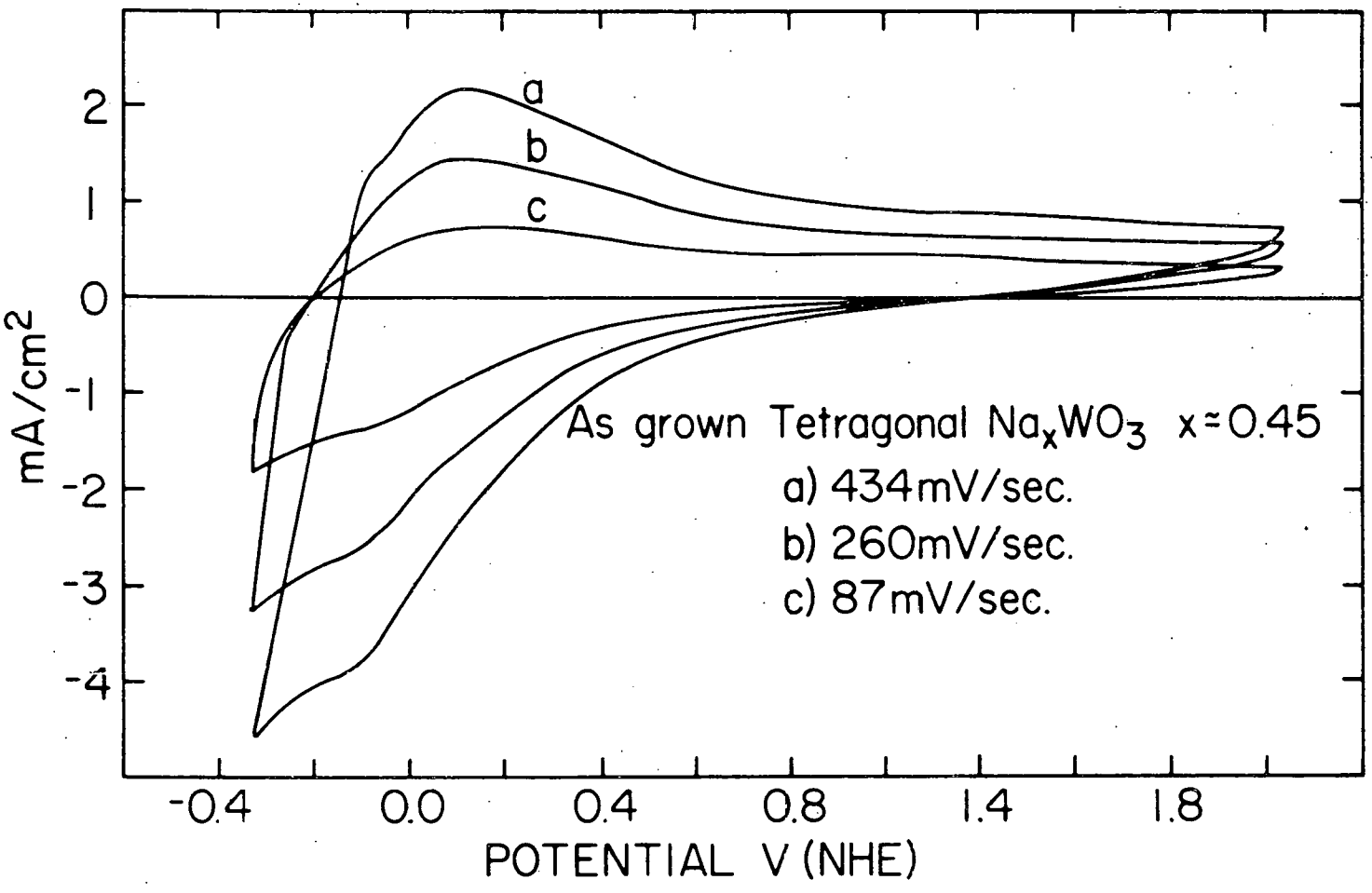

Figure 4.37. CV curve for a tetragonal sodium tungsten bronze. The current peaks associated with hydrogen bronze formation are smaller, broader, and shifted to more cathodic potentials, which means that the reaction is hindered

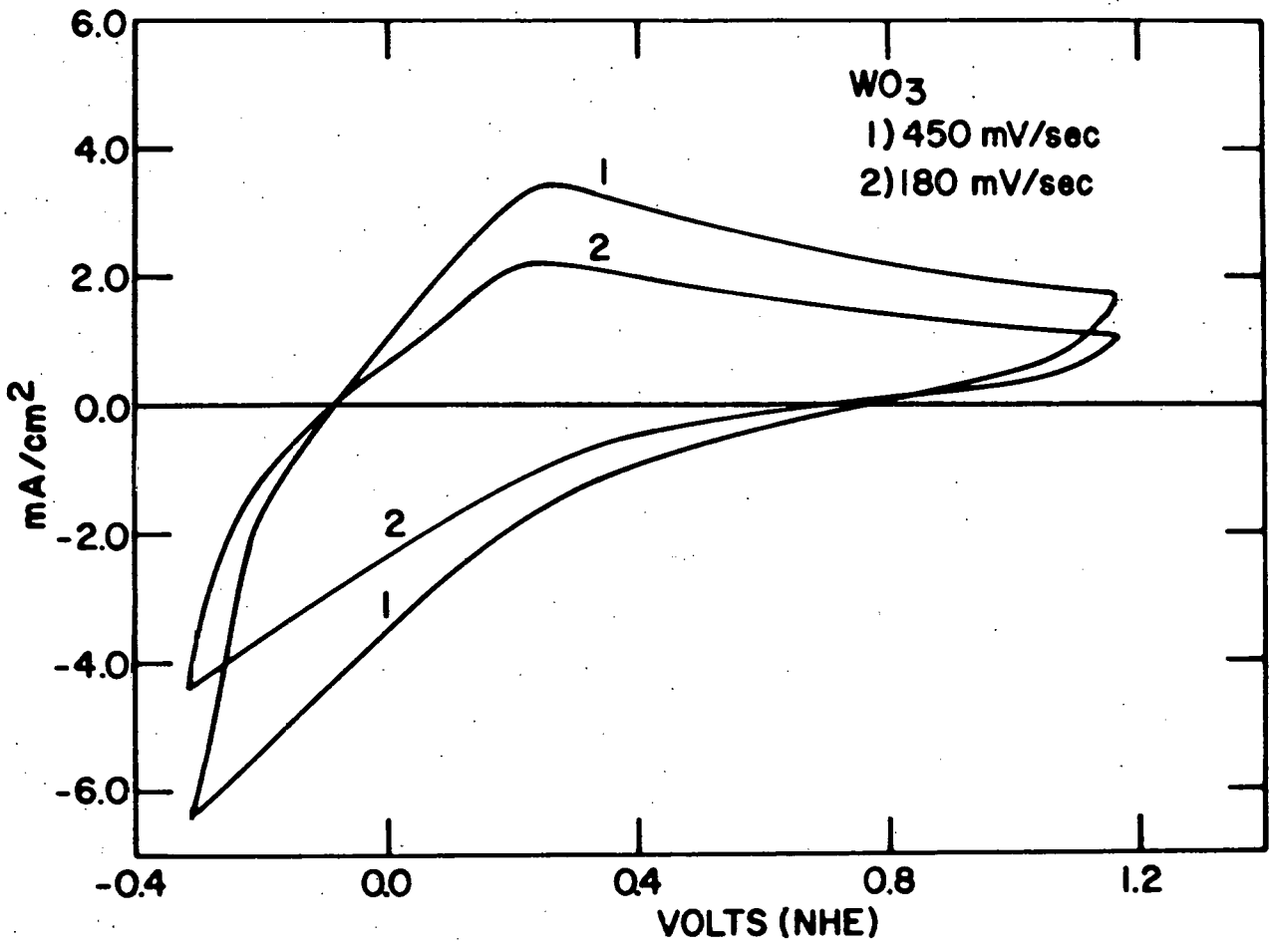

Figure 4.38. CV curves for a monoclinic $Na_{0.02}WO_3$ crystal. The hydrogen bronze formation peaks are completely broadened out, indicating that the reaction is hindered even more than on tetragonal Na_xWO_3

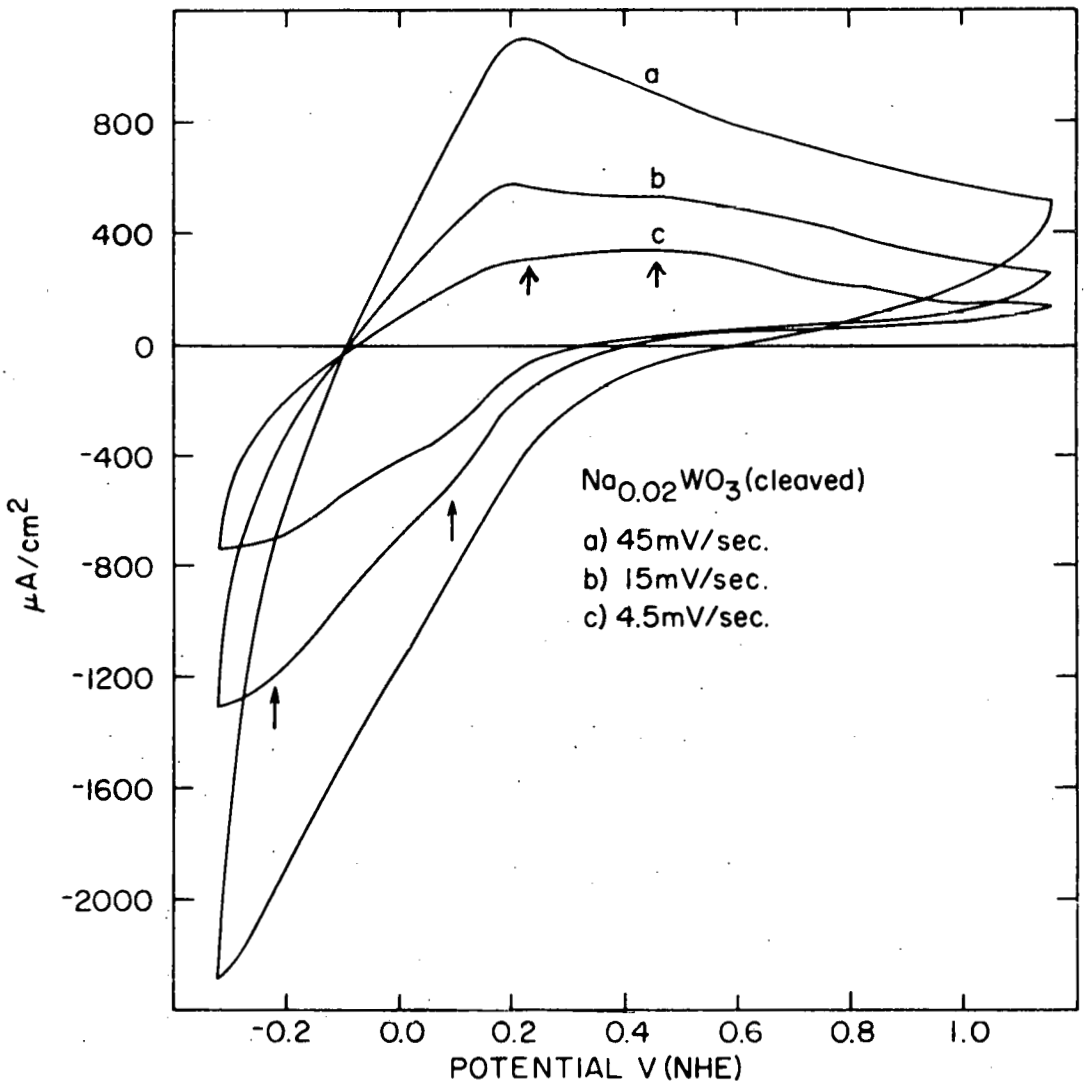

Figure 4.39. Slow CV scans on the $Na_{0.02}WO_3$ crystal. The two hydrogen bronze formation peaks can be identified on the two slowest scans. The anodic and cathodic peaks are separated by 400 mV for the reaction near -0.2 V and 300 mV for the reaction at 0.15 V

cathodic scans were very broad, but still discernible. The cathodic peaks occurred at roughly the same potentials as on cubic Na_xWO_3, but on the return scans the peaks were shifted to higher potentials. The anodic and cathodic current peaks for each reaction were separated by much more than 60 mV (300 and 400 mV), which indicates that a quasi-reversible reaction is occurring. The current peaks on anodized tetragonal Li_xWO_3 (Figure 4.40) were even further separated, showing almost irreversible behavior for the hydrogen bronze formation. The high potential of 1.2 V, needed to remove all of the hydrogen from the crystal, suggests that H_xWO_3 on the anodized, tetragonal lithium tungsten bronze surface may be stable in air or vacuum, and its properties studied by other techniques such as SIMS. There is no obvious reason why the anodized tetragonal lithium tungsten bronze should hold the hydrogen so firmly.

Analogous to the CV curves for cubic Na_xWO_3, the curves for cubic Li_xWO_3 have sharper, more well-defined peaks than the tetragonal Li_xWO_3. The CV curves for cubic $Li_{0.4}WO_3$ are shown in Figure 4.41.

Three tungsten bronzes with hexagonal crystal structures were examined by cyclic voltammetry, and despite their physical similarities such as crystal structure, lattice parameters, and electronic properties, they each displayed distinctly different CV curves. The three bronzes studied were $K_{0.32}WO_3$, $Rb_{0.3}WO_3$, and $Tl_{0.33}WO_3$. Potassium tungsten bronze is rather unstable in acid solutions, exhibiting large corrosion currents at potentials above 1.2 V. Reproducible CV curves could not be obtained with a freshly polished surface, so only the curve for an anodized surface is presented here. The CV trace is shown in Figure 4.42.

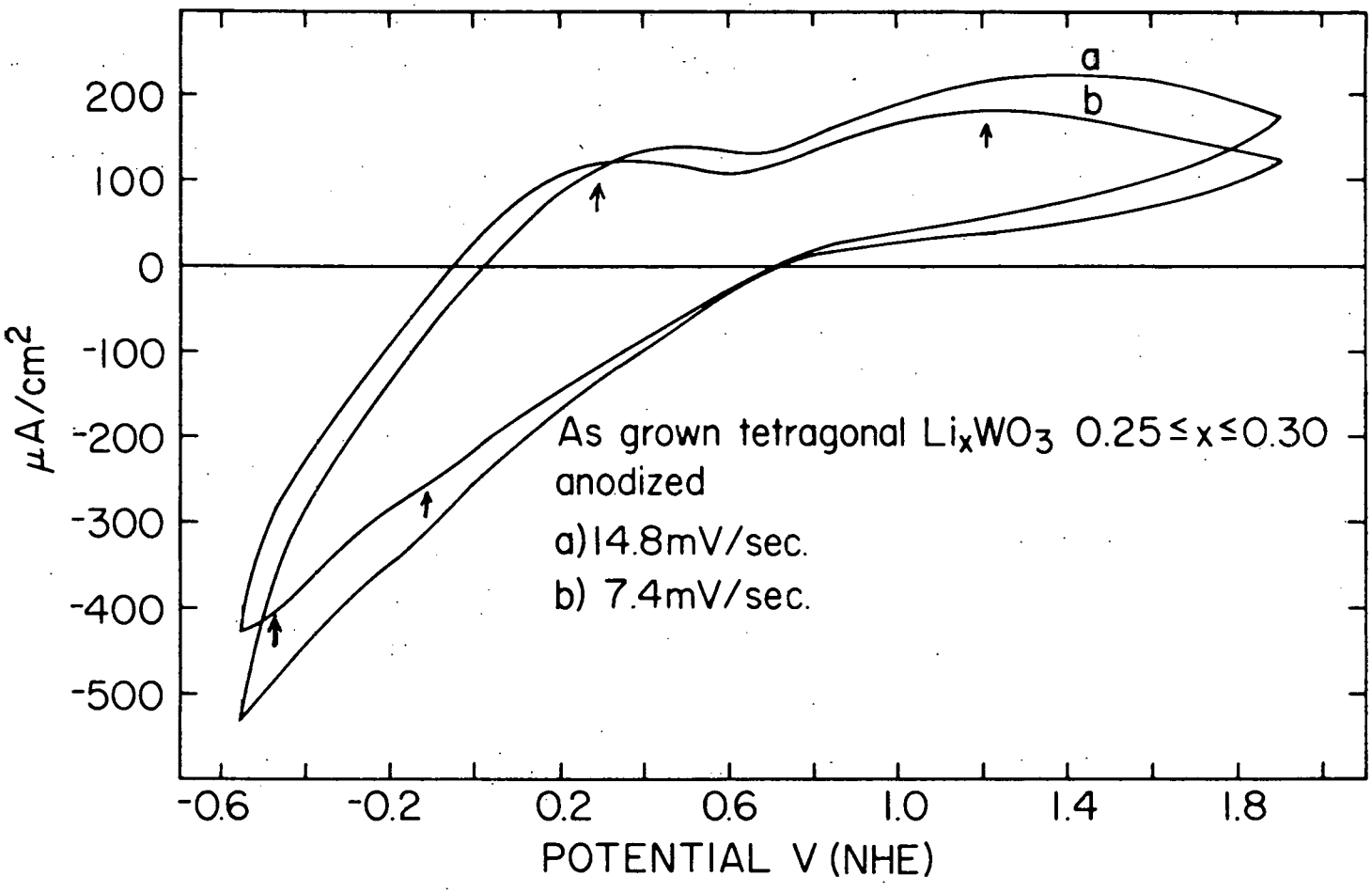

Figure 4.40. CV curves for an anodized tetragonal Li_xWO_3 crystal. The two hydrogen tungsten bronze formation peaks are visible, but the distinguishing feature of these curves is the wide (> 1.0 V) separation of the anodic and cathodic peaks. Before anodization, all the hydrogen was removed in the first peak at 0.30 V

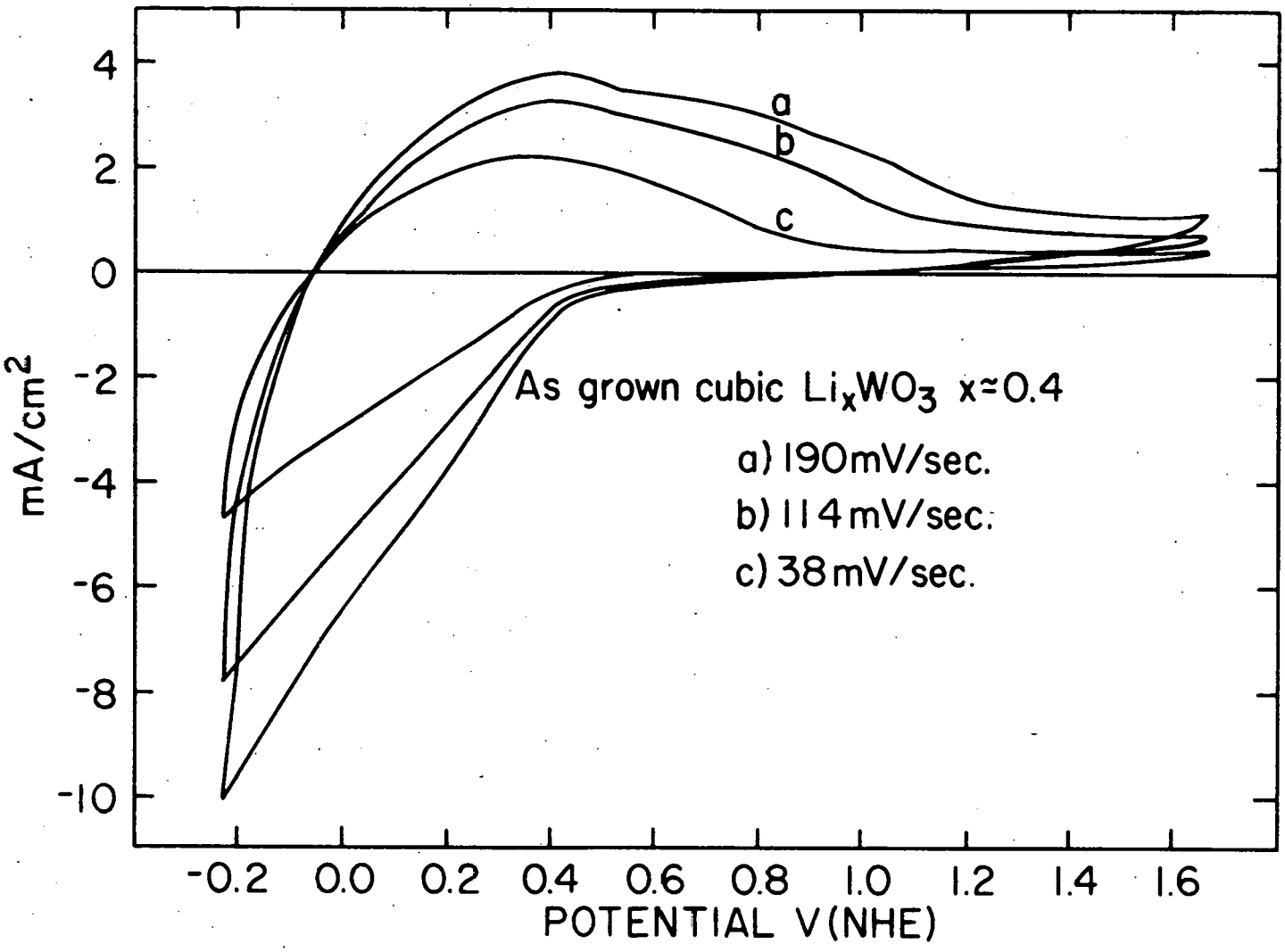

Figure 4.41. CV curves for a cubic Li_xWO_3 crystal. Analogous to cubic Na_xWO_3, the peaks on this cubic crystal are more well-defined than those on the tetragonal crystal

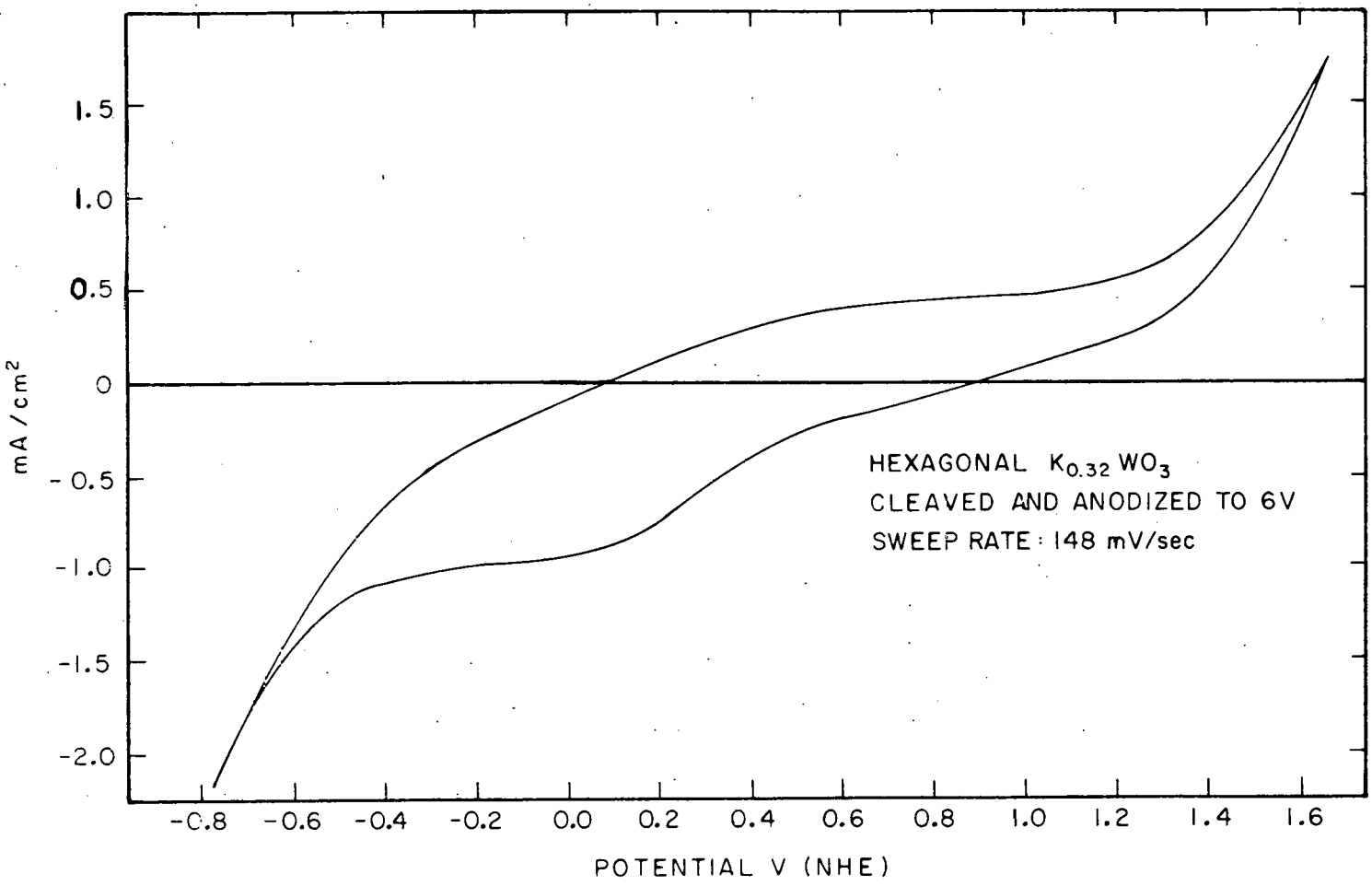

Figure 4.42. CV curve for hexagonal potassium tungsten bronze. The hydrogen tungsten bronze formation peaks are very flat, and widely separated in potential, so the reaction is nearly irreversible as on WO_3 and Li_xWO_3. Hydrogen evolution occurs at -0.6 V. The sharply rising anodic curve is not O_2 evolution, but dissolution of the crystal

Potassium tungsten bronze had a rest potential (in 0.1 N solutions) of -0.10 V and did not catalyze the oxygen reaction at all. Hydrogen tungsten bronze was formed on the surface of K_xWO_3, but the CV peaks were very flat and widely separated in potential, which indicates a nearly irreversible redox reaction. Hydrogen evolution occurred at -0.6 V.

The CV curves in Figures 4.43 and 4.44 show that hydrogen tungsten bronze is formed on the surfaces of freshly polished rubidium and thallium tungsten bronzes near -0.1 V. Both rubidium and thallium tungsten bronzes have better defined current peaks than potassium tungsten bronze. The peaks on the curves for $Rb_{0.3}WO_3$ are narrower than those on the cubic Na_xWO_3, indicating a fast, reversible reaction. The overall reaction is probably the same on all the bronzes, the reaction being the reversible formation of H_xWO_3 on the bronze surface (reaction 4.1).

Significant corrosion currents were observed at high anodic potentials on both rubidium and thallium bronzes. Anodization did not increase the magnitude of the current peaks for the rubidium tungsten bronze, but the current peaks were broadened. The current peaks for $Tl_{0.33}WO_3$ were broadened after anodization and doubled in magnitude.

These various CV curves for different crystals show that a bronze crystal with a certain alkali metal and crystal structure can be easily identified in most cases by its cyclic voltammetry curves. Two important conclusions can be drawn from this observation. First, in the case of cubic Na_xWO_3, the fact that anodized and nonanodized crystals have CV

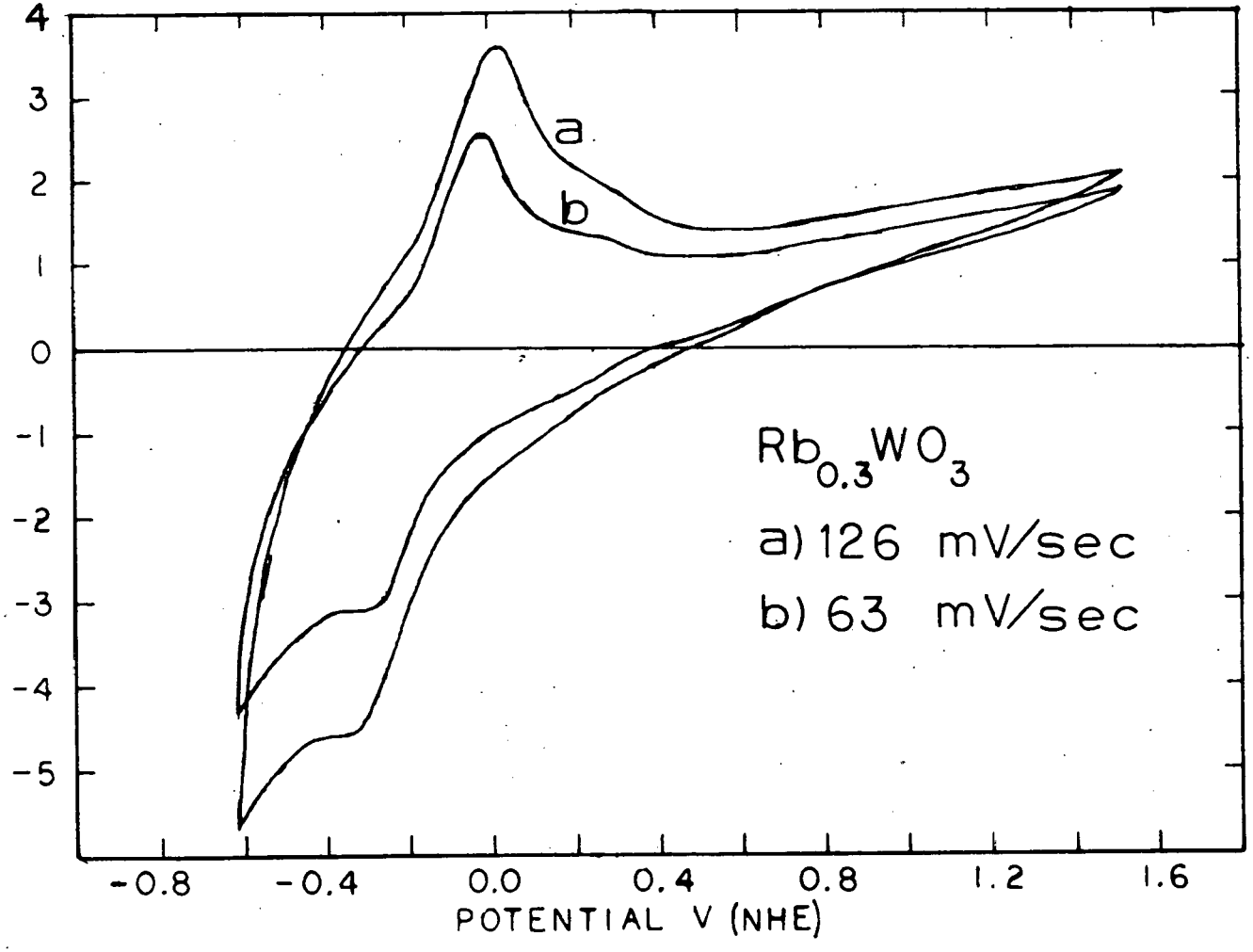

Figure 4.43. CV curves for hexagonal rubidium tungsten bronze with a fresh polished surface. A weak reaction occurs around 0.2 V and is only a shoulder on the dominant peak at -0.2 V. These two reactions are probably the same as on cubic Na_xWO_3. The increasing current at anodic potentials is due to corrosion

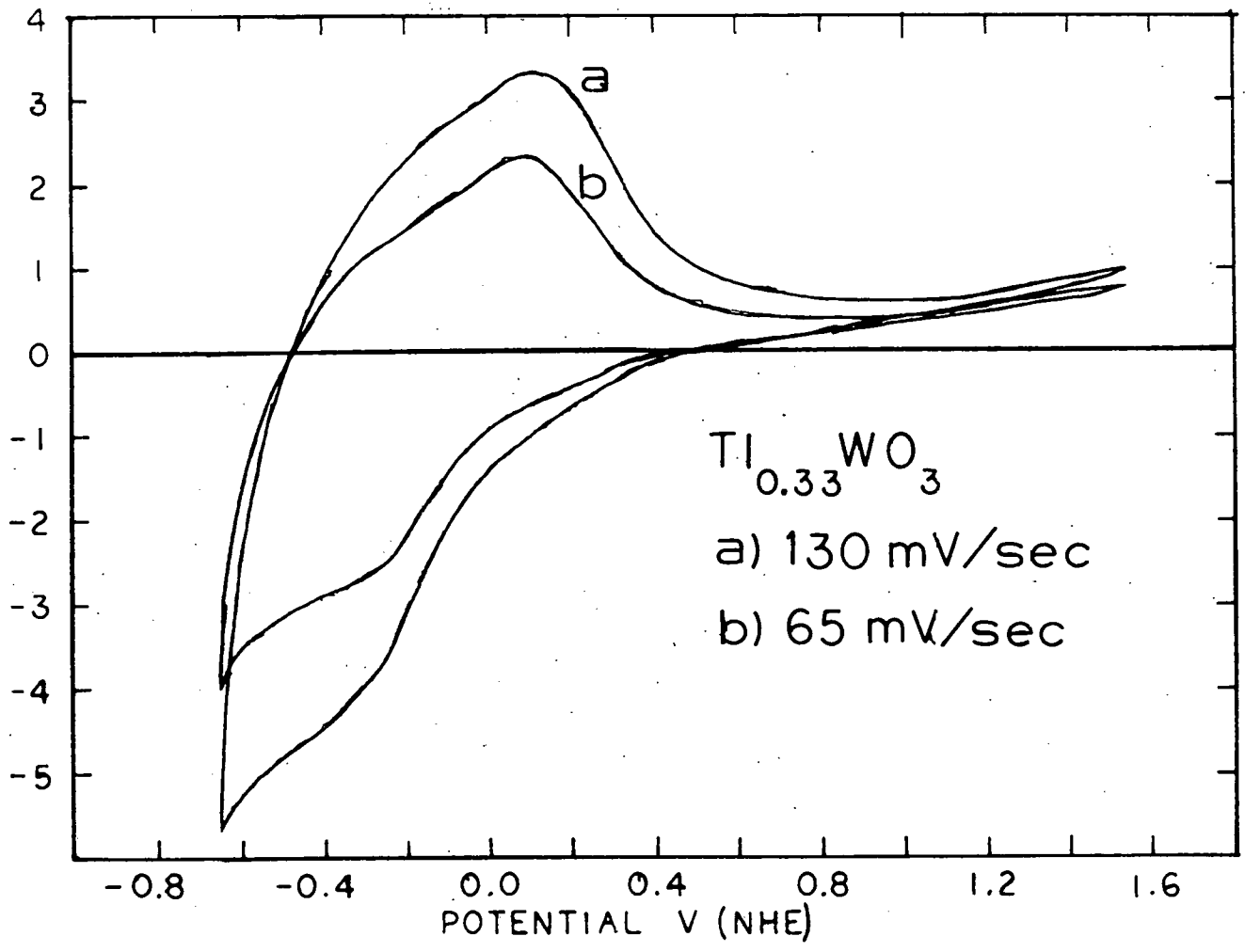

Figure 4.44. CV curves for hexagonal thalium tungsten bronze. Only one, broad reaction occurs on the cathodic scan and two broad peaks can be seen on the anodic scan. Slight anodic dissolution is indicated by the slowly rising currents at high potentials

curves of the same form, different from all other bronzes, implies that the sodium depletion layer does not collapse to a different crystal structure, but remains cubic. Second, the stability of a bronze surface in acid solution does not depend solely on the stability of the WO_6 octahedra of which the crystal is composed, but is dependent on the crystal structure and the alkali ion of that bronze crystal.

A very interesting bronze surface encountered in this study was the as-grown surface of a $Rb_{0.3}WO_3$ crystal. The CV curves for this surface are shown in Figure 4.45. At high anodic potentials, the current rapidly approaches zero, plus the integrated currents on the forward and reverse scans are equal. These characteristics imply that the surface is very stable to anodic dissolution. Hydrogen tungsten bronze was formed at -0.25 V and -0.35 V as indicated by the two well-defined current peaks at those potentials on the cathodic scans. The hydrogen was removed quickly and easily during the narrow current peak at -0.15 V on the anodic scan. These potentials were obtained by extrapolating to scan rate of zero mV/sec. After the crystal was anodized to 4 V, the peaks were broadened, but the peak heights were unchanged. The fact that the peak heights were unchanged implies that no rubidium depletion layer was formed by the anodization process. This crystal surface was the most stable surface studied of any of the bronze crystals.

Any chemically active surface constituent will reveal its presence on the electrode surface by some reaction peak on a CV curve. Platinum has a prominent cathodic peak between 0.6 and 0.7 V (see Figure 2.1) due to the reduction of a surface oxide. Metallic Pt on the surface of a

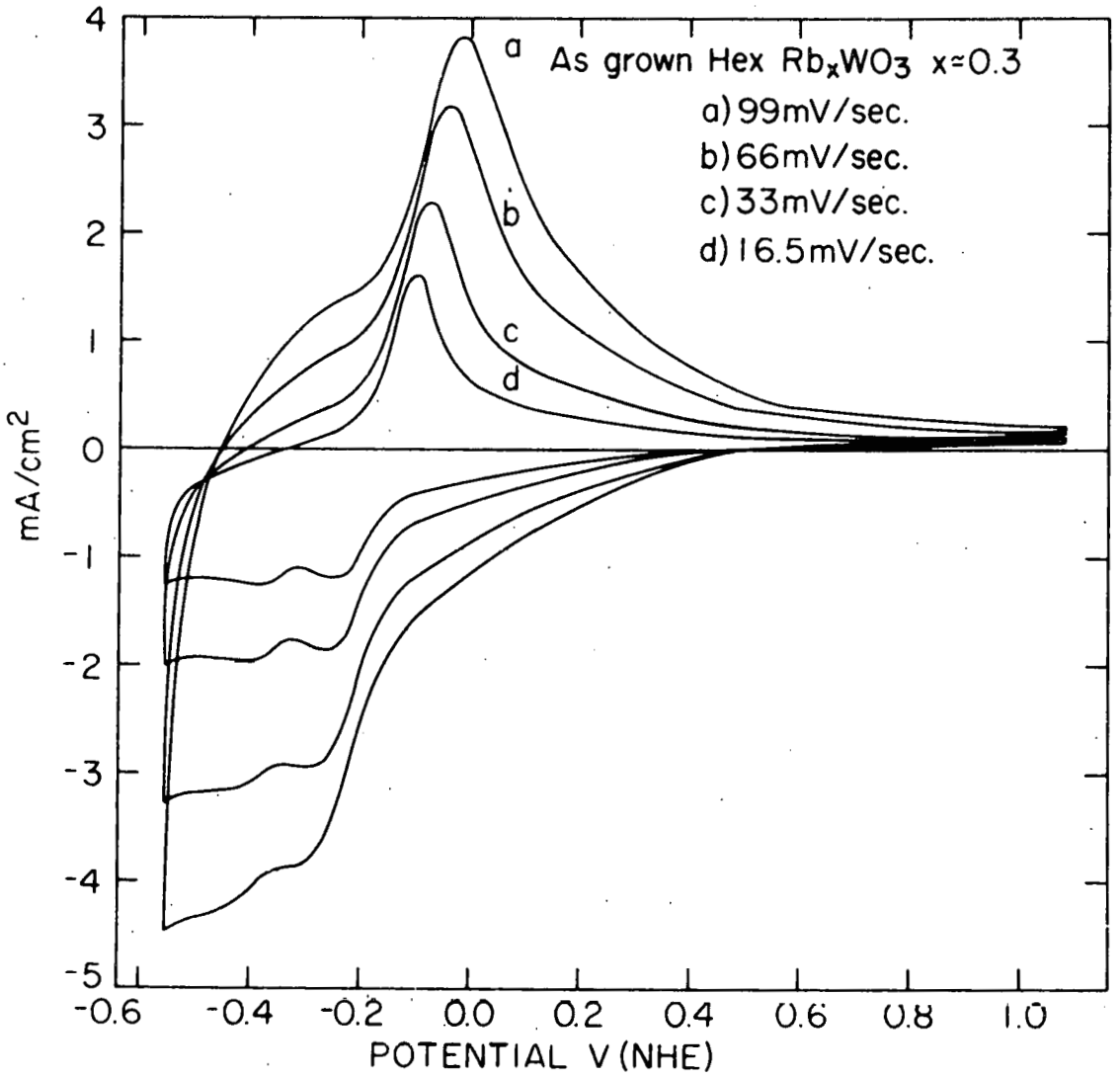

Figure 4.45. CV curves for an as-grown surface of a hexagonal rubidium tungsten bronze. The current approaches zero at high anodic potentials, and the integrated currents on the cathodic and anodic scans are equal, so the surface is quite stable. Hydrogen tungsten bronze is formed at -0.25 V and -0.4 V, and is removed in one reaction on the anodic scan

bronze can be detected by monitoring the CV scan in the stated potential region. CV curves for two Pt plated bronze crystals are shown in Figures 4.46 and 4.47, with an expanded current scale in the region of PtO formation and reduction. The presence of the Pt is also revealed by the hydrogen evolution reaction at -0.075 V. These two samples were studied in the same solution over the same range of potentials. Hydrogen evolution and hydrogen bronze formation occur at identical potentials on the two crystals, but the PtO peaks occur at different potentials, 200 mV apart. These two samples also had greatly different catalytic activities for the oxygen reaction (see Figure 4.9). The sample with the highest O_2 activity was the crystal with the smaller PtO peak, shown in Figure 4.46. In a earlier discussion of the Tafel results, Auger analysis and SEM photographs (summarized in Table 4.1), it was postulated that the Pt was present in different forms on the two crystals. The shift in the PtO reduction peak may perhaps be taken as additional evidence of different chemical states of the platinum. However if the PtO reduction peak shift is taken as evidence of such, the existence of Pt_xWO_3 on the surface must be excluded, because the SEM photographs revealed Pt particles on both surfaces (see Figures 4.19 and 4.20), and the PtO reduction peaks are undoubtedly associated with those Pt particles.

The discovery of more active forms of Pt for oxygen catalysis is a significant discovery, but the present work has only served to establish the existence of these different Pt forms on the bronze surface. The nature of the different forms of Pt on the bronze surface, and the role played by the bronze in the catalytic process, should be further

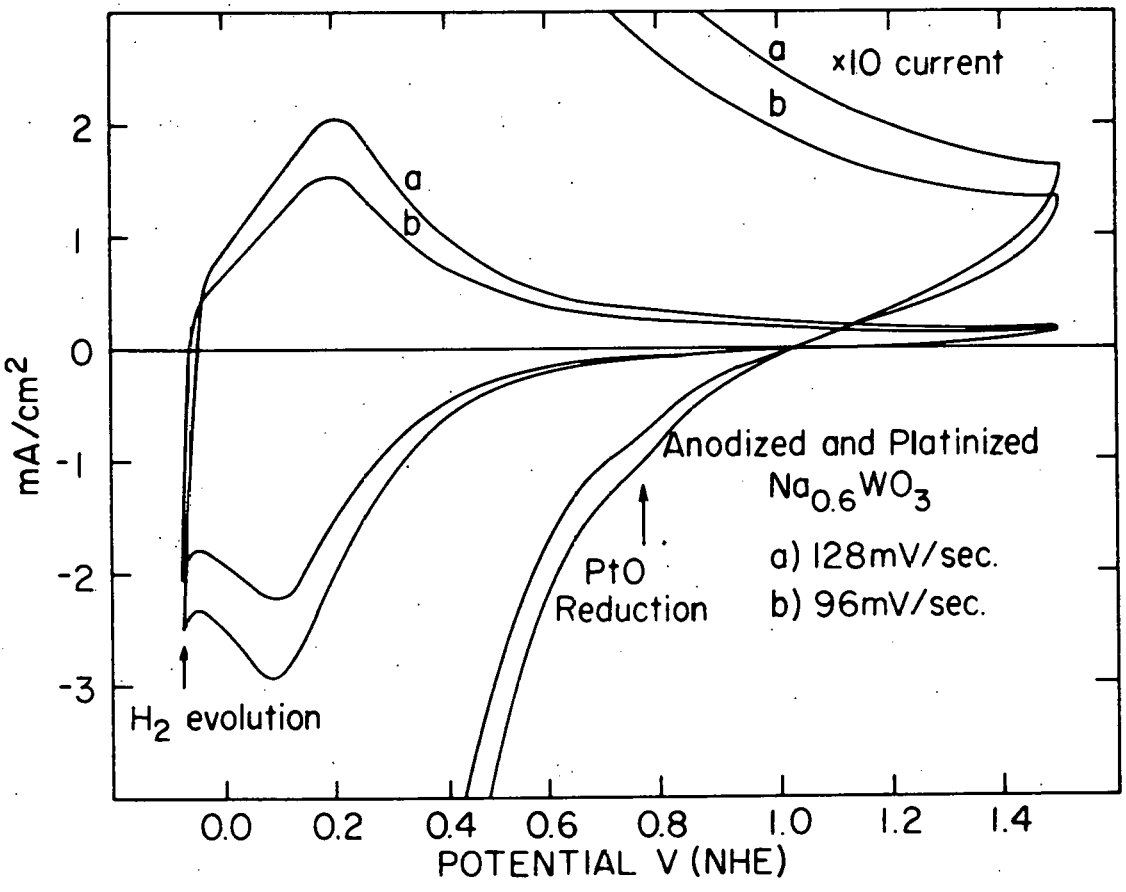

Figure 4.46. CV curves for a cubic Na_xWO_3 crystal (376B#2), plated in chloroplatinic acid at 0.040 V. Platinum is detected both by the PtO reduction peak (see Figure 2.1) near and hydrogen evolution near -0.075 V. The hydrogen bronze formation at 0.15 V is unaffected

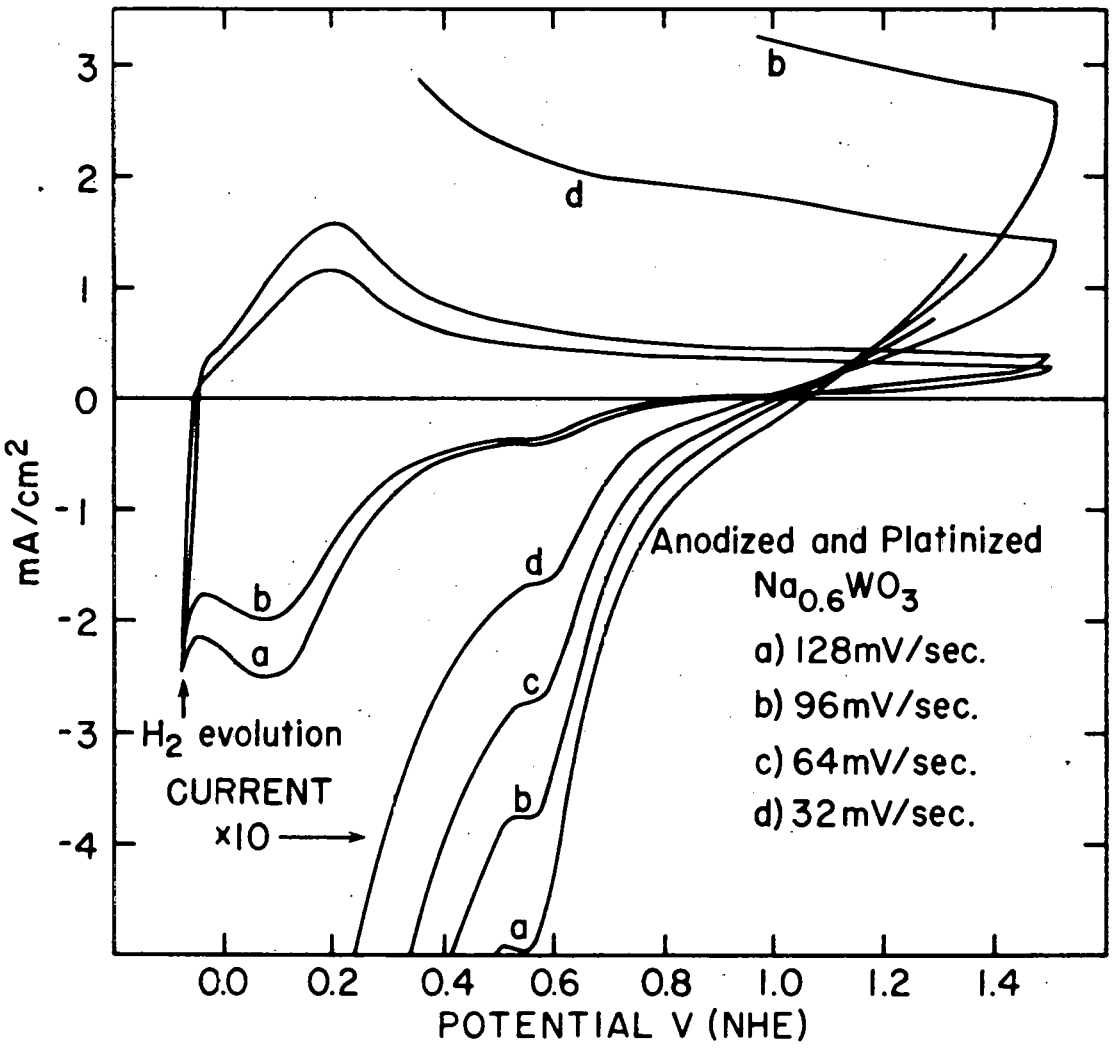

Figure 4.47. CV curves for a cubic Na_xWO_3 crystal (376B#1), plated in chloroplatinic acid at 0.120 V. The PtO reduction peak occurs 200 mV cathodic to the same peak on sample 376B#2

investigated. Perhaps then these differences in catalytic activity may be understood.

CHAPTER 5. SUMMARY AND CONCLUSIONS

Cubic sodium tungsten bronze was found to be a poor catalyst for the oxygen reaction, having an exchange current density of 10^{-14} A/cm^2, and a limiting current density of 4×10^{-5} A/cm^2. The Tafel slope was 110 mV/decade and the rest potentials were consistently near 0.5 V NHE. Tungsten trioxide and the other alkali tungsten bronzes, except potassium tungsten bronzes, had similar steady-state i-v characteristics. Potassium tungsten bronze did not catalyze the oxygen reaction at all. The similarities between the activities of WO_3, cubic Na_xWO_3, and the other alkali tungsten bronzes indicates that the activity is determined by the WO_6 octahedra, of which all the bronze crystals are constructed.

Doping the cubic Na_xWO_3 crystals, with up to 800 ppm of platinum, improved the i-v characteristics only at very low current densities ($i \leq 10^{-6}$ A/cm^2). When the platinum doped crystals were anodized so that the surface became a semiconducting oxide, the i-v characteristics were improved some more. The rest potentials were 50 mV higher, and the catalytic effect of Pt doping was increased to current densities of 4×10^{-6} A/cm^2. Previous results reported in the literature, claiming high catalytic activity for Pt doped sodium tungsten bronzes, were shown to be due to Pt contamination from the pre-electrolysis electrodes, and not to the Pt doping.

A large number of cubic Na_xWO_3 crystals were plated with Pt and tested as cathodes for oxygen reduction. Catalytic activities as high as that for pure platinum were obtained, but no synergistic effect was

found for the Pt-bronze system. However, several crystals plated with Pt by different methods had greatly different catalytic activities with the same amount of Pt on the surface. It was postulated that the Pt was deposited in different physical forms by the different plating methods, resulting in different catalytic activities. The formation of platinum tungsten bronze (Pt_xWO_3) on the sodium depleted surface is suggested as a possibility for one of these different forms of active platinum. If Pt_xWO_3 is not formed on the crystal surface, the role played by the oxide layer in activating the crystals as catalysts is still unknown. Previous anodic treatment of the samples was a prerequisite for the deposition of small amounts of Pt on the crystal surface in a finely dispersed form.

Anodized sodium tungsten bronzes were shown by Auger depth profiling to have a greatly depleted sodium content on the crystal surface. The sodium depletion layer was 1,500 Å thick for samples anodized to 9 V, with a sodium x-value of between 0.05 and 0.1. The cyclic voltammetry curves provide strong evidence that the sodium depletion layer on Na_xWO_3 retains the crystal structure of the bulk.

Hydrogen tungsten bronze is formed in the sodium depletion region of a sodium tungsten bronze crystal at low potentials. The hydrogen bronze is formed in two steps, one at 0.15 V and one at -0.3 V, corresponding to the formation of semiconducting and metallic hydrogen tungsten bronze. Hydrogen tungsten bronze was found to form at low potentials on the lithium tungsten bronzes and the three bronzes with hexagonal crystal structure also. The reaction occurred at slightly

different potentials on the different bronzes, but the overall reaction is still the reversible formation of H_xWO_3. Each tungsten bronze crystal exhibited a unique cyclic voltammetry curve, due to the different hydrogen bronze formation potentials, and different current peak shapes for that reaction.

The three bronzes with hexagonal crystal structures (rubidium, thalium, and potassium tungsten bronze) were found not to be as stable in acid solution as the other bronzes. In particular, large corrosion currents were observed on hexagonal potassium tungsten bronze above 1.2 V. No significant alkali depletion layers were found by the Auger analysis on these hexagonal bronze crystals. Apparently, when the alkali atoms are removed, the remaining hexagonal WO_3 structure is unstable towards anodic dissolution.

APPENDIX A. HIGH PURITY ELECTROCHEMICAL EXPERIMENTAL SYSTEM

Technical Details of the Still

The distillation unit is shown in Figure A.1. This apparatus consists mainly of quartz with Fischer and Porter teflon seals and stopcocks. The various valves and waste drains are of pyrex construction as is the acid flask and automatic burette. All other components are quartz. The boiling and receiving flasks are each seven liters in volume, large enough to allow for two or even three distillations of the first charge of water without opening the system to the atmosphere. Two separate charges may first be distilled to fill the receiving flask the first time. Repeated distillations are possible because the boiling flask may be drained without opening it to the atmosphere, rinsed, and refilled through a drain from the receiving flask. The entire system is always kept under a positive pressure ($\sim$ 4 cm of water) of high purity oxygen. Water used to fill the boiling flask should already be of the best "conductivity water" quality in order to prevent contamination of all parts of the still. (The term "conductivity water" arose from the work of earlier researchers who determined the conductivity of dilute electrolytic solutions.) The advantages of a quartz and teflon still are lost completely in redistilling ordinary tap distilled water. Feed water used in this still is taken from a Barnstead tin block "conductivity still" and has a specific conductivity of 5×10^{-7} $(\Omega\text{-cm})^{-1}$.

The first charge of water, 5 to 5½ liters, is held at low boil for 15-20 hours, while oxygen is bubbled through the still. After the slow

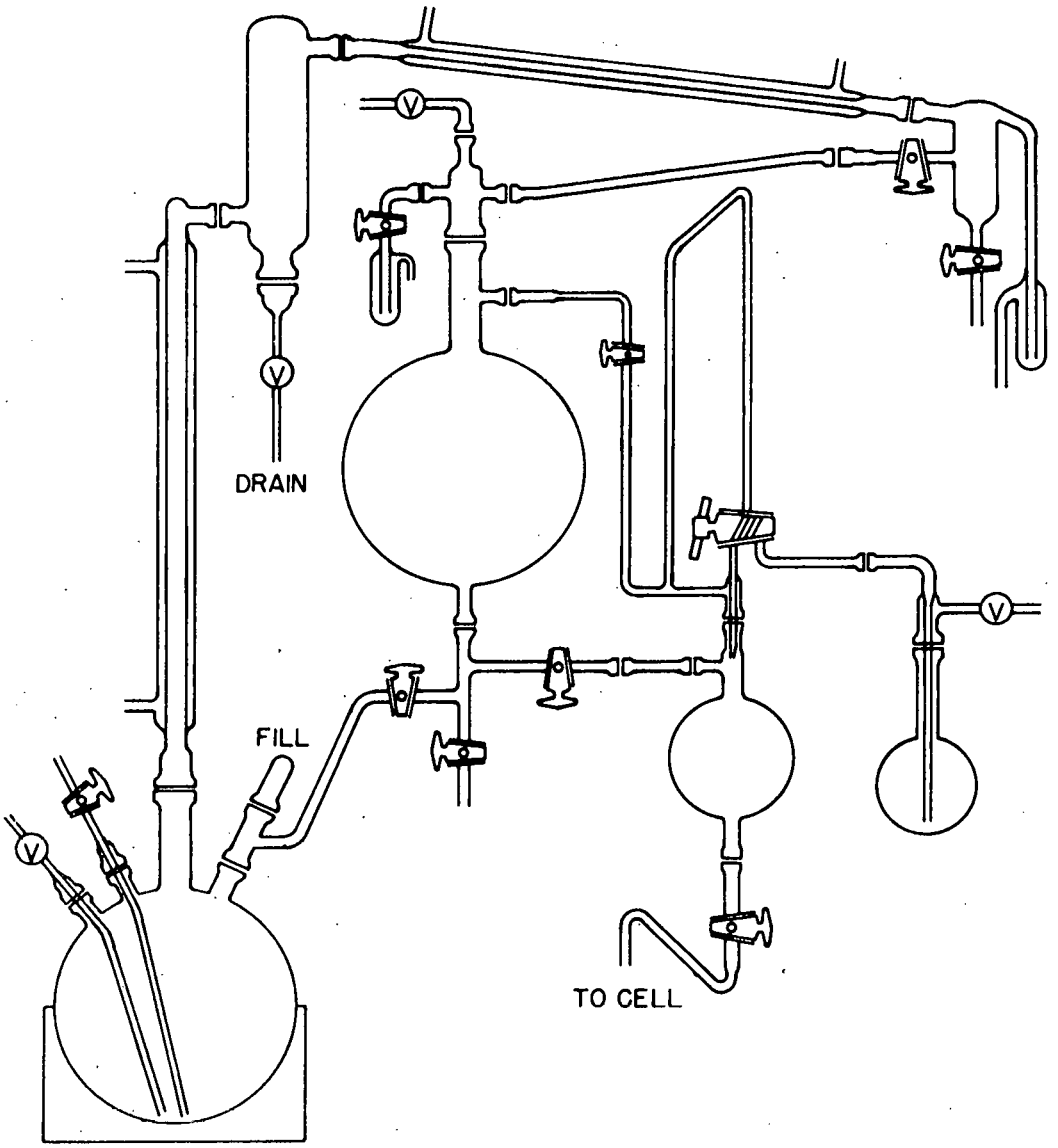

Figure A.1. Quartz and teflon still for in-situ distillation of high purity water. All stopcocks and water lines were also of quartz and teflon construction

boil, the water is brought to a vigorous boil to remove as many impurities as possible from both the water and the surfaces of system components further along the line. After 20 to 30 minutes of the hard boil, the secondary condenser is turned on and the stopcock on the stillhead is opened to the receiving flask. Condenser start up must be very slow to avoid the rapid condensation of steam and subsequent formation of a partial vacuum in the system. A partial vacuum will draw outside air and impurities into the system. The first condenser is a vertical refluxing condenser which is used only if a vigorous boil is desired for long periods of time without collecting any water. Normally the refluxing condenser is not used because some volatile impurities may be continually refluxed also.

An efficient spray trap must be used in any distillation process to prevent the carryover of tiny mist particles formed by bursting bubbles of steam in the boiling flask. On this still a quartz tube filled with crushed quartz chips effectively eliminates any mist carryover. The spray trap is between the two condensers. The top of the spray trap is fitted with a throat heater to eliminate the creep of soluble impurities along the otherwise moist surface into the final condenser and receiving flask. Eleven liters of water are first distilled in two separate distillations to fill the receiving flask with six liters of water. The boiling flask is then drained without being opened to the atmosphere, rinsed three times with a little water from the receiving flask and filled with the remaining water. The entire distillation procedure is then repeated, resulting in two or three liters of high purity water.

After distillation, the distilled water from the receiving flask is mixed with acid from the automatic burette in a separate one-liter quartz flask. The mixing flask drains directly into the main compartment of the electrochemical test cell.

The Electrochemical Test Cell

The complete cell is shown in Figure A.2. Except for the reference electrode compartment, the test cell is composed entirely of quartz and teflon. Three compartment cells are standard equipment for much of the electrochemical work done today. This cell is based on a standard design with several modifications for greater experimental flexibility and convenience. An important feature of this cell design is the teflon cell cap with teflon-to-glass tubing seals, shown in Figures A.3, A.4, and A.5. These tubing seals provide an excellent airtight seal with only fingertip tightening. The size 71/60 tapered cell cap and the seals were turned from solid teflon rods. Teflon (TFE fluorocarbon) machines beautifully with the correct tools, and is flexible, giving an airtight seal. The teflon cell cap can be made more compact than a 71/60 glass joint, resulting in a cell with less dead air space. Six 6 mm tubing seals are fitted on the top of the cap for solution inlet and electrode supports. Gas inlet and exit is made through the two side ports. For sample loading, the cell is opened at the 71/60 joint by slightly heating the teflon cap with a heat gun. Samples are loaded from beneath, the cell cap being clamped permanently in position. Gas lines are disconnected quickly at two "tapertite" Chemplast brand teflon tubing connectors.

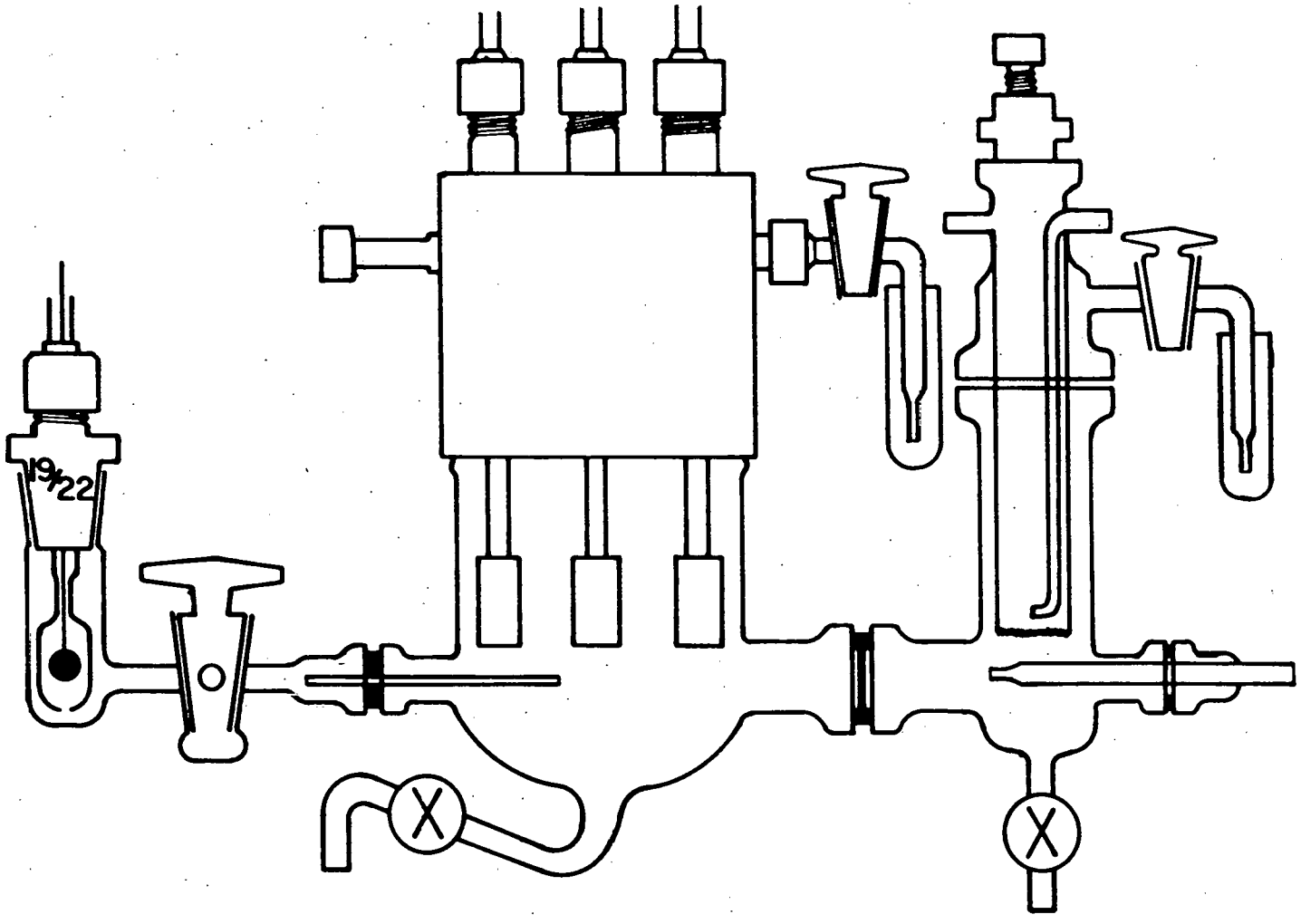

Figure A.2. Electrochemical test cell showing Pd-H reference electrode on the left and the double jacketed hydrogen counter electrode compartment on the right. The test compartment in the middle is a 71/60 quartz joint with a lathed teflon cap, and six (not all shown) teflon tubing seals

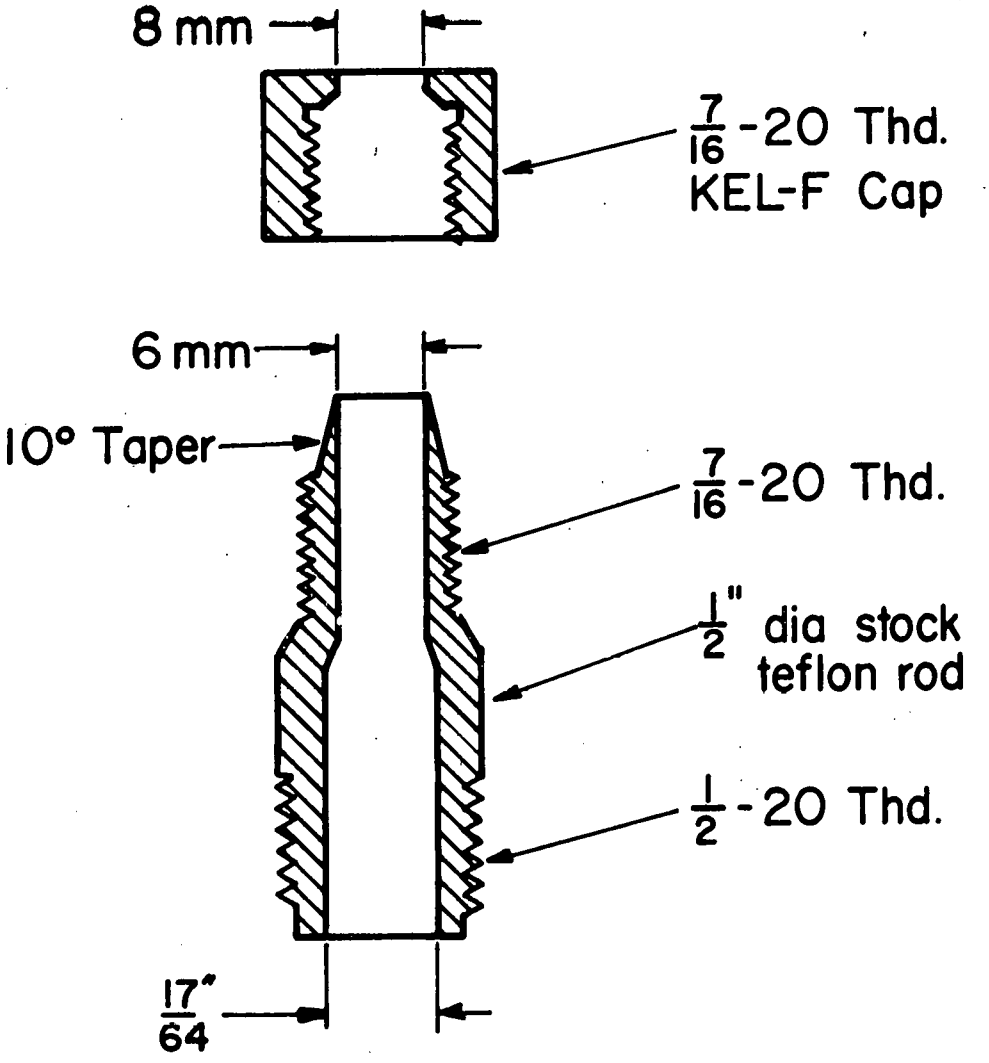

Figure A.3. Teflon to glass tubing seal. The cap and body were turned from KEL-F and teflon rods.

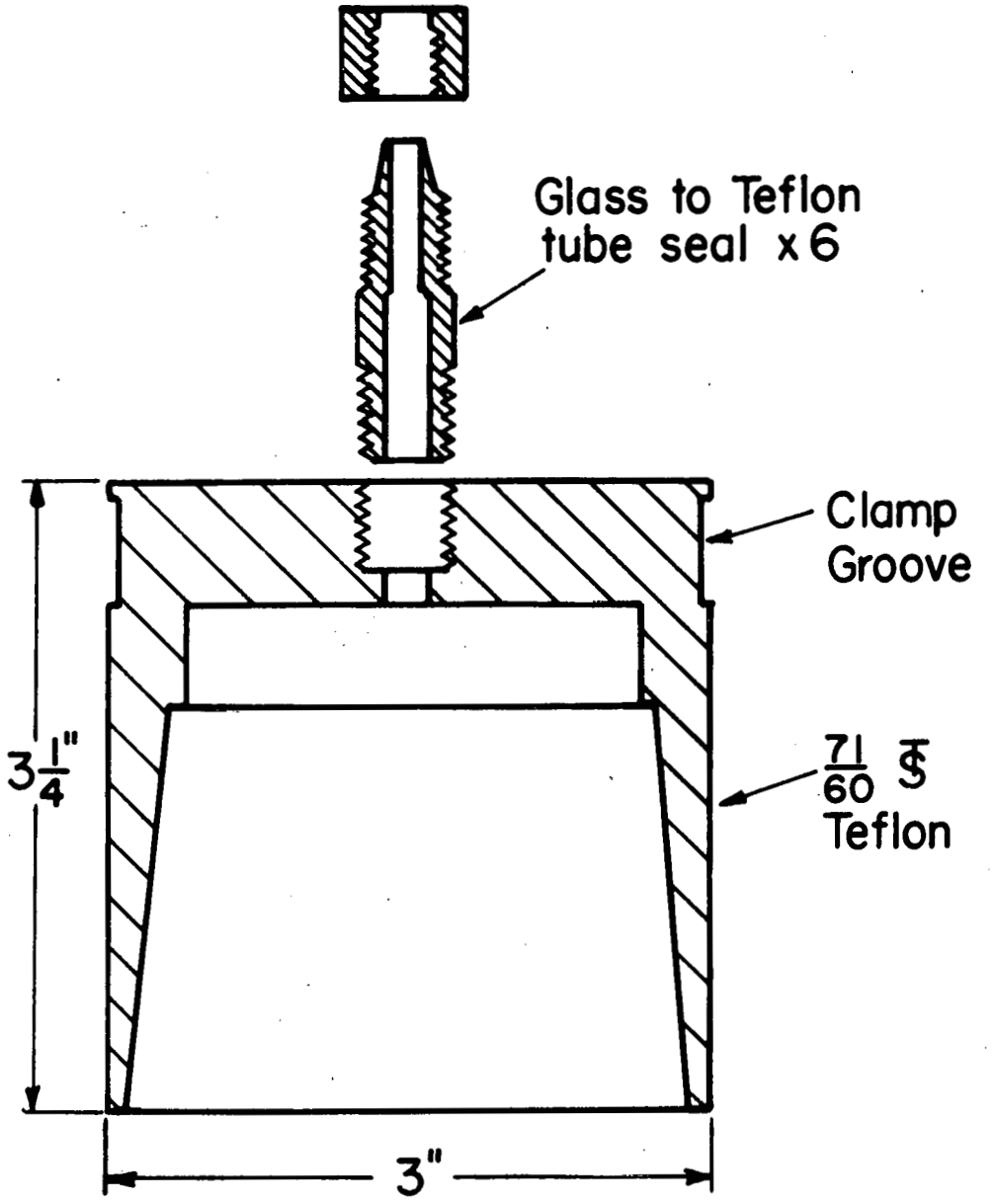

Figure A.4. Teflon cell cap with one tubing seal shown. The cap was turned from a solid 3 inch dia. Teflon rod

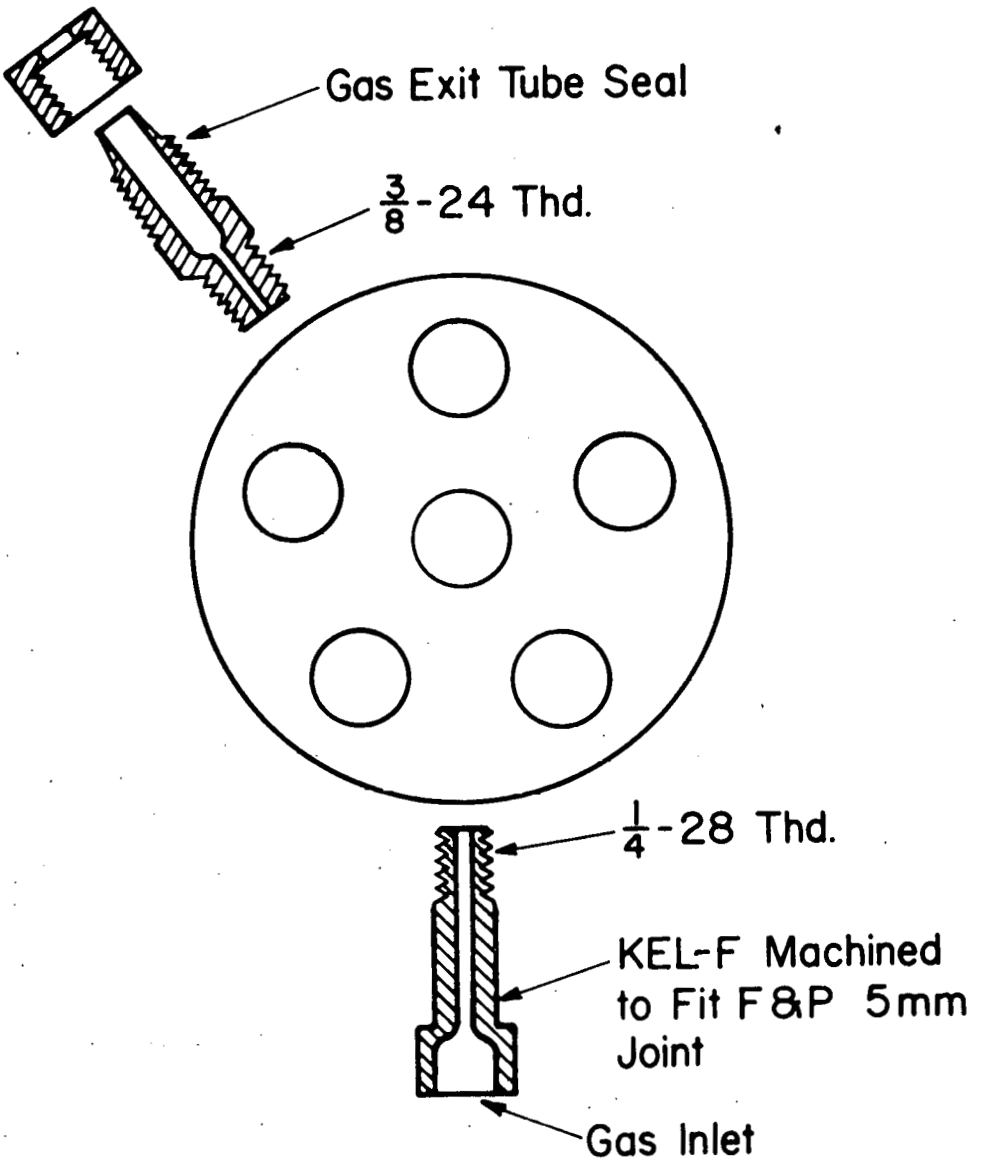

Figure A.5. Top view of the cell cap. The six holes are for the six tubing seals. Gas inlet and exit ports are on the side

The reference electrode compartment is separated from the main cell by a closed high vacuum stopcock and luggin capillary. Maintaining ultra high purity conditions required the use of a Pd-H reference electrode, shown in Figure A.6. The c.e. compartment, shown in Figure A.7, is separated from the main cell by a quartz fritted disc. The disc is contained in a machined teflon plug which replaces the F&P teflon seal. A gold foil of 20 cm^2 area, immersed in an H_2 saturated compartment, provides an inert auxillary or "counter" electrode. The hydrogen prevents gold dissolution when the c.e. is subjected to anodic potentials. Contamination of the main cell with hydrogen is prevented by isolating the c.e. in an inner c.e. compartment, shown in Figure A.8.

With the Fischer and Porter 9 mm and 15 mm quartz-teflon joints, the r.e. and c.e. compartments may be detached from the test compartment. This feature allows for easier cleaning of the cell, independent alterations of any one of the three compartments, and easy replacement of the luggin capillary and quartz fritted disc.

The main or test compartment of the cell is constructed from an inner 71/60 ground quartz joint, Figure A.9, and is filled with approximately 120 ml solution for most experiments. Total volume of the cell is 400 cm^3. The test compartment is of sufficient size that a large platinum or gold electrode may be held by one of the five sample holders to serve as a counterelectrode during capacitance or photolysis studies. One hundred ml is a small enough volume of solution that pre-electrolysis can be performed in 36 hours using the large Pt foil as an anode and the gold c.e. as the cathode, if pre-electrolysis is desired. The solution

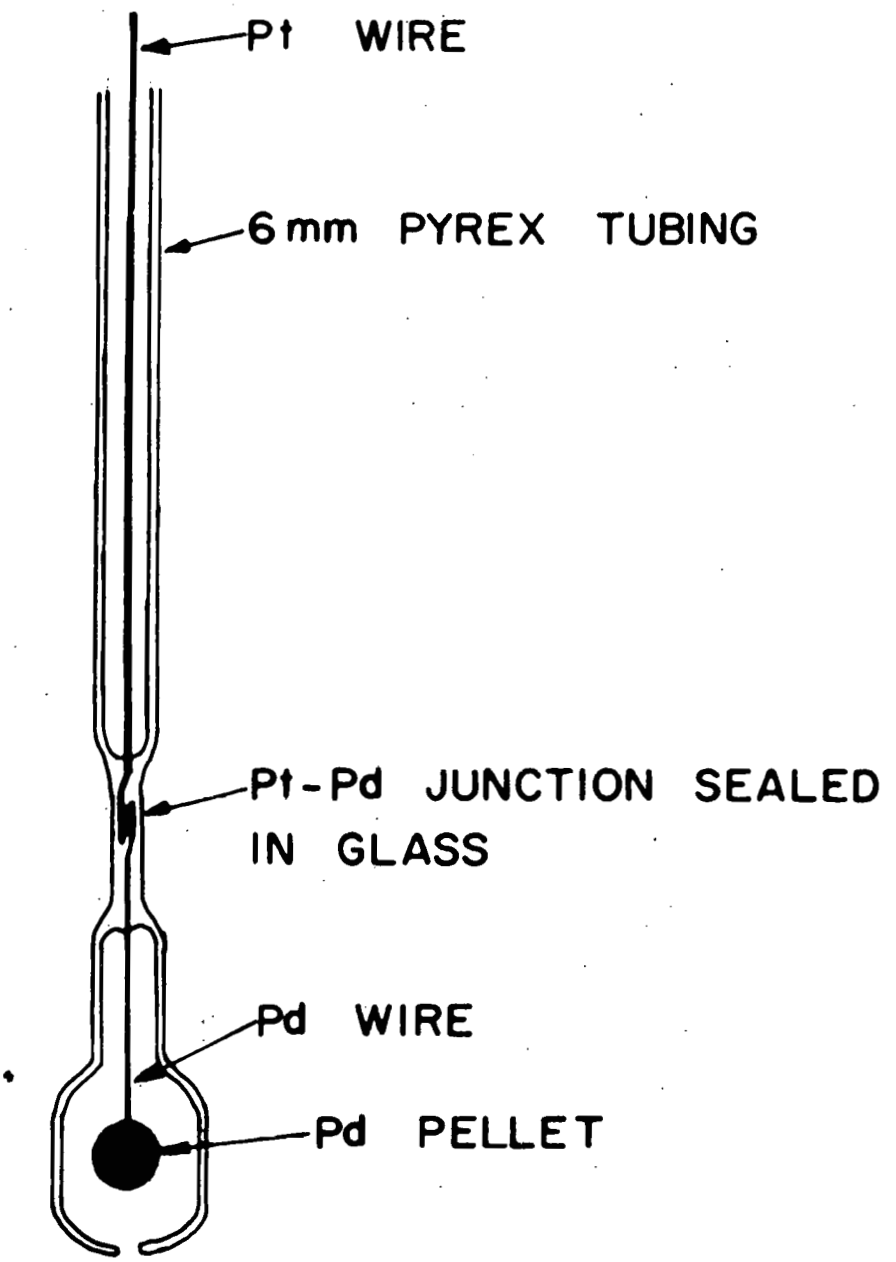

Figure A.6. Palladium-Hydride reference electrode of the design by McHardy (53)

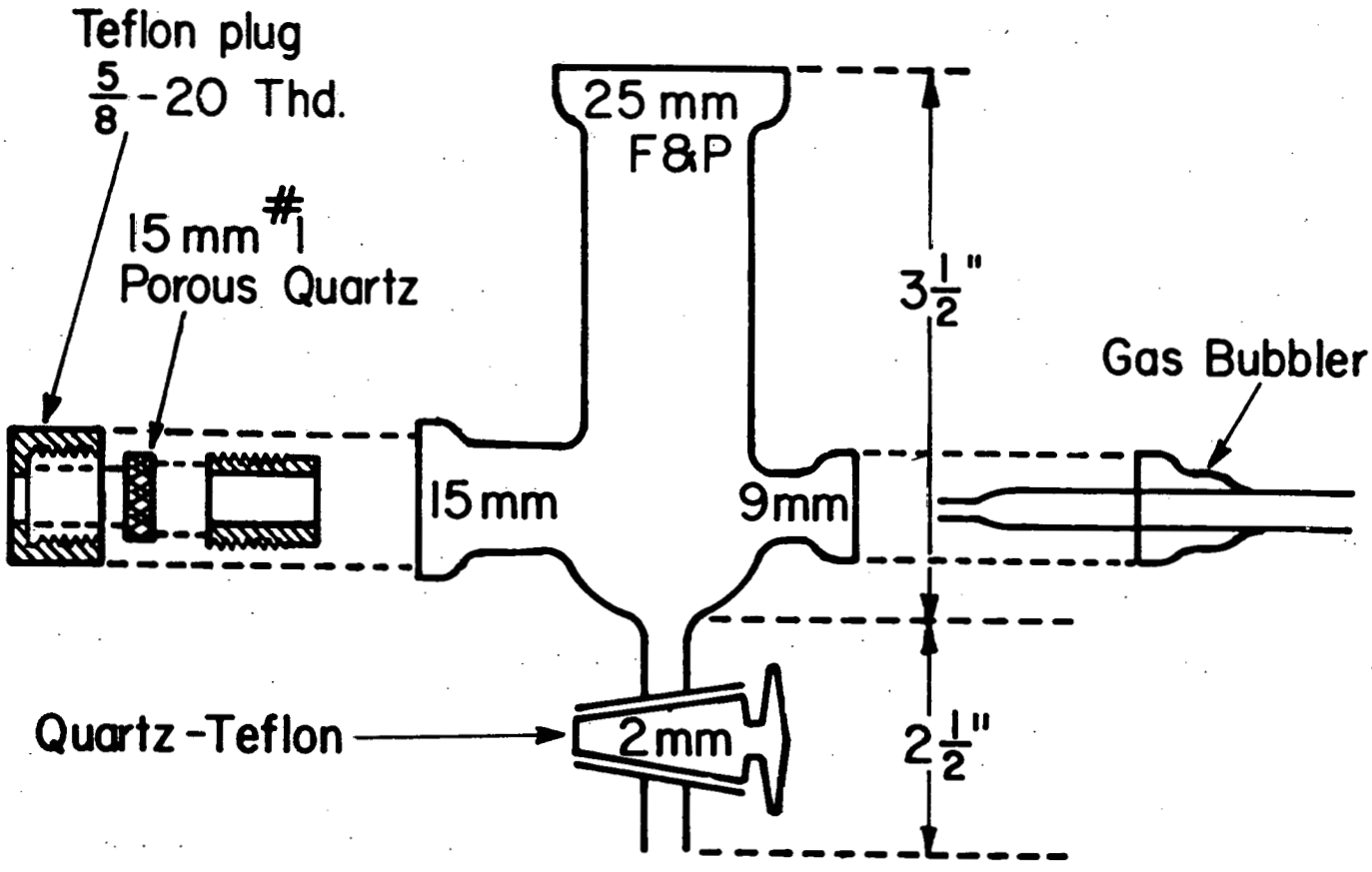

Figure A.7. Outer counter electrode compartment

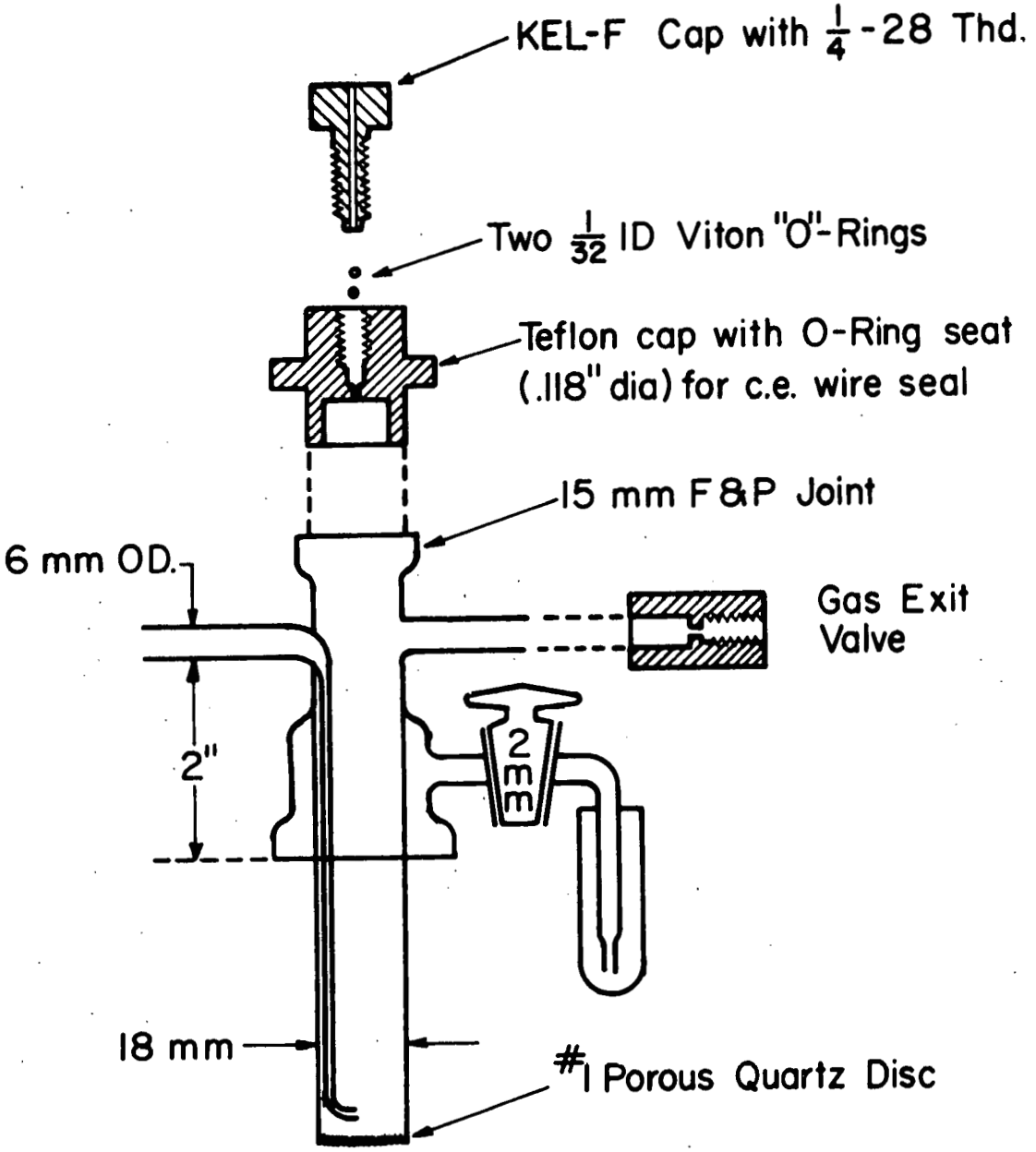

Figure A.8. Inner counter electrode compartment. A gold foil can be inserted from the top and suspended by a gold wire (not shown). The wire seal is made by two viton O-rings and then hydrogen is bubbled from the bottom up onto the gold foil

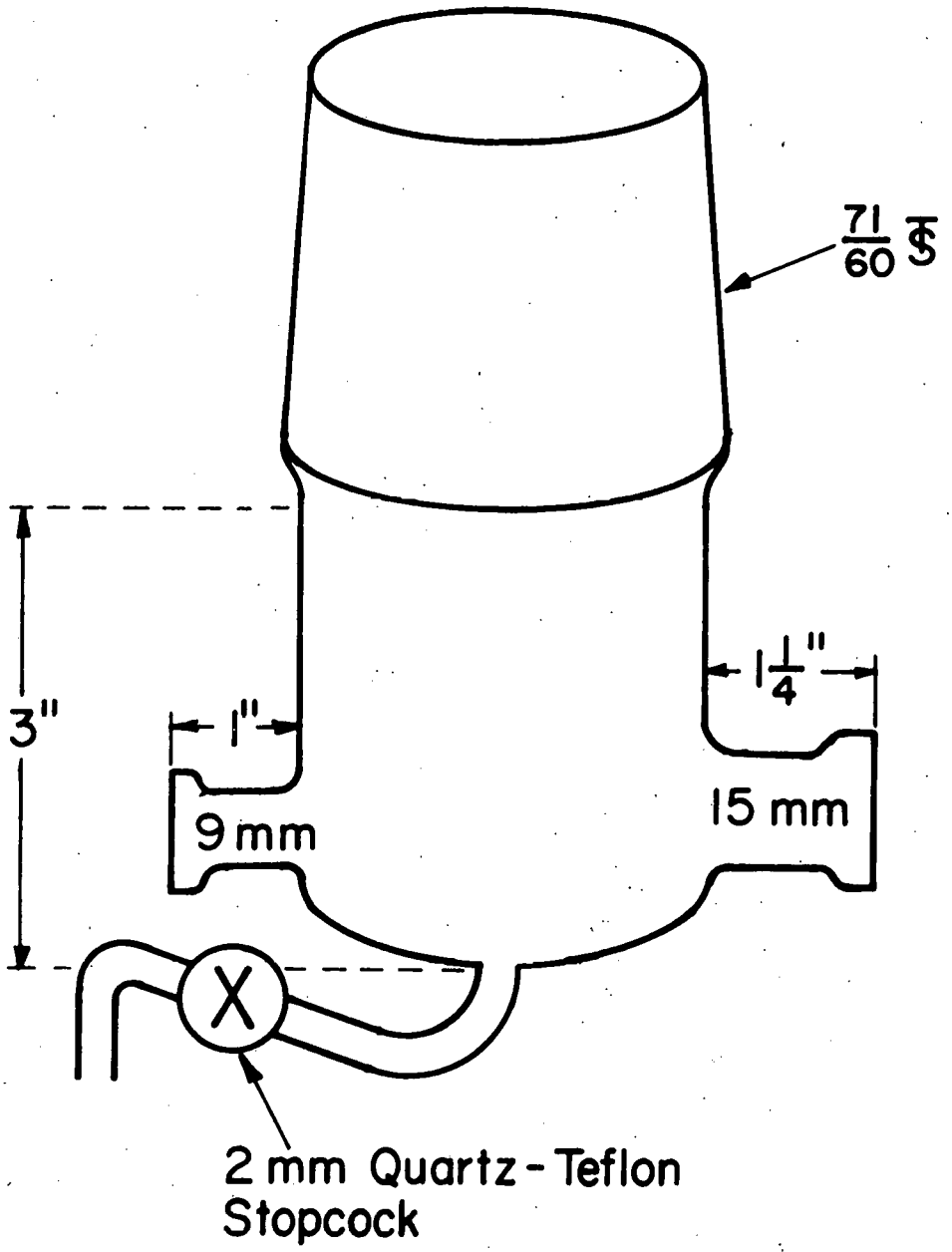

Figure A.9. Test compartment of the cell, made from a 71/60 quartz joint

in the test compartment may be vigorously stirred with a 1½" magnetic stirring bar. Two-millimeter teflon-quartz stopcocks provide drainage for the test and c.e. compartments.

Any of three different gases (O_2, H_2, He) may be independently bubbled into the test compartment and the inner c.e. compartment. The gas bubbled into the outer c.e. compartment is always the same as the gas passed through the test compartment. Extensive efforts were made to purify the gases bubbled into the cell. "Zero oxygen" with <0.2 ppm total hydrocarbons (THC) was passed through a quartz tube of platinized asbestos at 450°C, then over moist KOH (to remove CO_2) and then through two traps containing Linde 13X molecular sieve. When an inert atmosphere was needed, 99.998 percent pure "zero helium" (<0.5 ppm THC) was passed over hot copper turnings and through two liquid N_2 cooled cold traps also containing Linde 13X molecular sieve. The gas handling system was constructed entirely of acid cleaned stainless steel and pyrex tubing, with Fischer and Porter glass-teflon valves and S. S. Swagelock tubing connectors.

All parts of the still and cell were cleaned by soaking at least 24 hours in a 50-50 mixture of sulfuric and nitric acids before the final assembly. Each part was then rinsed at least six times with conductivity water from a Barnstead tin block still. All gas lines for the system were also cleaned with acid, the stainless steel by etching with nitric acid, and the borosilicate glass tubing by the method just described. Stainless steel tubing was used as the connections to the gas cylinders. The remaining tubing is of borosilicate glass. No glass

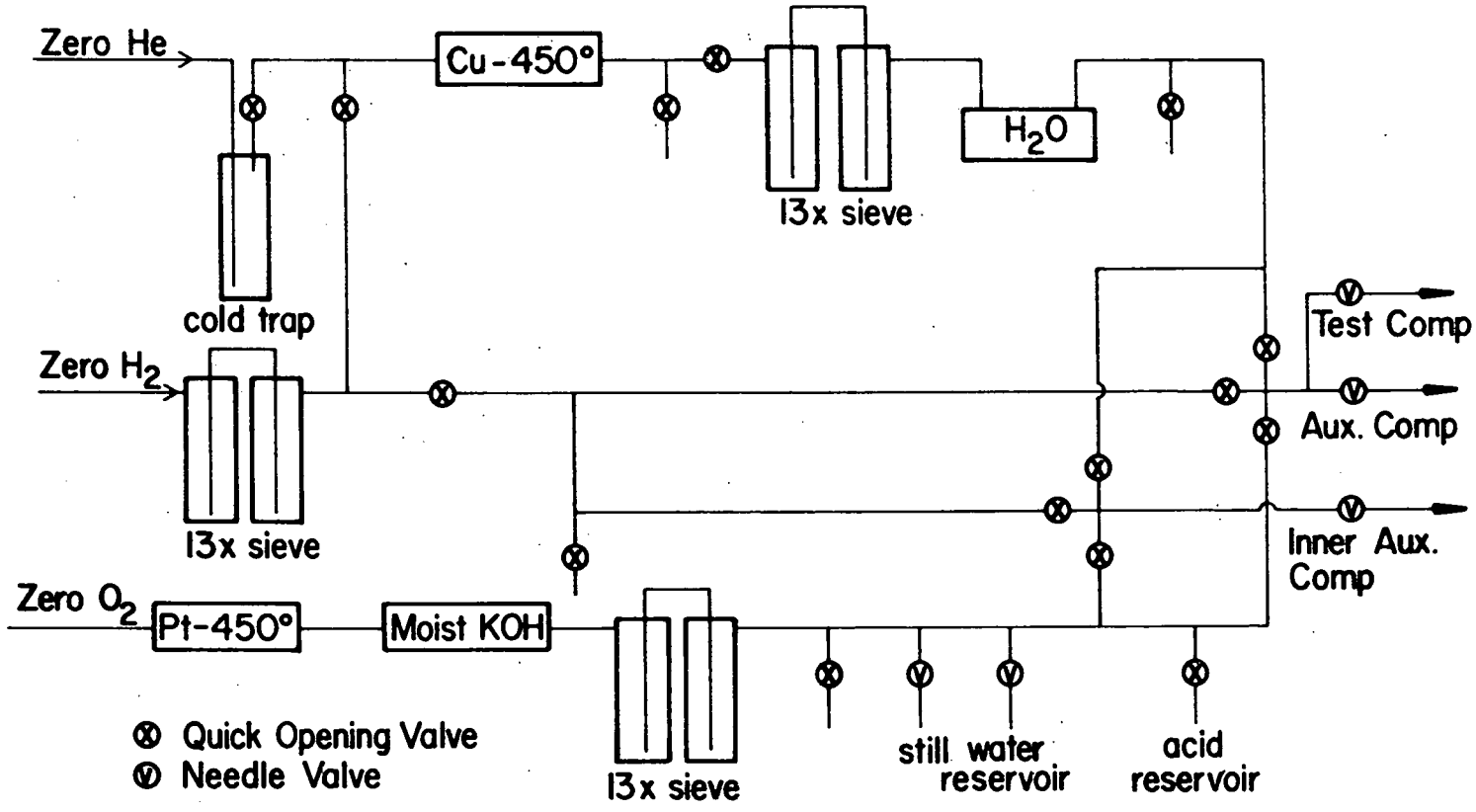

Figure A.10. Gas purification and valving system for the helium, hydrogen, and oxygen gases used in the experiments

blowing was performed after cleaning the parts. All glass tubes were connected with swagelock brand s.s. tubing connectors with teflon ferrules. All parts of the still are connected by Fischer and Porter teflon-quartz "solv-seal" joints.

The equipment described here was constructed in two air exhaust hoods for safety during the use of hydrogen gas. Photographs of the gas purification trains and the still and cell are shown in Figures A.11 and A.12.

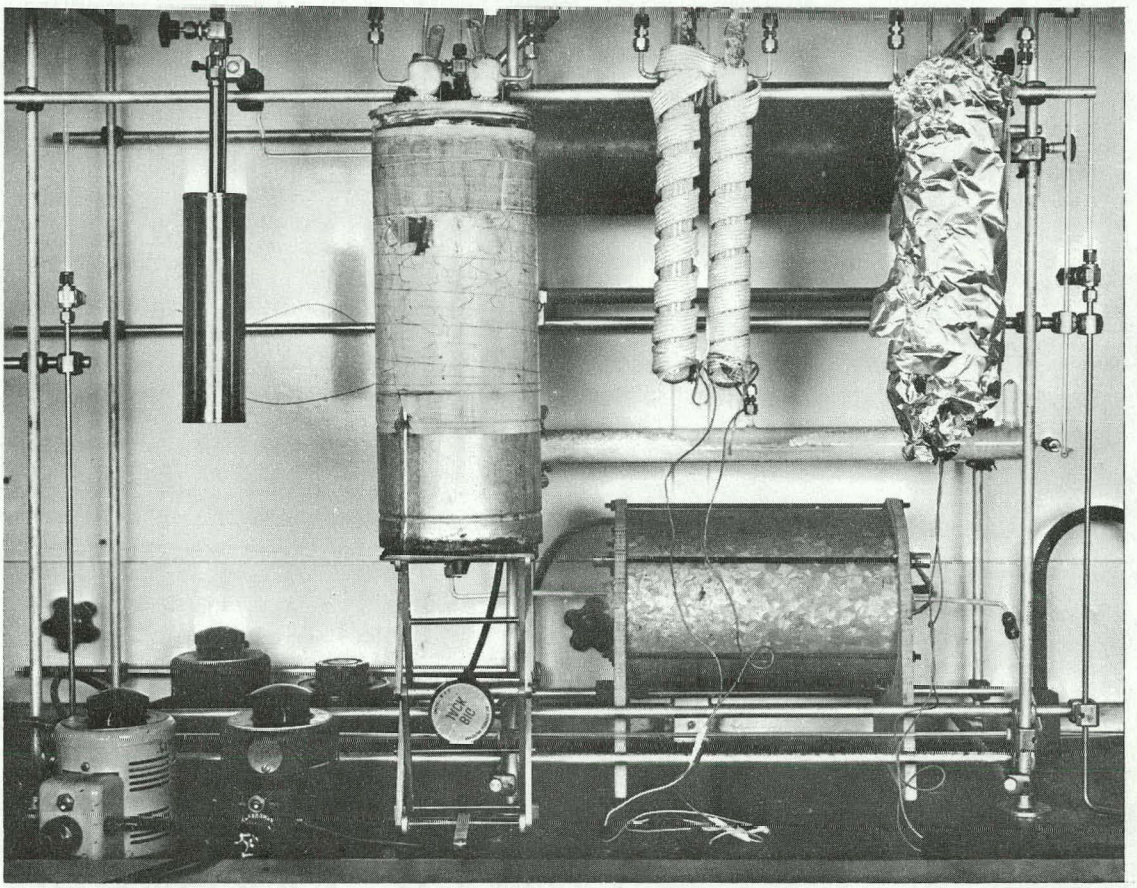

Figure A.11. Photograph of the gas purification trains for the helium, hydrogen and oxygen gases used in the experiments

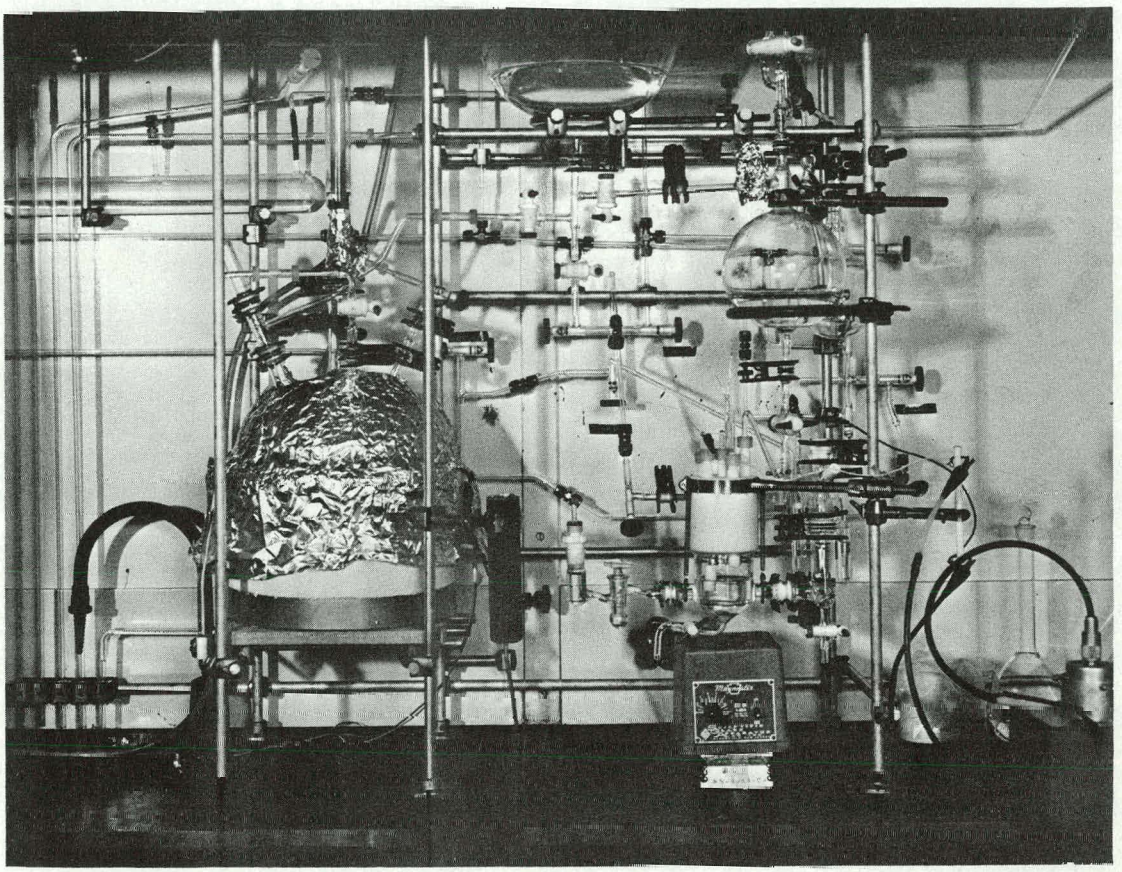

Figure A.12. Photograph of the high purity quartz still and electrochemical cell. The boiling flask for the still is at left center, storage flask at center top, solution mixing flask on the upper right, with the cell below it

APPENDIX B. WIDE RANGE-CONSTANT CURRENT POWER SUPPLY

Introduction

The first electrochemical experiments conducted consisted of the measurements of d.c. currents and voltages for various full cell and half cell reactions. Today, a wide range of instruments is used, involving many a.c. and pulsed techniques. However, d.c. measurements still are used to obtain several important electrochemical parameters such as exchange currents and transfer coefficients of various electrochemical reactions.

Of particular interest today, due to demands for better fuel cells, is the oxygen electrode and its d.c. current-voltage characteristics. If the galvanostatic method of measurement is employed, the constant current power supply used must contain several important features. Firstly, room temperature studies of oxygen reduction at an electrode-solution interface require a very wide range of current densities. The Tafel plot for oxygen reduction on platinum extends from 10^{-8} A/cm^2 to 10^{-3} A/cm^2.

Besides producing very low current densities, the d.c. current source should be very stable both as a function of time and of large variations in the load. The first feature is required because the time required for a steady-state potential to occur can be as long as several hours. Any noticeable change in current will perturb the interface, thus prolonging even further the attainment of a steady-state condition. The second feature is required because chemical changes on the electrode surface in time greatly change the voltage drop across the interface.

Technical Details

The circuit schematic diagram is shown in Figure B.1. This circuit produces a constant current through a load by maintaining a constant voltage across any of the current range resistors R_1 through R_8. The load is connected to the shielded "high output" and "low output" terminals and is in series with the current range resistor selected. The shields are connected to chassis ground.

The voltage applied to a range resistor is sensed by a high-input-resistance voltage follower. The output of the voltage follower is connected to the inverting input of a μA741 op-amp. The non-inverting input of the same op-amp is connected to the wiper of the ten turn pot R10. R10 produces the voltage level we wish to apply to a current range resistor. The voltage levels at the two inputs are then compared by the op-amp and the difference is amplified with a gain of 100. This amplified signal is again amplified by a second μA741 op-amp with a gain of 100 for a total gain of 10,000. Since the feedback signal is connected to an inverting pin of the op-amp, the amplified signal acts to decrease the difference signal to a negligible value. The difference in voltage levels at the "+" and "-" inputs of the μA741 op-amp on the right must be kept small because this difference is the error between the intended voltage from R10 and the actual voltage at the "low output" terminal. The difference signal is directly proportional to the load requirements and so cannot be compensated by any zero offset or other calibration techniques. A high gain is, therefore, essential in obtaining an accurate output current.

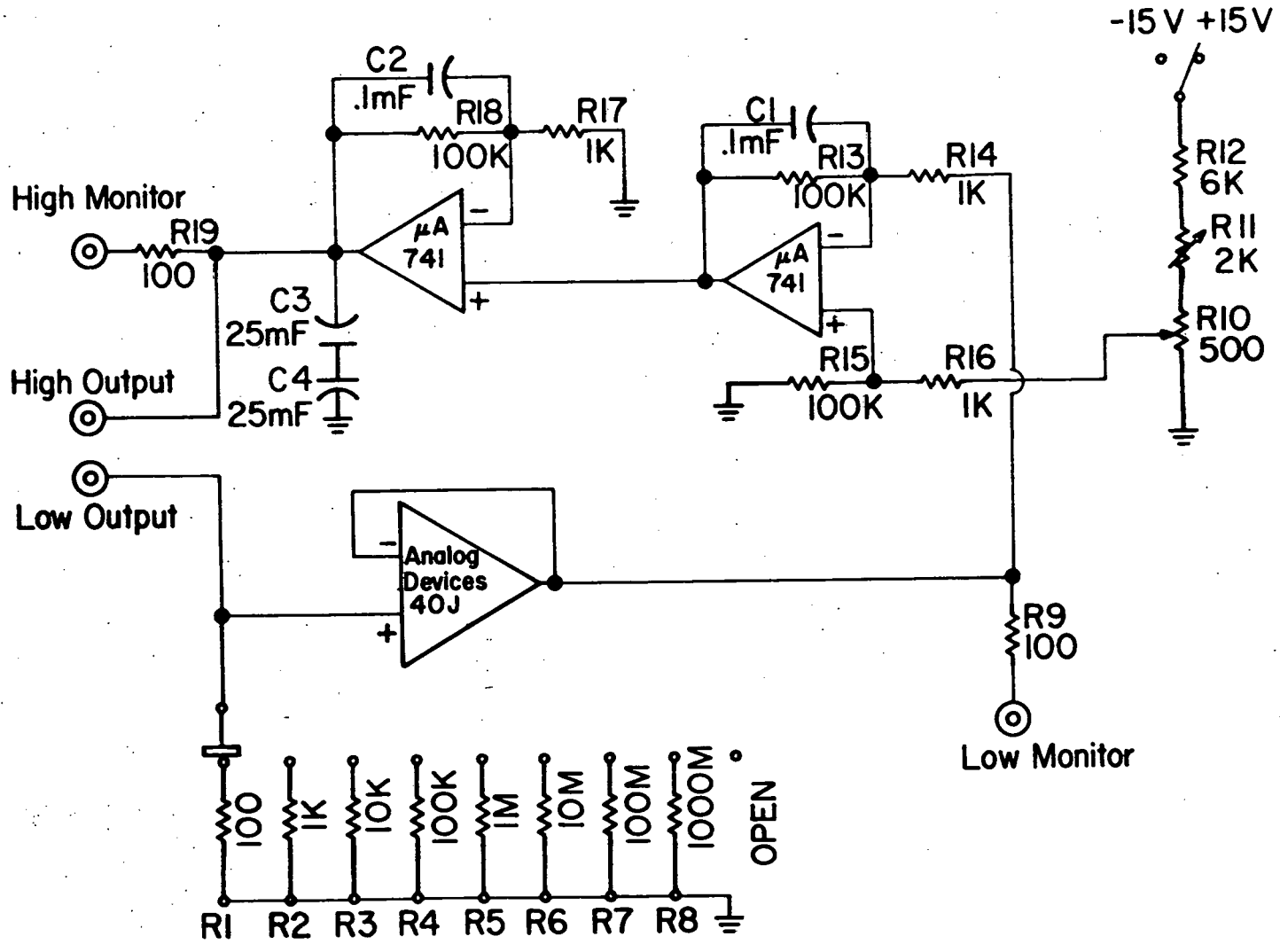

Figure B.1. Circuit schematic diagram for the wide range constant current power supply

The device is calibrated when the voltage output at the "low monitor" equals the value on the dial of the ten turn pot R10. Nominal values of R11 and R12 are chosen to produce approximately one volt across R10 and the calibration procedure consists only of fine adjustments on R11. The circuit then produces any voltage between 0 and ±1 volt (±0.5%) across any of the current range resistors. Each range, therefore, produces between 0 and $\frac{1V}{R_x}$ amps, x = 1, 2, ... 8. For accuracy, only voltages between 0.1 V and 1.0 V are used. The accuracy of the device is determined mainly by the accuracy of the current range resistors. The range resistors R_1 through R_6 are wire wound and metal film 1% resistors, but each resistor was checked and found to be within 0.5% of the stated value. The 100 MΩ and 1000 MΩ resistors are electrometer input resistors with a stated accuracy of ±1%. The actual current flowing through the range resistors was checked with a 100 Ω standard resistor on the high current ranges and with an electrometer on the low current ranges. The accuracy on all ranges is about ±1%.

The range selector switch must have a very high resistance between poles, such as the Leeds and Northrup 12 point selector switch with acrylonitrile styrene shaft and body. Likewise, the voltage follower in the feedback loop must have a very high input resistance so as not to perturb the small currents on the lowest ranges. A FET input Op amp with a specified minimum resistance of 10^{11} ohms was used in the circuit shown here.

A high gain amplifier, as this instrument, with direct feedback will invariably oscillate under some or even all load conditions. To

prevent oscillations, 0.1 μf ceramic capacitors C_1 and C_2 are placed across the 100 KΩ feedback resistors R13 and R18. This arrangement is essentially a low band pass filter. Still, transients which occurred with device turn-on caused the 40 J Op amp to latch permanently at 15 V. The back-to-back 50 μF electrolytic capacitors C_3 and C_4 completely eliminated this problem. Electrolytic capacitors were used because of their small size so they could be placed on a plug-in circuit card with the rest of the circuit.

The addition of the feedback and stabilizing capacitors destroys the frequency response of the device for medium and high frequencies, but this loss is unimportant for a constant current power supply. Low frequency load drift and 60 Hz power line interference are easily counteracted by this circuit and do not change the load current.

The physical layout of the circuit is shown in Figure B.2. The circuit is constructed on a standard plug-in circuit card with copper contacts. A schematic of the power supply and chasis wiring is shown in Figure B.3.

Performance

The device described above has been tested on all current ranges and is now used continuously in the type of measurements described in the introduction. This instrument has worked very well on all current ranges from 10^{-10} A to 10^{-2} A, with no problems whatsoever.

This power supply eliminates the need for the separate measurement of the current, a process which usually requires an electrometer for the

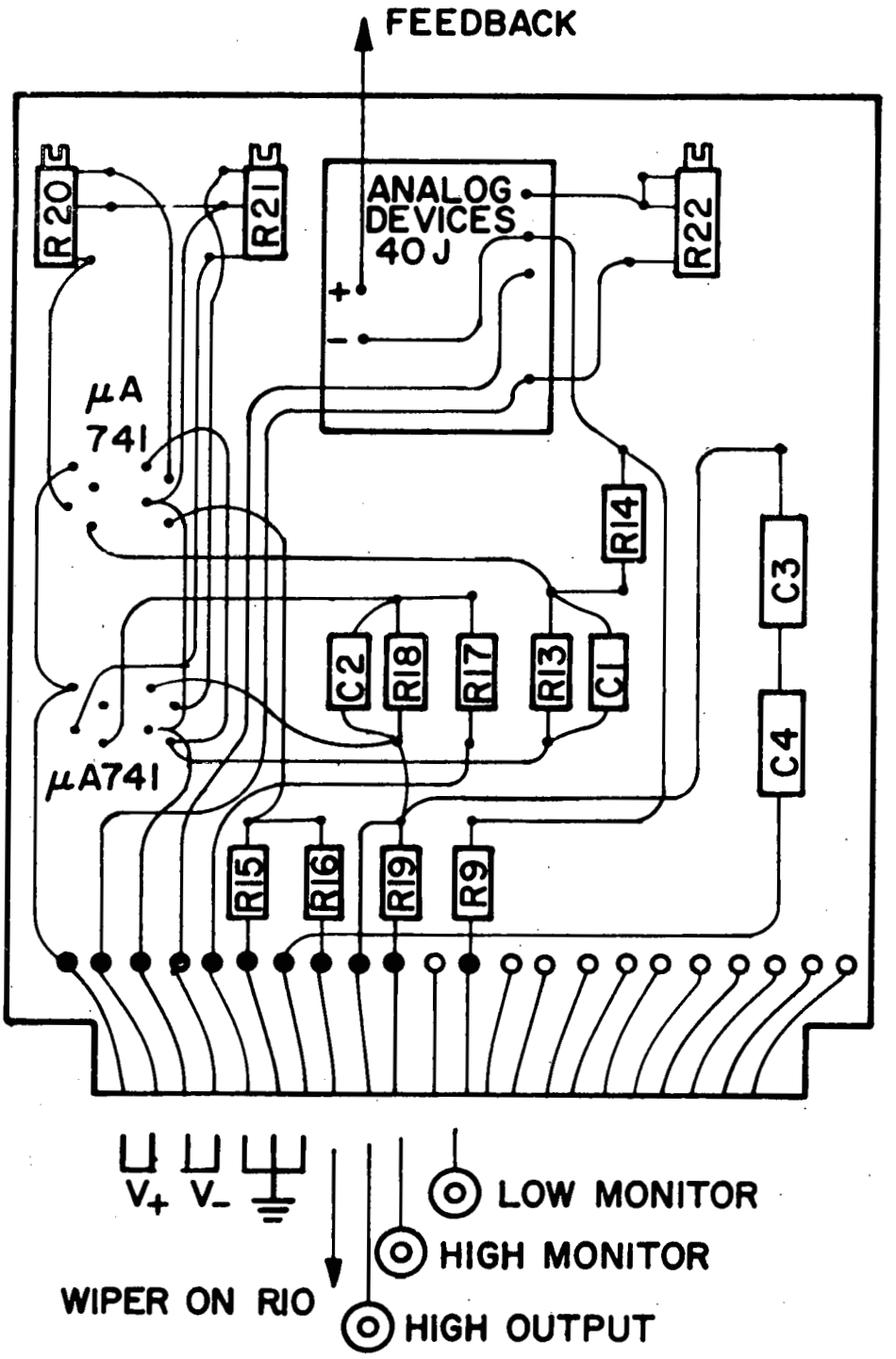

Figure B.2. Component layout on a plug-in card for the circuit shown in Figure B.1

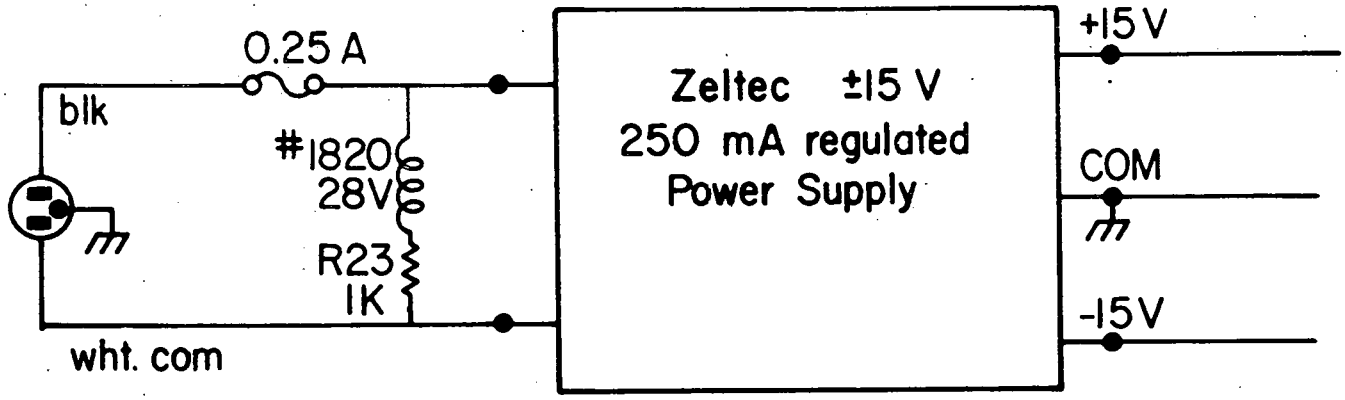

Figure B.3. Chassis wiring diagram for the constant current power supply

smaller currents. Even though neither side of the sample is held at ground, a differential input electrometer is not needed because the voltage on the low side of the sample is already well-known. The voltage level at the "low monitor" terminal never deviates more than 0.5% from the stated value on the R10 potentiometer dial. The noise level at the "low monitor" terminal is $\leq$0.2 mV peak to peak as determined with an oscilloscope with a 1 mV/cm input range. The voltage drift at the same terminal is less than 1 mV from week to week or between periods of non-use. The calibration and monitoring of the instrument was performed with a Dymec model 2401A integrating digital voltmeter and a Keithley model 640 electrometer.

REFERENCES

1. T. Wolfram, F. J. Morin, and R. Hurst, Proc. Workshop on Electrocatalysis on Non-Metallic Surfaces, Natl. Bur. Std. Spec. Publ. 455, edited by Alan D. Franklin (U.S. GPO, Washington, D.C., 1976), p. 21.

2. Ernest Yeager, Proc. Workshop on Electrocatalysis on Non-Metallic Surfaces, Natl. Bur. Std. Spec. Publ. 455, edited by Alan D. Franklin (U.S. GPO, Washington, D.C., 1976), p. 203.

3. A. C. C. Tseung and H. L. Bevan, Electroanal. Chem. Interfacial Electrochem. 45, 429 (1973).

4. James P. Hoare, The Electrochemistry of Oxygen (Interscience, New York, 1968), p. 122.

5. D. B. Sepa, A. Damjanovic, and J. O'M. Bockris, Electrochim. Acta 12, 746 (1967).

6. S. Sawada and G. C. Danielson, Phys. Rev. 113, 803 (1959).

7. A. Magneli, Nature, 169, 791 (1952).

8. Howard R. Shanks, J. Cryst. Growth 13/14, 433 (1972).

9. L. D. Muhlstein and G. C. Danielson, Phys. Rev. 158, 825 (1967).

10. M. Campagna, G. K. Wertheim, H. R. Shanks, and F. Zumsteg, Phys. Rev. Lett. 34, 738 (1975).

11. L. Kopp, B. N. Harmon, and S. H. Liu, Solid State Commun. 22, 677 (1977).

12. J. O'M. Bockris and J. McHardy, J. Electrochem. Soc. 120, 53 (1973).

13. J. P. Randin, A. K. Vijh, and A. B. Chugtai, J. Electrochem. Soc. 120, 1174 (1973).

14. M. F. Weber and H. R. Shanks, Proc. Workshop on Electrocatalysis on Non-Metallic Surfaces, Natl. Bur. Std. Spec. Publ. 455, edited by Alan D. Franklin (U.S. GPO, Washington, D.C., 1976), p. 297.

15. P. G. Dickens and R. J. Hurditch, Nature 215, 1266 (1967).

16. B. Broyde, J. Catalysis 10, 13 (1968).

17. J. H. Fishman, J. F. Henry, and S. Tessore, Electrochim. Acta 14, 1314 (1969).

18. J. O'M. Bockris and J. McHardy, J. Electrochem. Soc. 120, 61 (1973).

19. J. P. Randin, J. Electrochem. Soc. 121, 1029 (1974).

20. A. J. Appleby and C. Van Drunen, J. Electrochem. Soc. 123, 200 (1976).

21. R. D. Armstrong, A. F. Douglas, and D. E. Williams, Energy Conversion 11, 7 (1971).

22. M. Voinov and H. Tannenberger, From Electrocatalysis to Fuel Cells, G. Stanstede, editor (Univ. of Washington Press, Seattle, Washington, 1972), p. 101.

23. J. Vondrak and J. Balej, Collection Czechoslav. Chem. Commun. 40, 3298 (1975).

24. J. Heffler and H. Böhm, Mettalloberflaeche Angew. Electrochem. 27, 77 (1973).

25. J. McHardy and P. Stonehart, Electrochemistry (Physical Chemistry, series two, Vol. VI), (International Review of Science), A. D. Buckingham, consultant editor, J. O'M. Bockris, volume editor (Butterworths, London, 1976), p. 171.

26. W. Vielstich, Fuel Cells (Wiley-Interscience, New York, 1970).

27. J. O'M. Bockris and A. K. N. Reddy, Modern Electrochemistry, Vol. 2, (Plenum/Rosetta, 1973).

28. Tibor Erdey-Grúz, Kinetics of Electrode Processes (Wiley-Interscience, New York, 1972).

29. R. W. Gurney, Proc. Roy. Soc. A 134, 137 (1931).

30. J. Horiuti and M. Polanyi, Acta Physicochimica U.R.S.S. 4, 505 (1935).

31. R. A. Marcus, J. Chem. Phys. 43, 679 (1965).

32. V. G. Levich, Advances in Electrochemistry and Electrochemical Engineering, Vol. 4, edited by Paul Delahay (Interscience, New York, 1961), p. 249.

33. H. Gerischer, Zeitschrift für Physikalische Chemie Neue Folge. 26, 325 (1960).

34. D. B. Matthews and J. O'M. Bockris, Modern Aspects of Electrochemistry, edited by J. O'M. Bockris and B. E. Conway (Plenum, New York, 1971), p. 242.

35. A. Damjanovic, A. Dey, and J. O'M. Bockris, Electrochim. Acta 11, 791 (1966).

36. A. Damjanovic, A. Dey, and J. O'M. Bockris, J. Electrochem. Soc. 113, 739 (1966).

37. M. O. Davies, M. Clark, E. Yeager, F. Hovorka, J. Electrochem. Soc. 106, 56 (1959).

38. H. Gerischer, Proc. Workshop on Electrocatalysis on Non-Metallic Surfaces, Natl. Bur. Std. Spec. Publ. 455, edited by Alan D. Franklin (U.S. GPO, Washington, D.C., 1976), p. 1

39. Eric R. Brown and Robert F. Large, Chapter VI in Cyclic Voltammetry, AC Polarography and Related Techniques, A. Weissberger and B. W. Rossiter, editors (Wiley-Interscience, New York, 1971).

40. Ralph N. Adams, Electrochemistry at Solid Electrodes, Allen J. Bard, consulting editor (Marcel Dekker, New York, 1969).

41. R. S. Nicholson and I. Shain, Anal. Chem. 36, 706 (1964).

42. F. Will and C. A. Knorr, Zeit. Elektrochem. 64, 258 (1960).

43. S. Srinivasan and E. Gileadi, Electrochim. Acta 11, 321 (1966).

44. B. E. Conway and H. Angerstein-Kozlowska, Proc. Workshop on Electrocatalysis on Non-Metallic Surfaces, Natl. Bur. Std. Spec. Publ. 455, edited by Alan D. Franklin (U.S. GPO, Washington, D.C., 1976), p. 107.

45. Z. Nagy and J. McHardy, J. Electrochem. Soc. 117, 1222 (1970).

46. B. E. Conway, H. Angerstein-Kozlowska, and W. B. A. Sharp, Anal. Chem. 45, 1331 (1973).

47. J. O'M. Bockris, A. K. M. S. Hug, Proc. Roy. Soc. A 237, 277 (1956).

48. N. Watanabe, M. A. V. Devanathan, J. Electrochem. Soc. 111, 615 (1964).

49. R. Thacker and J. P. Hoare, J. Electrochem. Soc. 113, 862 (1966).

50. A. Iverson, J. Phys. Chem. 68, 515 (1964).

51. R. W. Powers, Electrochemical Technology 2, 163 (1964).

52. B. D. Cahan, Ph.D. thesis, University of Pennsylvania (1968), p. 37.

53. J. McHardy, Ph.D. thesis, University of Pennsylvania (1972), p. 84.

54. B. S. Hobbs and A. C. C. Tseung, J. Electrochem. Soc. 120, 766 (1973).

55. Calculated by B. N. Harmon and S. H. Liu, using the method described in Reference 11 (unpublished results).

56. Jean-Paul Randin, J. Electrochem. Soc. 120, 378 (1973).

57. J. Vondrak and J. Balej, Electrochim. Acta 20 283 (1975).

58. D. B. Sepa, D. S. Ovcin, and M. V. Vojnovic, J. Electrochem. Soc. 119, 1285 (1972).

59. R. J. Mannan, Ph.D. thesis, University of Pennsylvania (1967).

60. J. Vondrak and J. Balej, Electrochim. Acta 18, 1017 (1973).

61. J. P. Remeika, T. H. Geballe, B. T. Matthias, A. S. Cooper, G. W. Hull, and E. M. Kelly, Phys. Lett. 24A, 565 (1967).

62. G. Siclet, J. Chevrier, J. Lenoir, and C. Eyraud, Compt. Rend. (Paris) C 277, 227 (1973).

ACKNOWLEDGMENTS

Many people deserve credit for first making this project possible and then enabling this first phase to be completed. I extend my thanks to Howard Shanks and Al Bevolo for conceiving and writing the initial NSF proposal, the National Science Foundation for funding it, Professor Gordon Danielson for his enthusiastic support of my work, and especially to Dr. Erwin Buck, without whom the project may never have gotten off the ground. A second round of thanks to Howard Shanks and Duke Sevde for growing the best tungsten bronze crystals in the world for me to use, Al Bevolo for his expertise in the surface analysis of the crystals, and to Professor Danielson for teaching me the fundamentals of clear, concise writing.

The highly professional and beautiful work of Harold Hall of the glass shop in making the quartz still and cell was much appreciated, as was the careful and painstaking manner in which Dr. Harry Horner of the Botany Department obtained the SEM photographs of some of the crystals.

Dave Eckels always would help discuss possible solutions for many problems and questions that arose in the course of this work, and his interest was greatly appreciated.

Just as important as all of the above, was my friendship and association with many fellow students who made my stay here at Iowa State University a very enjoyable one.